2017

New Hypervelocity Terminal Intercept Guidance Systems for Deflecting/Disrupting Hazardous Asteroids

Joshua Lyzhoft
Iowa State University

New hypervelocity terminal intercept guidance systems for deflecting/disrupting hazardous asteroids

by

Joshua Richard Lyzhoft

A dissertation submitted to the graduate faculty

in partial fulfillment of the requirements for the degree of

DOCTOR OF PHILOSOPHY

Major: Aerospace Engineering

Program of Study Committee:
Bong Wie, Major Professor
John Basart
Ran Dai
Peter Sherman
Benjamin Ahn

The student author and the program of study committee are solely responsible for the content of this dissertation. The Graduate College will ensure this dissertation is globally accessible and will not permit alterations after a degree is conferred.

Iowa State University

Ames, Iowa

2017

DEDICATION

I would like to dedicate this thesis to Manuela. She has helped during difficult times and has shown me multiple paths of possibilities for solutions as well as happiness.

TABLE OF CONTENTS

LIST OF TABLES

LIST OF FIGURES

ACKNOWLEDGEMENTS

I would like to thank my parents (Rick and Michelle), siblings (Jeremiah and Karissa), family, and friends for the time and effort they have given to support me in my scholarly endeavor. In addition, I would like to give a special thank to my major professor, Dr. Bong Wie, for giving me his guidance and expertise to navigate and find the solutions to many challenging problems. My colleagues have been there to support me, give me ideas, and put up with my insanity. For that, they too will forever have my thanks. Finally, I would like to thank my committee members, Dr. John Basart, Dr. Ran Dai, Dr. Peter Sherman, and Dr. Benjamin Ahn, for being willing to challenge me to bring knowledge and advancements to my research area.

ABSTRACT

Computational modeling and simulations of visual and infrared (IR) sensors are investigated for a new hypervelocity terminal guidance system of intercepting small asteroids (50 to 150 meters in diameter). Computational software tools for signal-to-noise ratio estimation of visual and IR sensors, estimation of minimum and maximum ranges of target detection, and GPU (Graphics Processing Units)-accelerated simulations of the IR-based terminal intercept guidance systems are developed. Scaled polyhedron models of known objects, such as the Rosetta mission's Comet 67P/C-G, NASA's OSIRIS-REx Bennu, and asteroid 433 Eros, are utilized in developing a GPU-based simulation tool for the IR-based terminal intercept guidance systems. A parallelized-ray tracing algorithm for simulating realistic surface-to-surface shadowing of irregular-shaped asteroids or comets is developed. Polyhedron solid-angle approximation is also considered. Using these computational models, digital image processing is investigated to determine single or multiple impact locations to assess the technical feasibility of new planetary defense mission concepts of utilizing a Hypervelocity Asteroid Intercept Vehicle (HAIV) or a Multiple Kinetic-energy Interceptor Vehicle (MKIV). Study results indicate that the IR-based guidance system outperforms the visual-based system in asteroid detection and tracking. When using an IR sensor, predicting impact locations from filtered images resulted in less jittery spacecraft control accelerations than conducting missions with a visual sensor. Infrared sensors have also the possibility to detect asteroids at greater distances, and if properly used, can aid in terminal phase guidance for proper impact location determination for the MKIV system. Emerging new topics of the Minimum Orbit Intersection Distance (MOID) estimation and the Full-Two-Body Problem (F2BP)

formulation are also investigated to assess a potential near-Earth object collision risk and the proximity gravity effects of an irregular-shaped binary-asteroid target on a standoff nuclear explosion mission.

CHAPTER 1. INTRODUCTION

1.1 Research Motivation

Earth is subject to encounters with extraterrestrial objects on a yearly basis, which can be seen by meteor showers or other events. However, some events may not be observed due to their small size and insignificant effects. Unknown impact events are statistically modeled as discussed in [1]. Events taken into account are, but not limited to, ones that cause noticeable damage to Earth. Notable damage can be seen at places such as Barringer crater as well as Chicxulub crater. Such impact events could be very dangerous to the Earth's population and cycles.

In the morning of February 15th, 2013 an impact event occurred near Chelyabinsk, Russia. A meteor measuring approximately 17 meters in diameter streaked across the sky which ended in an air burst causing harm to the nearby population and millions of dollars worth of damage to surrounding buildings [2, 3, 4, 5]. With such seemingly random events, scientific research teams are investigating asteroid and comet composition as well as intercept. This has been seen by the intercept of comet Tempel 1 (Deep Impact mission), Rosetta mission observations, proposed Double Asteroid Redirection Test (DART) mission, as well as the Hypervelocity Asteroid Intercept Vehicle (HAIV) concept [6, 7, 8, 9].

During the past ten years, the Asteroid Deflection Research Center (ADRC) has been working on innovative planetary mission concepts involving mission trajectory optimization, terminal guidance using optical navigation, and asteroid disruption using nuclear

or kinetic impactor options [11, 10, 12, 13]. These studies include analysis of missions to small targets, which measure less than 150 meters in diameter. Two concepts developed at the ADRC are the HAIV and Multiple Kinetic-energy Impactor Vehicle (MKIV) [14]. Both scenarios require the development of terminal guidance algorithms using simulated imagery to intercept the target asteroid. Once intercept is certain, the spacecraft delivers either a momentum transfer by impact to divert the target from its nominal trajectory, or a blast causing disruption or pulverization. For such reasons, precision terminal guidance and realistic image processing is required to ensure a real mission's success.

Research investigating hypervelocity intercept of a small asteroid (< 150 m) is in its infancy. However, military and defense applications, which include ballistic missile intercept, have been already developed. This has been seen with evolution of the Exoatmospheric Kill Vehicle (EKV), which has been developed by Raytheon and investigated by the Department of Defense [15]. The system incorporates an infrared sensing array as well as communication with satellite systems, which are used to aid in target intercept. Unfortunately, further military advancement assessment and reliability reports of this system are classified. In contrast, other systems which explore the use of hypervelocity intercept have been studied.

A concept similar to the MKIV is the Multiple Kill Vehicle (MKV). This system uses multiple sub-spacecraft to either independently determine a target or be given target coordinates from a main camera system. Methods of target acquisition along with devices and targeting algorithms used have not been specified. Work herein investigates the possibility of implementing a changed MKV concept which includes image segmentation algorithms as well as sub-image centroids. However, each spacecraft must still undergo precision autonomous terminal guidance maneuvers, which include these images. Investigation of image device implementation must be pursued to better understand possible realistic situations.

A key implementation of the EKV, and possibly the MKV, is the use of the infrared sensor, which has not been used for asteroid intercept in the past. These sensors, however, require a cryogenic cooling assembly due to the detector's specific detectivity at certain temperatures. When using such a device, the peak emissions of asteroids fall within the sensitive regime of the mid to far infrared detector. This is due to the asteroid's temperature. Systems which have used an infrared detector array have been NASA's Wide-field Infrared Survey Explorer (WISE) telescope as will as Stratospheric Observatory for Infrared Astronomy (SOFIA). Both the EKV and infrared survey systems give motive to further investigate infrared devices for hypervelocity asteroid intercept in support of planetary defense.

1.2 Terminal Intercept Guidance Algorithms

Previous research work of Hawkins [16, 17] has explored the use of various proportional navigation (PN) guidance logic and predictive guidance schemes. Furthermore, he investigated the intercept capability of each guidance law separately. The work herein explores the capabilities for hypervelocity asteroid intercept when a combination of guidance laws, or hybrid, are implemented. Doing so may have the outcome of reducing the required fuel usage while still maintaining the desired precision. The research work of Hawkins [16, 17], which is based on ideal image optics, were later implemented on Graphical Processing Units (GPUs) in Kaplinger [18].

The images generated were used in calculating the line-of-sight (LOS) vector to the center of brightness (COB) of the image array [16, 17]. Targeting the COB location, along with preplanned thruster pulses, has been used in NASA's Deep Impact mission. This, however, is offset from the center of mass (COM) or the center of figure (COF) of the object, which might be desired for particular mission objectives. For the case of hypervelocity intercept, it is desired to have the most efficient energy transfer be

transformed to either complete destruction or changing the asteroid's velocity. A full shape model would be required to ensure that a location close to the COM is targeted. In some cases, a proper approach phase angle will give suitable illumination of the target for precision intercept. However, an infrared device would give this measurement regardless of approach phase angle. This reason gives a clear advantage over visible-band cameras, and it gives the main reason for further study of IR detectors.

To further add realism to the simulation, Hawkins [16, 17] implemented a Schmitt trigger to the guidance algorithm thruster output acceleration to help with system jitter and realistic thruster firing output magnitudes. The estimated LOS rate used non-filtered LOS measurements, as well as using a first-order differencing method. Since PN guidance, among other guidance laws, uses this measurement, some terminal guidance trajectories become sensitive to the targeting location pixel changes. Among the pixel location issue, image noise was not included nor was higher-order approximations for the LOS rate. In this thesis, we further investigate improvements for the LOS rate estimation and explore the use of signal filtering to compensate for the target pixel location changes. These applications will be used for the MKIV mission concept. Algorithms for determining the intercept asteroid impact locations for the multiple bodies as well as primitive object determination will be explored in this thesis

1.3 Detector Models

Kaplinger [18] uses polyhedron models, ideal geometric optics, and GPUs to create realistic grey-scale images. As stated previously, these images were used to create autonomous guidance schemes for hypervelocity asteroid intercept. These images were created without the consideration of sensor signal-to-noise ratio for varying asteroid detecting sensors. Moreover, there was no detailed investigation conducted for various camera nor sensor types as well as image noise inclusion. By neglecting the sensor noise,

digital image processing was quite trivial for finding the target's projected line-of-sight offset vector. In addition, only the visible band of light was taken into account, which only involved the inclusion of a representation for the reflectivity of the target object. Furthermore, the generated images created by Kaplinger use a primitive form for determining shadows based on face outward pointing vectors and the incoming sun vector. This does not always work when craters are present, due to complex geometry, nor when part of the object passes in front of itself.

To create more realistic images, work herein advances the synthetic imaging done by Kaplinger. One such way is by including surface-to-surface shadowing for non-convex shapes. This is particularly helpful when generating visible band images for terminal guidance. Further investigation is done in the inclusion of image signal-to-noise ratio estimation for visible and infrared wavelengths, which involves incorporating the asteroid's emissivity, reflectivity, and solid angle approximations. When considering a polyhedron shape, the solid angle is approximated by using each triangular face as well as the asteroid's location with respect to the sun as well as the spacecraft. For the infrared detector, both photon and thermal sensor are explored. Confirmation for the infrared sensor formulation herein is done by calculating and comparing detection distances for the already operational WISE telescope. Moreover, specific telescope and sensor parameters are explored for the use in terminal guidance, which includes trajectory simulations based from synthetic imaging.

Another device that is considered is radar, which is primarily used for the investigation of maximum detection distance estimation. In general, components of the radar can be changed to fit the users needs. However, estimation for the cross-sectional area using polyhedron models is not explored. This becomes very complicated since the internal composition as well as structure of any asteroid interest needs to be considered. Estimation of the cross-sectional area is completed by scaling already known smaller asteroids, such as Bennu.

1.4 Orbit Characterization and Binary Asteroid Systems

Orbit characterization is important to establish if an asteroid or any other near-Earth object (NEO) would cause a risk to Earth and its inhabitants. Researchers and scientist use measurement data from observations to estimate an object's orbital elements. This also includes Earth among other celestial body's. In reality, orbital elements vary over time due to the non-Keplerian motion which is experienced. These effects are caused by the gravitational pull from all objects within the solar system. However, Keplerian motion can be a close approximation for an initial glance at potentially hazardous objects.

A method was developed which calculates the minimum orbit intersection distance (MOID) between 2 ellipses [19]. Since Keplerian motion, without perturbations, are ellipses, the MOID algorithm can be applied to an Earth ellipse and known solar system body ellipse. This method, however, is independent of time and requires progressing through discrete angles between zero and 360 degrees. Hence, the speed of the algorithm is based on the amount of precision required by discretization, which was never stated in [19]. Work herein investigates a linear interpolation accuracy when finding crossing events. Doing so allows for lower number of discretized points, which increases computational speed. Increasing speeds would allow for a more efficient search for known potentially hazardous NEOs.

Another area of interest when considering planetary defense is solar system binary objects. This is particularly interesting for hypervelocity intercept as well as proximity dynamics due to complexity of the localization of objects. Recent work on the Double Asteroid Redirection Test (DART) has been investigating the Didymos binary system [20]. The proposed mission will send a spacecraft to intercept with the secondary body. Measurements from the perturbed secondary body will help in understanding binary asteroid movement and reaction to impulsive forces. Researchers and engineers at the Jet Propulsion Laboratory (JPL) and NASA Goddard Space Flight Center (GSFC) have

been using polyhedron shape models to simulate the full-two-body-problem (F2BP). Work herein supports the work done at the GSFC. In addition to using a formulation developed in [21], further advancements have been made in the use of non-convex shapes as well as varying pockets of internal density. However, the density pockets must also be represented by an internal polyhedron as well as a density difference from the nominal constant density.

A variety of topics are investigated throughout this work, which range from initial orbit characterization to terminal guidance algorithms and realistic sensor simulations. Each subject is needed to ensure that hazardous celestial objects can be determined and then disrupted or eliminated. The initial MOID calculation helps find known objects that may be harmful to Earth. Incorporating image sensor simulations provide the terminal guidance algorithms with realistic measurements corresponding to the asteroid. Investigating binary asteroid system dynamics provides a unique and challenging scenario, if such a system were to endanger the planet.

CHAPTER 2. HYPERVELOCITY TERMINAL GUIDANCE LAWS

2.1 Introduction

The Terminal Guidance, Navigation, and Control (GNC) subsystem is one of the key subsystems of asteroid intercept and rendezvous missions. Previous missions, such as STARDUST, EPOXI, and Deep Impact have utilized terminal GNC systems to conduct celestial object flybys as well as impacts [22]. These orbital maneuvers, however, must be done autonomously based on on-board measurements of the asteroid's position and velocity states as well as target reference trajectories. If the spacecraft required human input for terminal intercept, the delay and even power required for communication with Earth could potentially cause mission failure. For this reason, autonomous guidance and control is considered for hypervelocity asteroid intercept. Two guidance logics as well as a combination of both, among using filters, are considered herein. These algorithms follow Proportional Navigation (PN), Kinematic Impulse (KI), and a hybrid of both PN and KI. However, each requires a line-of-sight vector, which can be found by using a reference trajectory and the equations of motion.

2.2 Equations of Motion

The target asteroid is modeled as a point mass in standard heliocentric Keplerian Orbit. Its orbital motion is described by

$$\dot{\mathbf{r}}_T = \mathbf{v}_T \tag{2.1}$$

$$\dot{\mathbf{v}}_T = \mathbf{g}_T \tag{2.2}$$

$$\mathbf{g}_T = -\frac{\mu_\odot \mathbf{r}_T(t)}{\|\mathbf{r}_T(t)\|_2^3} \tag{2.3}$$

where $\mathbf{r}_T$ is the position vector of asteroid with respect to the heliocentric reference frame, $\mu_\odot$ is the solar gravitational parameter, and $\mathbf{g}_T$ is the gravitational acceleration due to the sun.

Similarly, the orbital motion of a spacecraft is described by

$$\dot{\mathbf{r}}_S = \mathbf{v}_S \tag{2.4}$$

$$\dot{\mathbf{v}}_S = \mathbf{g}_S + \mathbf{u}(t) \tag{2.5}$$

$$\mathbf{g}_S = -\frac{\mu_\odot \mathbf{r}_S(t)}{\|\mathbf{r}_S(t)\|_2^3} \tag{2.6}$$

where $\mathbf{r}_S$ is the position vector of the spacecraft with respect to the heliocentric reference frame, $\mathbf{g}_S$ is the gravitational acceleration acting on the spacecraft due to the sun, and $\mathbf{u}$ is the control acceleration provided by the spacecraft thrusters. Other disturbing acceleration is neglected due to the assumption of small size asteroid [16]. However, these small disturbances may be included if higher-order dynamics are required or desired. A depiction of the simple two body system can be seen in Figure 2.1

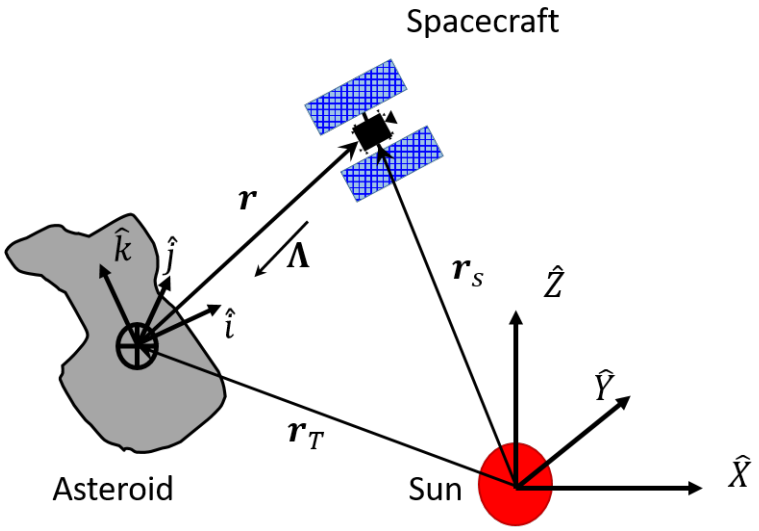

Figure 2.1: Depiction of asteroid and spacecraft position vectors along with the line-of-sight unit vector.

The relative orbital motion of the spacecraft with respect to the target asteroid is described by

$$\mathbf{r} = \mathbf{r}_S - \mathbf{r}_T \tag{2.7}$$

$$\mathbf{v} = \mathbf{v}_S - \mathbf{v}_T \tag{2.8}$$

$$\dot{\mathbf{v}} = \mathbf{g}_S - \mathbf{g}_T + \mathbf{u}(t) \tag{2.9}$$

where $\mathbf{r}$ is the relative position of the spacecraft with respect to the target asteroid. It is important to calculate the relative state, either from a reference orbit or from measured/estimated data, because this information is needed when applying a given guidance control scheme that calculates a required control acceleration.

2.3 Guidance Laws

In this section, two different terminal guidance control algorithms will be explored as well as a hybrid controller concept. It is important to note that each guidance law

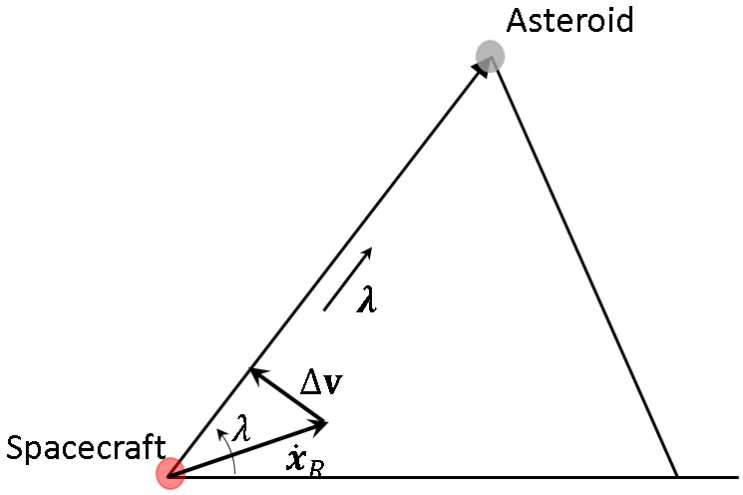

Figure 2.2: Illustration of the geometry for PN guidance.

is formulated for continuous information. In practice however, this is not the case. In a later section, we will explore the challenges when involved when considering discrete measurements, which may include optical navigation parameters.

2.3.1 Proportional Navigation (PN)

The PN guidance originates from the need of homing guidance. Homing guidance is usually referring to the mid to terminal phase of missile guidance. The PN guidance law commands acceleration perpendicular to the instantaneous spacecraft-asteroid line-of-sight (LOS) vector. At each instance, the acceleration commands are proportional to the line-of-sight rate and the relative closing velocity. If done correctly, this scheme pushes the LOS rate to zero, which, if achieved, will result in a successful intercept. An illustration of PN guidance can be seen in Figure 2.2 The guidance law, as given in [23], is

$$\mathbf{u} = nV_c\dot{\mathbf{\Lambda}} \tag{2.10}$$

where $\mathbf{u}$ is the control acceleration command, n is a unitless effective navigation gain (usually in the range of 3 to 5), V_c is the spacecraft-asteroid closing velocity, and $\dot{\mathbf{\Lambda}}$ is the LOS rate vector. The LOS rate can be calculated if the states of the target are known.

However, in cases where this is not entirely possible, an estimation of the LOS rate can be used. A simple, and if sampled fast enough, way for finding the LOS rate is by finite differencing. The first-order estimation using this method is

$$\dot{\mathbf{\Lambda}} = \frac{d\hat{\mathbf{\Lambda}}}{dt} \approx \frac{\hat{\mathbf{\Lambda}}(t) - \hat{\mathbf{\Lambda}}(t - \Delta t)}{\Delta t} \tag{2.11}$$

where Δt is the time between the current and the previous sample for the LOS vector measurements. Higher order approximations using more LOS samples are discussed later in this chapter. Other required variables are the closing velocity, time-to-go, and the line-of-sight rate which are computed as follows:

$$V_c = -\dot{\mathbf{r}} \cdot \hat{\mathbf{\Lambda}} \tag{2.12}$$

$$t_{go} = \frac{\|\mathbf{r}\|_2}{V_c} \tag{2.13}$$

$$\hat{\mathbf{\Lambda}}(t) = -\frac{\mathbf{r}(t)}{\|\mathbf{r}(t)\|_2} \tag{2.14}$$

2.3.2 Kinematic Impulse (KI) Terminal Guidance Law

The Kinematic Impulse (KI) guidance law is a predictive control method. It is based on the estimation of the LOS vector and takes into account the target's future position. The method depends on a linearized theory to minimize the cost of on-board computations. Predictive guidance requires on-board measurement to estimate the lLOS vector, as well as the LOS rate vector, and knowledge of the target asteroid's orbit. This will also be represented by the relative error state transition matrix, which is derived from orbit perturbation theory [27]. A depiction of the reference target orbit and the spacecraft can be found in Figure 2.3.

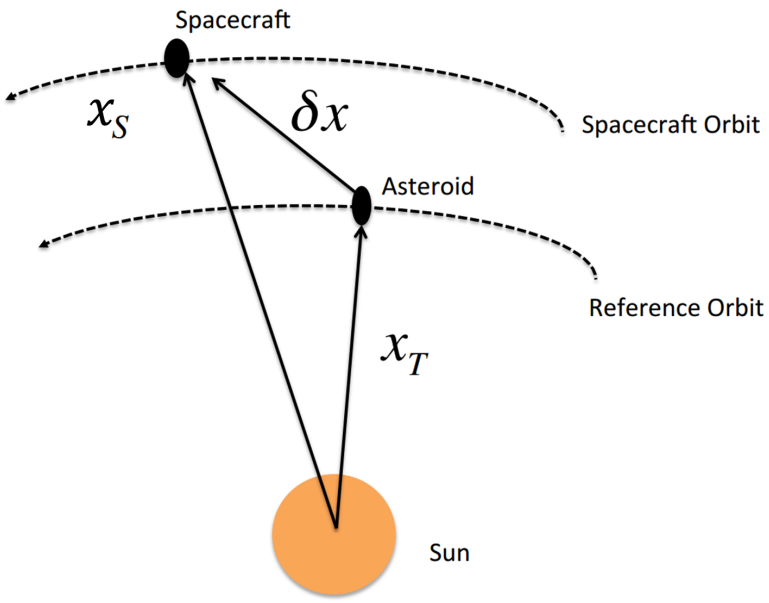

Figure 2.3: Perturbed orbital trajectories of the target asteroid and spacecraft.

A reference target represented by the asteroid's state, $\mathbf{x}_T^*$, is used to determine the spacecraft's state, $\mathbf{x}_S$, with the incorporation of the perturbation, $\delta\mathbf{x}$, as follows:

$$\mathbf{x}_S = \mathbf{x}_T^* + \delta\mathbf{x} \tag{2.15}$$

where $\mathbf{x}_S$ is the spacecraft state vector represented as

$$\mathbf{x}_S = [x_S \quad y_S \quad z_S \quad \dot{x}_S \quad \dot{y}_S \quad \dot{z}_S]^T \tag{2.16}$$

Similarily, the state for the reference trajectory is written as

$$\mathbf{x}_T^* = [x_T \quad y_T \quad z_T \quad \dot{x}_T \quad \dot{y}_T \quad \dot{z}_T]^T \tag{2.17}$$

The magnitude of the reference orbit's position vector as well as the spacecraft's position vector are described by

$$r_T = \sqrt{x_T^2 + y_T^2 + z_T^2}$$

$$r_S = \sqrt{x_S^2 + y_S^2 + z_S^2} \tag{2.18}$$

In general, the nonlinear differential equations of motion of the spacecraft are represented as

$$\dot{\mathbf{x}}_S = \mathbf{f}\left(\mathbf{x}_S, t\right) = \begin{bmatrix} \dot{x}_S \\ \dot{y}_S \\ \dot{z}_S \\ \ddot{x}_S \\ \ddot{y}_S \\ \ddot{z}_S \end{bmatrix} = \begin{bmatrix} f_1 \\ f_2 \\ f_3 \\ f_4 \\ f_5 \\ f_6 \end{bmatrix} = \begin{bmatrix} \dot{x}_S \\ \dot{y}_S \\ \dot{z}_S \\ -\frac{\mu_\odot \, x_S}{r_S^3} \\ -\frac{\mu_\odot \, y_S}{r_S^3} \\ -\frac{\mu_\odot \, z_S}{r_S^3} \end{bmatrix} \tag{2.19}$$

By substituting Equation 2.19 into 2.15 and using the perturbation theory, we obtain the equations of motion of the form

$$\dot{\mathbf{x}}_S = \mathbf{f}\left(\mathbf{x}_S, t\right) = \mathbf{f}\left(\mathbf{x}_T^* + \delta\mathbf{x}, t\right) \tag{2.20}$$

Then, by expanding the nonlinear equation using a Taylor series expansion about $\mathbf{x}_T^*$ and incorporating the time derivative of Equation 2.15 as well as applying reference trajectory state knowledge at any given time, we obtain the perturbed differential equations of motion as

$$\delta\dot{\mathbf{x}}(t) = \mathbf{F}(t)\ \delta\mathbf{x}(t) \tag{2.21}$$

where $\mathbf{F}$ is the Jacobian matrix of the $\mathbf{f}$ vector which is evaluated at $\mathbf{x}_T^*$, defined as

$$\mathbf{F}(t) = \left[\frac{\partial \mathbf{f}(t)}{\partial \mathbf{x}(\mathbf{t})}\right]_* = \begin{bmatrix} 0 & 0 & 0 & 1 & 0 & 0 \\ 0 & 0 & 0 & 0 & 1 & 0 \\ 0 & 0 & 0 & 0 & 0 & 1 \\ -\frac{\mu_\odot}{r_S^3} + \frac{3\mu_\odot x_S^2}{r_S^5} & \frac{3\mu_\odot x_S y_S}{r_S^5} & \frac{3\mu_\odot x_S z_S}{r_S^5} & 0 & 0 & 0 \\ \frac{3\mu_\odot y_S x_S}{r_S^5} & -\frac{\mu_\odot}{r_S^3} + \frac{3\mu_\odot y_S^2}{r_S^5} & \frac{3\mu_\odot y_S z_S}{r_S^5} & 0 & 0 & 0 \\ \frac{3\mu_\odot z_S x_S}{r_S^5} & \frac{3\mu_\odot z_S y_S}{r_S^5} & -\frac{\mu_\odot}{r_S^3} + \frac{3\mu_\odot z_S^2}{r_S^5} & 0 & 0 & 0 \end{bmatrix} \tag{2.22}$$

By expanding the state-error equation, Equation 2.15, using a Taylor series as well as substituting in Equation 2.21 along with its time derivatives, we obtain the solution as

$$\delta\mathbf{x}(t) = \left[\mathbf{I} + \mathbf{F}(t)t_{go} + \frac{1}{2}\mathbf{F}(t)^2 t_{go}^2 + ...\right]\delta\mathbf{x}_o = \mathbf{\Phi}\delta\mathbf{x}_o \tag{2.23}$$

where $\mathbf{I}$ is a 6×6 identity matrix, $\delta\mathbf{x}_o$ is the initial relative or state error state, t_{go} is the change in time from the initial state to the final desired state, and $\mathbf{\Phi}$ is the state transition matrix. This solution is used for the evolution of the relative-orbit error state. The state transition matrix used for estimating the relative state is given by

$$\mathbf{\Phi} =$$

$$\begin{bmatrix}
1+\frac{3\mu_\odot x_S^2 t_{go}^2}{2r_S^5}-\frac{\mu_\odot t_{go}^2}{2r_S^3} & \frac{3\mu_\odot x_S y_S t_{go}^2}{2r_S^5} & \frac{3\mu_\odot x_S z_S t_{go}^2}{2r_S^5} & t_{go} & 0 & 0 \\
\frac{3\mu_\odot x_S y_S t_{go}^2}{2r_S^5} & 1+\frac{3\mu_\odot y_S^2 t_{go}^2}{2r_S^5}-\frac{\mu_\odot t_{go}^2}{2r_S^3} & \frac{3\mu_\odot y_S z_S t_{go}^2}{2r_S^5} & 0 & t_{go} & 0 \\
\frac{3\mu_\odot x_S z_S t_{go}^2}{2r_S^5} & \frac{3\mu_\odot y_S z_S t_{go}^2}{2r_S^5} & 1+\frac{3\mu_\odot z_S^2 t_{go}^2}{2r_S^5}-\frac{\mu_\odot t_{go}^2}{2r_S^3} & 0 & 0 & t_{go} \\
\frac{-\mu_\odot t_{go}}{r_S^3}+\frac{3\mu_\odot x_S^2 t_{go}}{r_S^5} & \frac{3\mu_\odot x_S y_S t_{go}}{r_S^5} & \frac{3\mu_\odot x_S z_S t_{go}}{r_S^5} & 1+\frac{3\mu_\odot x_S^2 t_{go}^2}{2r_S^5}-\frac{\mu_\odot t_{go}^2}{2r_S^3} & \frac{3\mu_\odot x_S y_S t_{go}^2}{2r_S^5} & \frac{3\mu_\odot x_S z_S t_{go}^2}{2r_S^5} \\
\frac{3\mu_\odot x_S y_S t_{go}}{r_S^5} & \frac{-\mu_\odot t_{go}}{r_S^3}+\frac{3\mu_\odot y_S^2 t_{go}}{r_S^5} & \frac{3\mu_\odot y_S z_S t_{go}}{r_S^5} & \frac{3\mu_\odot x_S y_S t_{go}^2}{2r_S^5} & 1+\frac{3\mu_\odot y_S^2 t_{go}^2}{2r_S^5}-\frac{\mu_\odot t_{go}^2}{2r_S^3} & \frac{3\mu_\odot y_S z_S t_{go}^2}{2r_S^5} \\
\frac{3\mu_\odot z_S x_S t_{go}}{r_S^5} & \frac{3\mu_\odot y_S z_S t_{go}}{r_S^5} & \frac{-\mu_\odot t_{go}}{r_S^3}+\frac{3\mu_\odot z_S^2 t_{go}}{r_S^5} & \frac{3\mu_\odot z_S x_S t_{go}^2}{2r_S^5} & \frac{3\mu_\odot z_S y_S t_{go}^2}{2r_S^5} & 1+\frac{3\mu_\odot z_S^2 t_{go}^2}{2r_S^5}-\frac{\mu_\odot t_{go}^2}{2r_S^3}
\end{bmatrix} \tag{2.24}$$

where t_{go} is the time-to-go, x_S, y_S, and z_S are the position components for the spacecraft, and r_S is the magnitude of the spacecraft's position vector. However, for simplification, the state transition matrix, $\mathbf{\Phi}$, will be set into four 3x3 matrices, as follows:

$$\mathbf{\Phi} = \begin{bmatrix} \mathbf{\Phi}_1 & \mathbf{\Phi}_2 \\ \mathbf{\Phi}_3 & \mathbf{\Phi}_4 \end{bmatrix} \tag{2.25}$$

Completing the matrix multiplications, we obtain the expression of the relative position at a final time given an initial relative position as

$$\mathbf{r}\left(t_f\right) \approx \tilde{\mathbf{r}}_{t_f} = \mathbf{\Phi}_1(t)\mathbf{r}(t)+\mathbf{\Phi}_2(t)\dot{\mathbf{r}}(t) \tag{2.26}$$

The unit vector of the estimated final state vector is written as

$$\hat{\mathbf{\Lambda}}_c = \frac{\tilde{\mathbf{r}}_{t_f}}{\|\tilde{\mathbf{r}}_{t_f}\|_2} \tag{2.27}$$

Since the predicted final relative position is calculated, the required change in velocity can be estimated. It is assumed that the relative velocity of the spacecraft and asteroid has a very small change. By assuming the unchanging relative velocity, the required approximated change in velocity is found as

$$\delta \mathbf{v} = \frac{\tilde{\mathbf{r}}_{t_f}}{\|\tilde{\mathbf{r}}_{t_f}\|_2} V_c - \tilde{\mathbf{v}} \tag{2.28}$$

where $\tilde{\mathbf{v}}$ is the approximation of the relative velocity. The expression for $\tilde{\mathbf{v}}$ can be found by using the state transition matrix or estimated by using a combination of the line of sight and line of sight rate. By using the latter, the expression for the estimation for the relative velocity is

$$\tilde{\mathbf{v}} = -V_c t_{go} \dot{\mathbf{\Lambda}}(t) - V_c \hat{\mathbf{\Lambda}}(t) \tag{2.29}$$

By substituting Equations 2.27 and 2.29 into Equation 2.28, the final approximation for the change in velocity is found as

$$\delta \mathbf{v} = V_c \left(\hat{\mathbf{\Lambda}}_c + t_{go} \dot{\mathbf{\Lambda}}(t) + \hat{\mathbf{\Lambda}}(t) \right) \tag{2.30}$$

With the required estimation of velocity change, the command acceleration may also be found. What must be commanded is along the same unit vector as the change in velocity and can then be written as

$$\mathbf{u} = T_{max} \frac{\delta \mathbf{v}}{\|\delta \mathbf{v}\|_2} \tag{2.31}$$

where T_{max} is the maximum amount of thrust available by the guidance system. Further details on the state transition matrix and velocity change derivations can be found in [16, 27].

2.3.2.1 Preplanned Pulses

Since the KI guidance is a predictive scheme and calculates a required change in velocity to intercept a target at a given time, it may be used to determine preplanned pulses. This is one of the advantages that KI has over PN. The number of pulses desired is

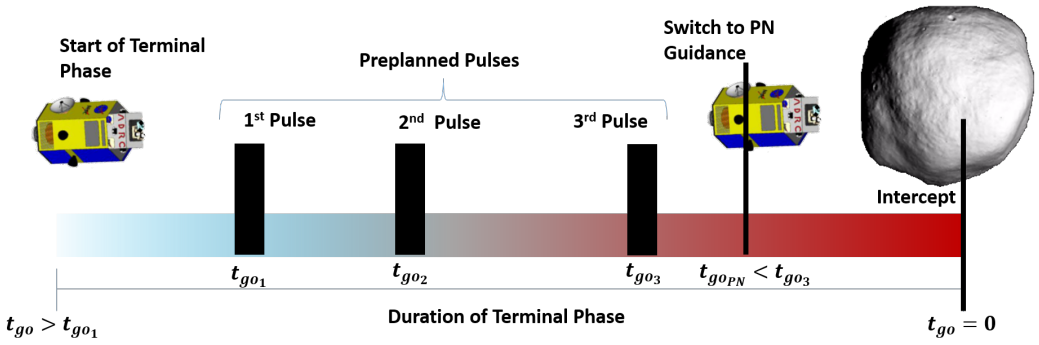

Figure 2.4: Hybrid guidance scheme illustrating the use of 3 preplanned KI pulses. The variable t_{go} represents the time-to-go until asteroid intercept.

user defined. At each pulse, there is an associated time before intercept, which correlates to the time-to-go. When time-to-go reaches the pulse triggering time and the estimated change in velocity is greater than or equal to the allowed thruster velocity change, then the thrusters are turned on and provide maximum thruster output, T_{max}. However, if the reference model is not accurate, then the required velocity change will reflect the poor model. Incorporating sensor information will help create a better estimation for the LOS rate. This will be further discussed later in this chapter.

2.3.3 The KI/PN Hybrid Concept

The KI/PN hybrid concept incorporates the preplanned pulses associated with KI guidance and the continuous firing of the PN guidance. During the beginning portion of the terminal phase for asteroid intercept, the spacecraft uses the preplanned KI pulses, and once the time-to-go is less than a certain amount, the spacecraft then switches over to PN. An illustration can be seen in Figure 2.4. By implementing PN, it ensures that the target will be intercepted due to the continuous nature of the guidance scheme. However, the target may not always be intercepted due to the thruster limitations. Incorporating a Schmitt trigger onto the continuous PN will create realistic capabilities given by an impulsive thruster. Possible advantages of using a hybrid scheme are observed herein and briefly discussed in [28].

2.4 Higher Order LOS Rate Approximations

A higher order estimation for the LOS rate, using a greater number of previous LOS measurements, can be found by using the general form of a Taylor series expansion and backward differencing [24, 25]. The second-order derivative expansion of a general equation's derivative is given by

$$F'(x) = \frac{F(x) - F(x-h) + \frac{1}{2}h^2 F''(x)}{h} \tag{2.32}$$

where $F(x)$ is a given function at time x, and h is the time between the current (first) and previous (second) sample. The primes denote the time derivative. The second time derivative requires more Taylor series terms and manipulation, but can be found by substitution and finite differencing as

$$F''(x) = \frac{mF(x) - (m+h)F(x-h) + hF(x-h-m)}{mh^2} \tag{2.33}$$

where m is the time between the second sample and the third sample. If all of the times between samples are equal, which can be represented by h, then Equation 2.33 can be simplified as

$$F''(x) = \frac{F(x) - 2hF(x-h) + F(x-2h)}{h^2} \tag{2.34}$$

Equation 2.34 can be substituted into Equation 2.32 when desired. The second-order approximation for rate is given by

$$F_2'(x) = \frac{3F(x) - 4F(x-h) + F(x-2h)}{2h} \tag{2.35}$$

where the subscript 2 denotes the second-order approximation. For the general case formulation, as seen in [26], the approximation of a derivative using expansions can be written as

$$\frac{\partial^q N}{\partial x^q} \approx \sum_{i=1}^{p} \gamma_i N_i \tag{2.36}$$

where q denotes the derivative, p is the number of samples, γ_i is the ith coefficient, and N is the function. When $i = 1$, it represents the first sample where as $i = p$ represents the current sample. Then the Taylor series expansion of N_i is

$$N_i = N_* + (x_i - x_*)\frac{\partial N_*}{\partial x_*} + \frac{1}{2!}(x_i - x_*)^2\frac{\partial^2 N_*}{\partial x_*^2} + \frac{1}{3!}(x_i - x_*)^3\frac{\partial^3 N_*}{\partial x_*^3} + ... \tag{2.37}$$

where the * subscript denotes the point at which the derivatives are desired. Substituting Equation 2.37 into Equation 2.36 results in the expansion of the approximation

$$\frac{\partial^q N}{\partial x^q} \approx \sum_{i=1}^{p}\gamma_i N_i = \sum_{i=1}^{p}\gamma_i N_* + \sum_{i=1}^{p}\gamma_i (x_i - x_*)\frac{\partial N_*}{\partial x_*} + \sum_{i=1}^{p}\gamma_i \frac{1}{2!}(x_i - x_*)^2\frac{\partial^2 N_*}{\partial x_*^2} + ... \tag{2.38}$$

From inspection, it can be seen that this expansion can be written in terms of partial derivative coefficients

$$\sum_{i=1}^{p}\gamma_i N_i = B_0 N_* + B_1\frac{\partial N_*}{\partial x_*} + B_2\frac{\partial^2 N_*}{\partial x_*^2} + ... \tag{2.39}$$

where

$$B_n = \sum_{i=1}^{p}\gamma_i (x_i - x_*)^n \quad \text{for } n = 0, 1, ..., q-1 \tag{2.40}$$

The factorial of n can be multiplied to the side of the coefficient B_n. By doing, it allows for the formulation of a set of linear equations to solve for the function coefficients, γ_i. A matrix representation, using Einstein notation, is given by

$$(k-1)!B^k = A_j^k\gamma^j \tag{2.41}$$

where k is the row index and j is the column index. The transformation matrix, A, is expressed as

$$A_j^k = (x_{p-j} - x_*)^{(k-1)} \tag{2.42}$$

It can be noted, in the case for backward differencing, when $k = 1$ and $j = p$, the equation is 0^0, which in this case, is equal to one. When solving for a desired derivative, q, set $B_{q-1} = 1$ and the rest to 0. For example, when wanting the second-order approximation

for the first derivative using backward differencing, $q = 3$, p goes from 1 to 3, and j goes from 1 to 3. The full matrix representation is

$$\begin{bmatrix} B_0 \\ B_1 \\ 2B_2 \end{bmatrix} = \begin{bmatrix} 1 & 1 & 1 \\ (x_2-x_*) & (x_1-x_*) & (x_0-x_*) \\ (x_2-x_*)^2 & (x_1-x_*)^2 & (x_0-x_*)^2 \end{bmatrix} \begin{bmatrix} \gamma_1 \\ \gamma_2 \\ \gamma_3 \end{bmatrix}$$

if the time between the second and third sample is equal, the single increment can be given as before, h. The matrix form can be simplified by replaying the components of A and by desiring the first derivative

$$\begin{bmatrix} 0 \\ 1 \\ 0 \end{bmatrix} = \begin{bmatrix} 1 & 1 & 1 \\ -2h & h & 0 \\ (-2h)^2 & (-h)^2 & 0 \end{bmatrix} \begin{bmatrix} \gamma_1 \\ \gamma_2 \\ \gamma_3 \end{bmatrix}$$

from this point, the system of equations can be solved. By replacing these quantities and solving the system of equations, the solution is

$$\begin{bmatrix} \gamma_1 \\ \gamma_2 \\ \gamma_3 \end{bmatrix} = \begin{bmatrix} \frac{1}{2h} \\ \frac{-2}{h} \\ \frac{3}{2h} \end{bmatrix}$$

Replacing these coefficients into the newly bounded Equation 2.36 gives

$$\frac{\partial N}{\partial x} \approx \sum_{i=1}^{3} \gamma_i N_i = \frac{1}{2h} N_1 - \frac{2}{h} N_2 + \frac{3}{2h} N_3$$

Recall that γ_1 refers to the first sample while γ_3 refers to the current sample. This means that $N_1 = N_{-2}$, $N_2 = N_{-1}$, and $N_3 = N_0$. Manipulating to give a common denominator results in

$$\frac{\partial N}{\partial x} \approx \frac{N_{-2} - 4N_{-1} + 3N_0}{2h}$$

This equation is exactly what was found in Equation 2.35. The same process can be applied to any order of derivative approximation as well as other differencing methods.

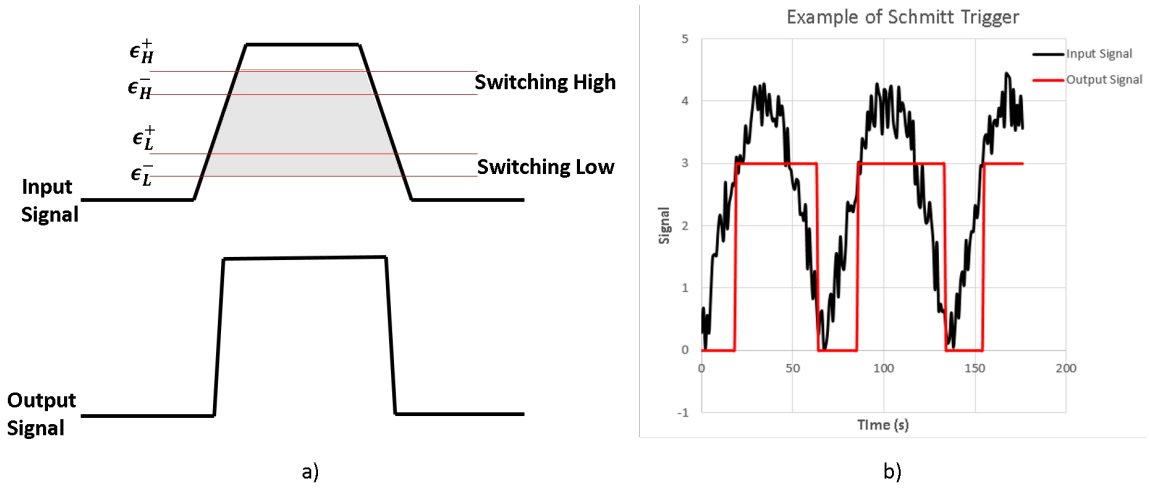

Figure 2.5: a) Depiction of Schmitt trigger changing function into a square signal output (in ideal situations, $\epsilon_H^+ = \epsilon_H^-$ and $\epsilon_L^+ = \epsilon_L^-$) and b) Example of Schmitt trigger on a noisy repeating signal.

2.5 Schmitt Trigger and Thrust Limiter

While computing the required spacecraft command acceleration for the guidance schemes herein, the given thruster's output may not be able to fulfill the requirements due the calculated thrust being higher than the maximum thrust available from thrusters. A solution to help remedy this situation, as well as help reject noise, is to implement a Schmitt trigger. Structure of this trigger can be seen in Figure 2.5 a). The Schmitt trigger converts an input signal into a square function based off of an upper and lower threshold. Once the upper threshold of the trigger is met, max threshold is commanded. If the output falls below the lower threshold, the output is zero. By requiring the information of the last step's "on" or "off" command, the output then becomes delayed. An illustration and example can be seen in Figure 2.5. In the repeating wave example in Figure 2.5 b), it can be seen that, if the thruster is not throttleable, the trigger creates a more reasonable thruster firing sequence. However, as previously stated, the firing output is slightly delayed due to the thruster having to be switched on once the max threshold is reached.

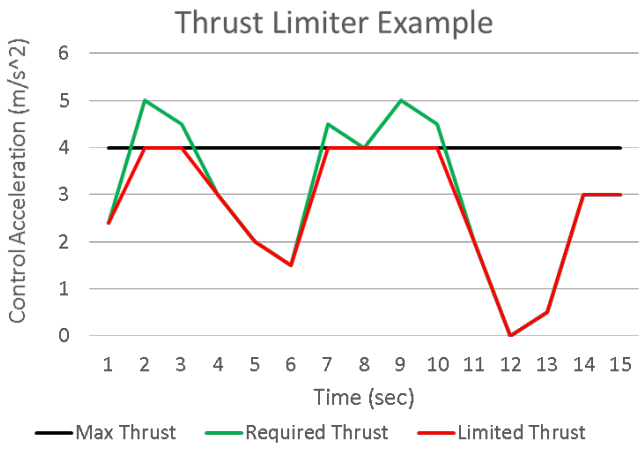

Figure 2.6: An example showing the thrust limiter concept.

Another option to consider is to use a thruster limiter. This allows for the thrusters to have a variable output which ranges from zero to device max. The needed command acceleration from the guidance control scheme is used as input into the limiter. If the needed acceleration is greater than what the device can handle, the max is allowed. However, a disadvantage is that the thruster needs to have the ability to vary. Some thrusters only operate under the fully on or off conditions. An example of a working thruster limiter can be seen in Figure 2.6. A lower bound, if needed, may be applied. In this case, the limiter would turn off once it is above the upper limit and below the lower limit. This differs from the Schmitt trigger by the guidance scheme required acceleration not having the need to reach the upper bound to switch on, but only needing to reach the trigger's lower limit.

2.6 Image Line-of-Sight

The image line-of-sight (LOS) is the directional vector from the spacecraft to the target object, which is determined by the current estimated LOS given by trajectory models, and the object's pixel centroid located on the image plane. However, the camera frame first needs to be established. Since the LOS vector and the spacecraft position

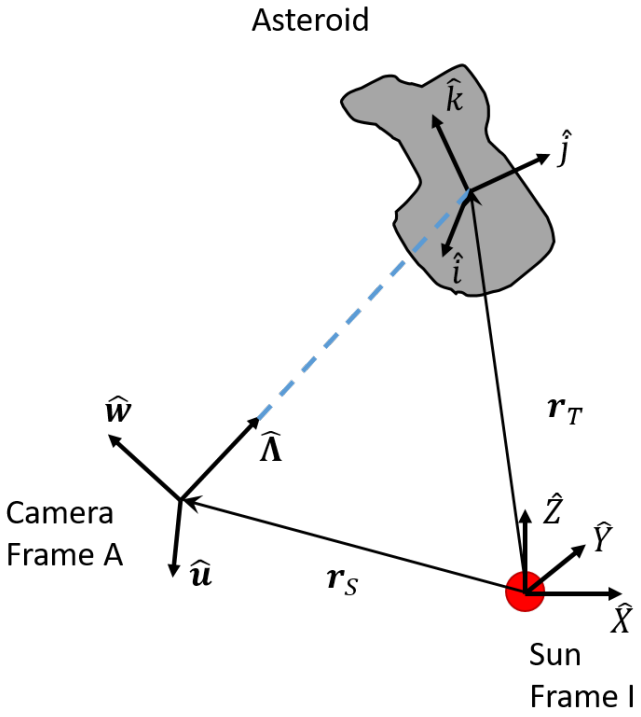

Figure 2.7: Illustration of the spacecraft's camera frame.

are known, the camera frame can be constructed. For simplicity, the image plane is perpendicular to the line of sight vector and can be defined by the two unit vectors as follows:

$$\hat{\mathbf{w}} = \hat{\mathbf{\Lambda}} \times \frac{\mathbf{r}_S}{r_S} \quad \text{and} \quad \hat{\mathbf{u}} = \hat{\mathbf{\Lambda}} \times \hat{\mathbf{w}} \tag{2.43}$$

By using this definition, the transformation matrix which maps the camera frame directly to the global frame is computed as

$$C^{I/A} = \left[\hat{\mathbf{u}}, \quad \hat{\mathbf{w}}, \quad \hat{\mathbf{\Lambda}}\right]_{3\times 3} = \begin{bmatrix} u_1 & w_1 & \Lambda_1 \\ u_2 & w_2 & \Lambda_2 \\ u_3 & w_3 & \Lambda_3 \end{bmatrix} \tag{2.44}$$

where I represents the inertial frame, A represents the camera frame, and the subscripts denote the components of its corresponding unit vector described by LOS and the perpendicular plane definition in 2.43. A depiction of the orientations can be seen in Figure 2.7. The camera frame plane, which is perpendicular to $\hat{\mathbf{\Lambda}}$ and parallel to the plane

Table 2.1: Example of camera parameters with resulting pixel resolution

	Camera 1	Camera 2	Camera 3	Camera 4
Resolution (m×n)(pixels)	1024 × 1024	1024 × 1024	512 × 512	256 × 256
Focal length (mm)	4000	1800	1800	1800
Sensor array size (U×W) (μm)	18 × 18	18 × 18	36 × 36	30 × 30
Horizontal Field of View (FOV_h) (radians)	4.61×10^{-3}	10.2×10^{-3}	5.1×10^{-3}	4.3×10^{-3}
Vertical Field of View (FOV_v) (radians)	4.61×10^{-3}	10.2×10^{-3}	5.1×10^{-3}	4.3×10^{-3}
Horizontal pixel resolution at 100 km (m)	0.450	1.00	2.00	1.67
Vertical pixel resolution at 100 km (m)	0.450	1.00	2.00	1.67

created by $\hat{\mathbf{w}}$ and $\hat{\mathbf{u}}$, is then broken up into a number of horizontal and vertical pixels. Pixel count in the vertical and horizontal directions do not need to be equal. Each pixel has a resolution at a certain distance, which is based off of the focal length of the system when using a pinhole camera, and is given by

$$h_{pix} = \frac{\|\mathbf{r}\|_2 U}{m\ F} \quad \text{and} \quad v_{pix} = \frac{\|\mathbf{r}\|_2 W}{n\ F} \tag{2.45}$$

where h_{pix} is the horizontal pixel resolution, v_{pix} is the vertical pixel resolution, U is a sensor array's horizontal width, W is a sensor array's vertical height, m is the number of horizontal pixels, n is the amount of vertical pixels, and F is the system's focal length. Similarly, the pixel resolution can be found using the angular resolution incorporating the vertical and horizontal field-of-views (FOV)

$$h_{pix} = \frac{2\,\|\mathbf{r}\|_2 \tan\left(\frac{FOV_h}{2}\right)}{m} \quad \text{and} \quad v_{pix} = \frac{2\,\|\mathbf{r}\|_2 \tan\left(\frac{FOV_v}{2}\right)}{n} \tag{2.46}$$

where, in general, the FOV, using S as a sensor dimension length, can be found by

$$FOV = 2\ \text{atan}\left(\frac{S}{2F}\right) \tag{2.47}$$

Table 2.1 shows pixel resolution at different ranges for varying pixel arrays and focal lengths. With this information and a pixel location for the object to target, the new

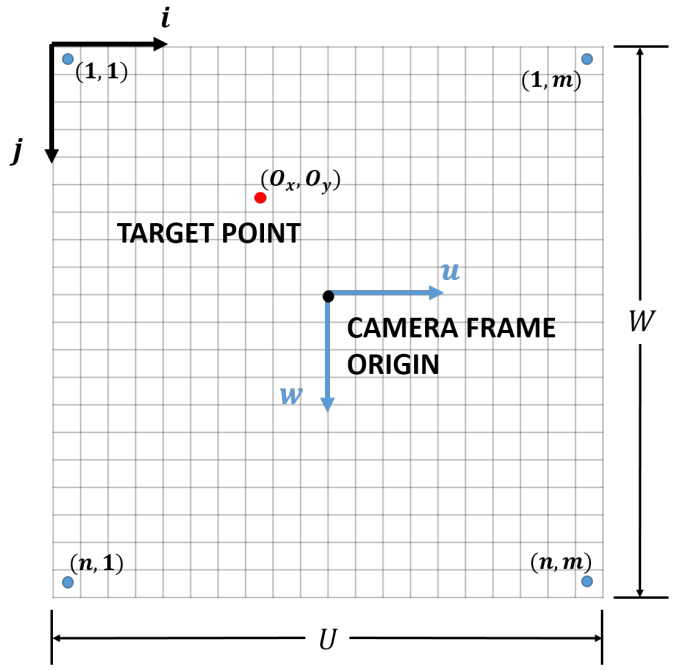

Figure 2.8: Diagram illustrating the set up of the pixel and camera frame.

target location base from the image can be found as

$$\tilde{\mathbf{r}} = \mathbf{r} - C^{I/A} \begin{bmatrix} \left(O_x - \frac{m}{2}\right) h_{pix} \\ \left(O_y - \frac{n}{2}\right) v_{pix} \\ 0 \end{bmatrix} \tag{2.48}$$

where O_x and O_y are the horizontal and vertical targeted pixel location on the image. Figure 2.8 illustrates the sensor array and pixel targeted location. As long as the orientation of the pixel plane and the image coordinates remain parallel, ascending $\hat{\mathbf{i}}$ and $\hat{\mathbf{j}}$ are in the same direction as $\hat{\mathbf{u}}$ and $\hat{\mathbf{w}}$, the above equation holds. Further discussion of how to determine the horizontal and vertical targeted location is found in Chapter 4. The image LOS is then obtained as

$$\hat{\mathbf{\Lambda}}_I = -\frac{\tilde{\mathbf{r}}}{\|\tilde{\mathbf{r}}\|_2} \tag{2.49}$$

During the computation of the required spacecraft acceleration, $\hat{\mathbf{\Lambda}}_I$ replaces $\hat{\mathbf{\Lambda}}$. This is the case for any of the guidance control schemes.

CHAPTER 3. VISIBLE/INFRARED SENSOR MODELING AND TERMINAL GUIDANCE SIMULATION FOR A SINGLE KINETIC-ENERGY IMPACTOR VEHICLE

3.1 Introduction

The Asteroid Deflection Research Center (ADRC) at Iowa State University has been developing a Hypervelocity Asteroid Intercept Vehicle (HAIV) concept to mitigate the impact threat of hazardous asteroids with short warning time [31, 32, 33]. An illustration of the proposed HAIV terminal intercept scenario is provided in Figure 3.1. To demonstrate the feasibility of such a mission, a scaled polyhedron model of 433 Eros was used in [34] for a closed-loop optical navigation and guidance simulation study of the HAIV concept. Similar concepts for hypervelocity asteroid intercepts using visual imaging autonomous guidance have been considered, such as the Don Quijote mission [35, 36], Asteroid Impact and Deflection Assessment (AIDA) [37], and the Impactor for Surface and Interior Science (ISIS) [38]. Visual based guidance has been demonstrated in [39] and [40]. However, when visual tracking of a target is not available, an IR telescope/sensor might be required for a precision impact and mission success. It can be seen in Figure 3.2 that size, with slight contribution from albedo, will affect the asteroid's signature in the IR regime, whereas for visible electromagnetic wavelengths, asteroid size and albedo play a key role in object detection and observation.

An IR sensor array has been employed for the Exoatmospheric Kill Vehicle (EKV). This vehicle is designed to intercept ballistic missiles at hypervelocity speeds [41]. The

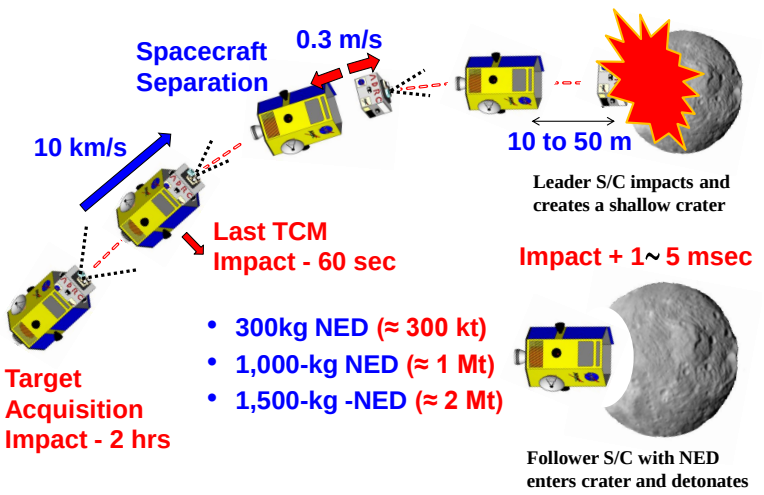

Figure 3.1: A baseline terminal intercept scenario of a two-body HAIV carrying a nuclear explosive device (NED).

on-board focal plane array used for EKV targeting consists of a 256 by 256 structure with pixel pitch of 30 μm, which is sensitive to IR emission belonging to a wavelength range of 7 to 30 micrometers [42]. During the EKV targeting process, the spacecraft receives information from the long-wave IR sensor of the Space Based Infrared System (SBIRS) in low Earth orbit. By using the SBIRS, the detection range of the system is said to be about 10^7 kilometers for an object emitting 6×10^8 W/Ster. However, signal-to-noise ratios (SNR) vary depending on the probability of detection [43]. The EKV houses a 30-centimeter diameter optical system, which, with the IR detector, has an approximate detection range of 2000 kilometers [44].

It has been shown in [46] that physical models are needed to estimate the SNR for a given detector and asteroid scenario in the N-band of IR wavelength. This formulation used an alternative definition for the SNR. A reference IR telescope, the Wide-field Infrared Survey Explorer (WISE), uses a Cassegrain-like primary mirror to collect signal from objects of interest. A WISE telescope illustration can be seen in Figure 3.3 [47]. This chapter is based on the author's journal article [45].

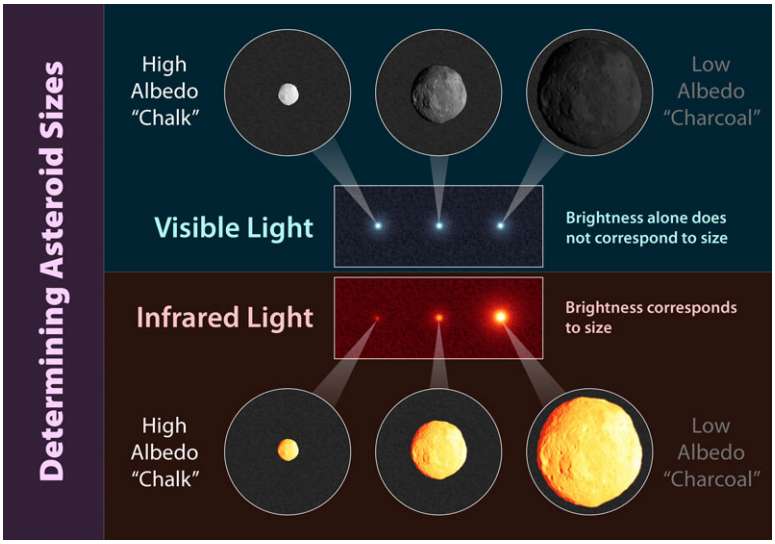

Figure 3.2: Comparisons of optical and infrared images of asteroids with different sizes and albedos. Image courtesy of http://wise.ssl.berkeley.edu/gallery_asteroid_sizes.html.

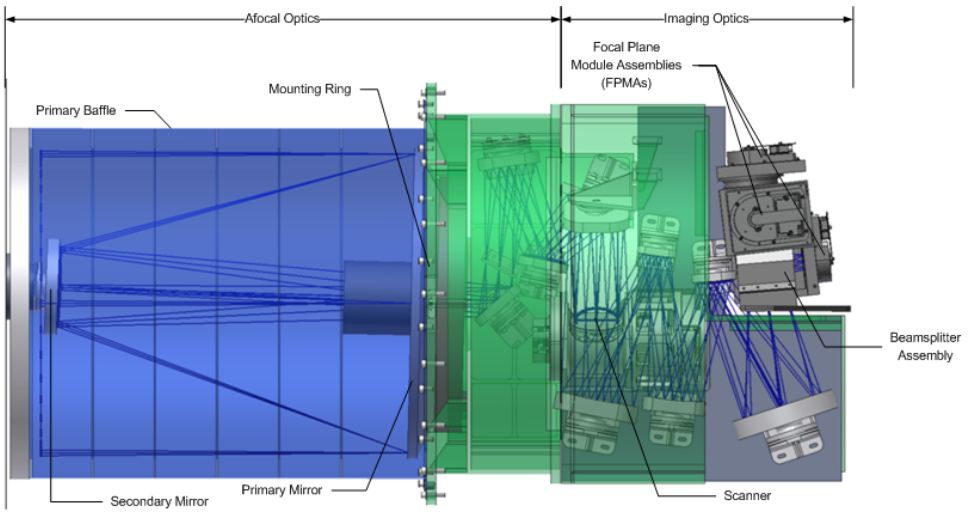

Figure 3.3: Illustration of WISE telescope. Image courtesy of NASA/JPL.

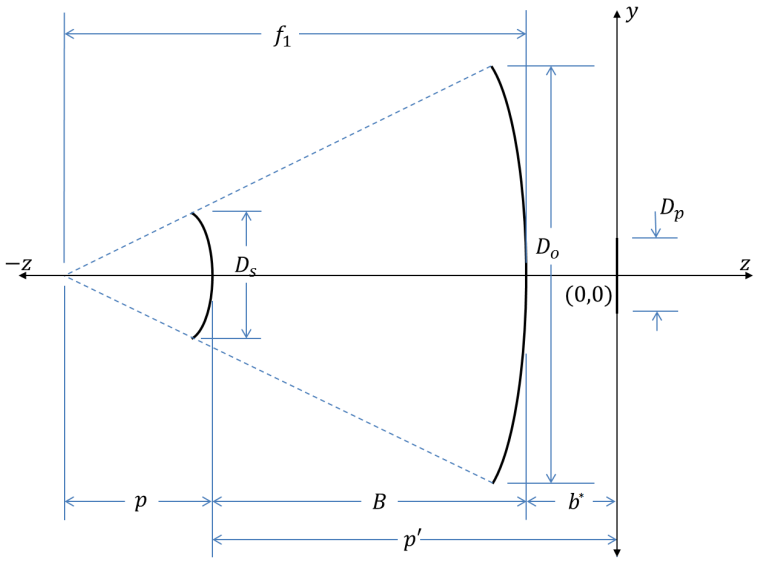

Figure 3.4: Classical Cassegrain telescope design.

3.2 Optics and Sensors

Three types of sensors, along with their optical configurations, are studied for possible implementation to the HAIV. The instruments of interest herein are a visible band sensor, an IR sensor, and a radar device. Typical parameters of these sensors are determined by estimating the SNR, which corresponds to a minimum or maximum detection distance, and characteristics of the optics to be implemented.

3.2.1 Classical Cassegrain Telescope

A classical Cassegrain telescope design is considered due to its simplicity and similarity to the NEOWISE infrared telescope design. An illustration of the Cassegrain telescope is given in Figure 3.4, which will be the basis of the instrument's parameters. Given an effective focal length, a primary mirror focal length and diameter, and a back focus distance, telescope parameters are determined. It can be seen that baffling and glare stops are not considered.

A first parameter calculation can be done to determine the magnification of the system, given both overall system and primary mirror focal lengths. The magnification of the system is

$$M = \frac{F}{f_1} \tag{3.1}$$

where F and f_1 are the system focal length and the primary mirror focal length. Once magnification is calculated, other parameters of this system are found. Given the back focus (distance from the primary mirror to the focal plane), b^*, the primary mirror focus intercept point is found as

$$p = \frac{F+b^*}{M+1} \tag{3.2}$$

The overall distance from the secondary mirror to the focal plane, also known as the secondary to Cassegrain focus p', is given by

$$p' = pM \tag{3.3}$$

From the Cassegrain focus, the mirror separation, B, is found as

$$B = p'-b^* \tag{3.4}$$

Another very important part of the Cassegrain telescope is to design the size of the secondary mirror. This diameter, D_s, can be found as

$$D_s = \frac{pD_o}{f_1}+\frac{BD_p}{f_1 M} \tag{3.5}$$

where D_p is the minimum diameter of the image plane (not including thickness) and D_o is the primary mirror diameter. This correlates to the size of the imaging device, which is equivalent to the minimum dimension of the array. Equations 3.2 and 3.5 are given in Beish [48].

The radius of curvature (ROC) is found for both, the primary mirror and secondary mirror and is given by

$$R_1 = 2f_1 \tag{3.6}$$

and

$$R_2 = \frac{2}{\frac{1}{p} - \frac{1}{p'}} \tag{3.7}$$

where R_1 is the ROC for the primary mirror and R_2 is the ROC for the secondary mirror [49, 50]. By using the ROC of each mirror, the prescription for the two mirrors can be found by the formulas

$$z_1 = \frac{y_1^2}{2R_1} - b^* \tag{3.8}$$

$$z_2 = \frac{y_2^2/R_2}{1+\sqrt{1-(1+b_2)(y_2/R_2)^2}} - (b^*+B) \tag{3.9}$$

and

$$b_2 = \frac{-4M}{(M-1)^2} - 1 \tag{3.10}$$

where z_1 and z_2 are face locations of the mirrors when the image plane array is located at the origin of a measurement, $\frac{-D_o}{2} \leq y_1 \leq \frac{-D_0}{2}$, and $\frac{-D_s}{2} \leq y_2 \leq \frac{-D_s}{2}$ [50]. This is only valid in the case of a Classical Cassegrain telescope.

3.2.2 Visible Band Sensor

A visible band sensor is characterized herein. The first step of estimating the SNR is to integrate Planck's law for black body radiation over the visible band of electromagnetic spectrum, which gives the radiance. Figure 3.5 illustrates the black body curves for the IR regime of interest for the electromagnetic spectrum. An assumption is made where IR and visible waves are not transmitted through the body and only reflected energy

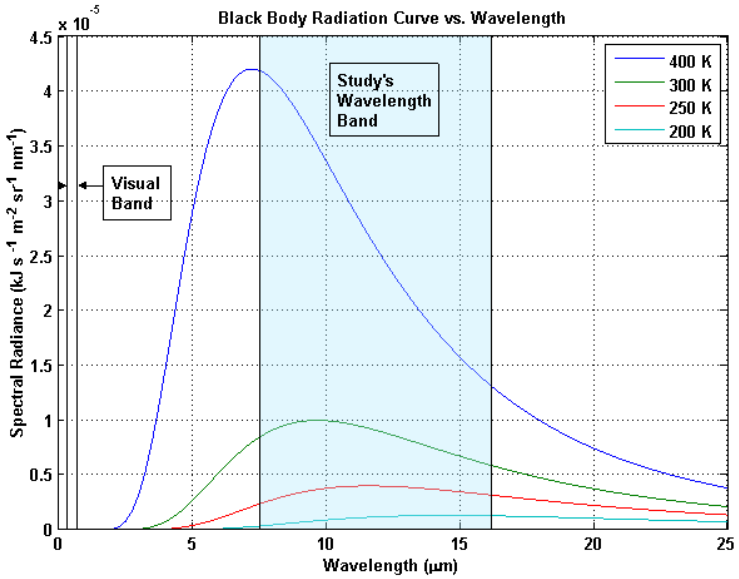

Figure 3.5: Black body radiation for different temperature values in the IR regime.

and emitted energy are considered. Below is the formulation of radiance ($\mathrm{Wm^{-2}sr^{-1}}$) and irradiance ($\mathrm{Wm^{-2}}$) for reflected energy. Radiance is given by

$$L_{Vs_i} = \int_{\lambda_1}^{\lambda_2} \frac{2hc^2}{\lambda^5} \frac{1}{e^{\frac{hc}{k_B T_{sun} \lambda}} - 1} d\lambda \tag{3.11}$$

where the temperature of interest is that of the sun, h is the Planck's constant ($6.6260695710^{-34}\mathrm{m^2kgs^{-1}}$) c is the speed of light, k_B is the Boltzmann constant ($1.380648810^{-23}\mathrm{m^2kgs^{-2}K^{-1}}$), λ_1 is the lower bound wavelength, and λ_2 is the upper bound wavelength. Since this is calculated, one must evaluate the radiance of the sun at the body, which is the irradiance multiplied by the sun's solid angle. A solid angel of an object is the area of its projection onto a sphere with some arbitrary radius corresponding to the distance between objects and is measured in steradians [52]. In this case, the radius is the distance from the sun to the object. However, the radius can also be from the object to the spacecraft, as will be used in the infrared situation. An assumption is made that the sun's solid angle can use a circular approximation, since the asteroid's distance from the sun is much larger than the radius of the sun. This leads to the incident irradiance at the object as

$$E_{Vs_i} = L_{Vs_i} \frac{\pi r_s^2}{d_{s/obj}^2} \tag{3.12}$$

where r_s is the radius of the sun and $d_{s/obj}$ is the distance from the sun to the object. The irradiance of the reflected electromagnetic waves, from the object as seen by the spacecraft, is given by

$$E_{V_{reflected}} = \frac{\alpha_V}{\pi} E_{Vs_i} \Omega_{reflected} \tag{3.13}$$

where α_V is the asteroid's visible albedo, $\Omega_{reflected}$ is the solid angle for reflected irradiance, and $d_{obj/sc}$ is the distance from the object to the spacecraft. The inclusion of a factor of $1/\pi$ is due to the assumption of a Lambertian surface, which has a relation between irradiance and radiance due to the formulation of existence [51]. Since the reflected energy's irradiance is estimated, the emitted energy from the object must be calculated.

The emitted energy from the body is very similar to reflected energy obtained by an integration of Planck's law using the asteroid temperature. A typical asteroid temperature, for objects approximately 1 AU away from the sun, is 300 K [53]. This will be used later for detection distances and simulations. The equation for emitted radiance is given by

$$L_{V_{emitted}} = \epsilon_V \int_{\lambda_1}^{\lambda_2} \frac{2hc^2}{\lambda^5} \frac{1}{e^{\frac{hc}{k_B T_{obj} \lambda}} - 1} d\lambda \tag{3.14}$$

where ϵ_V is the object's visible emissivity. This assumes that there is no transitivity, which is the case for the infrared band as well. Once again, the irradiance can be found by multiplying the radiance by the solid angle (circular approximation), as follows:

$$E_{V_{emitted}} = L_{V_{emitted}} \Omega_{emitted} \tag{3.15}$$

where $\Omega_{emitted}$ is the solid angle for emitted irradiance. The total irradiance seen by the spacecraft is then given by

$$E_V = E_{V_{reflected}} + E_{V_{emitted}} \tag{3.16}$$

In general, the irradiance at the spacecraft from the visible emission can be neglected, therefore $E_{V_{emitted}} \approx 0$. From the irradiance, the photon flux, given in number of photons per square meter per second, is calculated as follows:

$$\Phi_V = \frac{E_V \lambda_{max}}{hc} \tag{3.17}$$

where λ_{max} is the wavelength of peak emission, which is a function of Wien's displacement constant and the Sun's temperature. By collecting the device parameters and the photon flux at the device, the signal given on the pixel array in number of electrons is obtained as

$$S_{V_{signal}} = \Phi_V \tau_{opt} \eta G_V \tau_{int} N \pi \left(\frac{D_o}{2}\right)^2 \tag{3.18}$$

where a_{opt} is a coefficient from the optics, τ_{opt} is the optics' efficiency, η is the device's quantum efficiency, G_V is the device's photoconductive gain, τ_{int} is the device's integration time, N is the number of image samples, and D_o is the diameter of the primary mirror or lens. A similar expression can be found in [54]. Equation 3.18 is also used in IR signal formulation, which has IR specific variables. For the SNR to be calculated, the estimated standard deviations of the noise are found. The shot noise characteristics of the device are dictated by the following expression:

$$\sigma_{V_{shot}} = \sqrt{S_{V_{signal}}} \tag{3.19}$$

where the standard deviation is in number of electrons and follows Poisson statistics. Another noise contribution is caused by dark current. This noise also follows Poisson statistics and also is dictated by Arrhenius equations in the form of $D = \kappa_1 e^{\left(\frac{\kappa_2}{T}\right)}$, where T is the sensor temperature, κ_2 represents a function of the activation energy of the material, and κ_1 is the dark count per pixel per second. Using pixel 3 information found in [55], the parameters κ_1 and κ_2 can be calculated, which will be discussed later. These

variables however, are sensor and pixel specific. The dark current standard deviation can then be written as

$$\sigma_{V_{dark}} = \sqrt{\frac{\kappa_1 n_{pix} \tau_{int} N e^{\left(\frac{\kappa_2}{T_d}\right)}}{D_V}} \tag{3.20}$$

where D_V is the dark count to electron conversion gain found in [56], T_d is the detector temperature, and n_{pix} is the total number of pixels. Similar forms of Equations 3.19 and 3.20 are found in [61]. These equations will also be applied to the IR sensor. Since these noise values are assumed to be statistically independent, the total noise standard deviation is described as

$$\sigma_{V_{noise}} = \sqrt{\sigma^2_{V_{shot}} + \sigma^2_{V_{dark}} + R_r^2} \tag{3.21}$$

where R_r is the read-in noise. This value is usually given as an RMS value measured in number of electrons. The final expression for the SNR in the visible band becomes

$$SNR_V = \frac{S_{V_{signal}}}{\sigma_{V_{noise}}} \tag{3.22}$$

3.2.3 Infrared Sensor

Similar to the visible band sensor, the IR device is simulated by also using Planck's law of black body radiation, which is integrated over the infrared wavelengths. However, the emissivity is taken into account. In Figure 3.5, black body radiation curves for different asteroid temperatures are shown, and the band in a transparent blue represents the infrared wavelengths of this study. Two types of infrared sensors will be discussed, photon detectors and thermal detectors.

3.2.3.1 Photon Detector

Photon detectors collect photons at a certain wavelength and directly convert the photons to a number of electrons with a device quantum efficiency. These electrons are

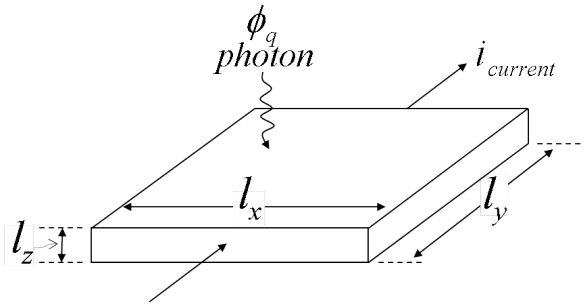

Figure 3.6: A simple diagram of sensor pixel characteristics.

then interpreted by the sensor array electronics. A similar method to visible band sensor SNR is followed for the photon detector. The radiance and irradiance for emitted and reflected radiation are given as

$$L_{IR_{emitted}} = \epsilon_{IR} \int_{\lambda_1}^{\lambda_2} \frac{2hc^2}{\lambda^5} \frac{1}{e^{\frac{hc}{k_B T_{obj} \lambda}} - 1} d\lambda \tag{3.23}$$

$$E_{IR_{emitted}} = L_{IR_{emitted}} \Omega_{emitted} \tag{3.24}$$

$$L_{IRs_i} = \int_{\lambda_1}^{\lambda_2} \frac{2hc^2}{\lambda^5} \frac{1}{e^{\frac{hc}{k_B T_{sun} \lambda}} - 1} d\lambda \tag{3.25}$$

$$E_{IR_{reflected}} = \frac{\alpha_{IR}}{\pi} L_{IRs_i} \Omega_{reflected} \frac{\pi r_s^2}{d_{s/obj}^2} \tag{3.26}$$

$$E_{IR} = E_{IR_{emitted}} + E_{IR_{reflected}} \tag{3.27}$$

where ϵ_{IR} is the IR emissivity of the object, α_{IR} is the object's IR albedo, λ_1 and λ_2 are the IR lower and upper bound wavelengths. Note that these equations must be integrated over the infrared spectrum regime of interest. To find the radiance for reflected energy and emitted energy, they are not integrated over the visible spectrum like in Section 3.2.2, but over infrared wavelengths. Following similar steps from that of the visual camera, the photon flux and signal are described as follows:

$$\Phi_{IR} = \frac{E_{IR}\lambda_{max}}{hc} \tag{3.28}$$

$$S_{IR_{signal}} = \Phi_{IR}\tau_{opt}\eta G_{IR}\tau_{int}N\pi\left(\frac{D_{mirror}}{2}\right)^2 \tag{3.29}$$

where the λ_{max} is the wavelength of peak emission, which is a function of Wien's displacement constant and object's temperature and G_{IR} is the IR device gain. With signal photons known, noise characteristics need to be developed.

Four types of noise sources are considered herein: shot noise, dark current noise, Johnson noise, and generation-recombination noise. The standard deviations of each noise can be described as

$$\sigma_{IR_{shot}} = \sqrt{S_{IR_{signal}}} \tag{3.30}$$

Similarly, the dark current noise for the infrared sensor can be expressed int the Arrhenius form. The parameters κ_1 and κ_2 are found by using material specific information. For later comparison to the WISE telescope, a silicon arsenide (Si:Ar) detector is used. Information regarding the dark current electron count per pixel can be found in [57]. However, the Si:Ar detector parameters are that of the James Web Space Telescope's (JWST) Mid-Infrared Instrument (MIRI). This will be discussed in a later section. The dark current noise is then expressed as

$$\sigma_{IR_{dark}} = \sqrt{\frac{\kappa_1 n_{pix}\tau_{int}Ne^{\left(\frac{\kappa_2}{T_d}\right)}}{D_V}} \tag{3.31}$$

where again, D_V is the dark count per electron gain for the detector. To reiterate, the parameters κ_1 and κ_2 in the IR detector are not the same as in Section 3.2.2.

$$\sigma_{IR_{johnson}} = \sqrt{\frac{2k_B n_{pix}T_d\rho l_y NG^2}{l_x l_z R_{sp}^2\tau_{int}}} \tag{3.32}$$

where (l_x, l_y, l_z) are pixel dimensions, R_{sp} is voltage to electron conversion, and ρ is the resistivity. Typical values for R_{sp} can be found in [58]. The resistivity is the inverse

of conductivity and is sensitive to detector temperature. Material information of the Si:Ar detector at low temperatures is taken from [59]. In general, for semiconductors, the resistivity follows an Arrhenius form [60]. An expression for ρ is

$$\rho = \rho_o e^{\frac{E_a}{k_{Be} T_d}} \tag{3.33}$$

where ρ_o is the resistivity as detector temperature goes to infinity, E_a is the material activation energy given in election volts, and k_{B_e} is Boltzmann's constant in electron volts per Kelvin.

$$\sigma_{IR_{GR}} = G\sqrt{2\eta\Phi_{IR}\tau_{opt}A_d N\tau_{int}} \tag{3.34}$$

where A_d is the area of the detector. Similar forms of Equations 3.30 through 3.34 can be found in [61, 62]. An illustration of a simple sensor pixel can be seen in Figure 3.6. If the noises are assumed to be statistically independent of each other, then the total noise standard deviation for the infrared regime is given by

$$\sigma_{IR} = \sqrt{\sigma^2_{IR_{shot}} + \sigma^2_{IR_{dark}} + \sigma^2_{IR_{johnson}} + \sigma^2_{IR_{GR}}} \tag{3.35}$$

From the formulated IR signal and noise equations, the SNR in the infrared band of interest takes the same form as that of the visible band, which is the ratio of estimated signal to the calculated noise standard deviation, given by

$$SNR_{IR} = \frac{S_{IR_{signal}}}{\sigma_{IR}} \tag{3.36}$$

3.2.3.2 Thermal Detector

The thermal detector operates by detecting the temperature of incident radiation. Radiation illuminates a sensitive material and causes a temperature change, which is detected as a voltage that differs from the detector's bias voltage and then incorporated into the sensor array's electronics. A depiction of a thermal detector can bee seen in Figure 3.8. This detector can operate at temperatures higher than photon detectors, which

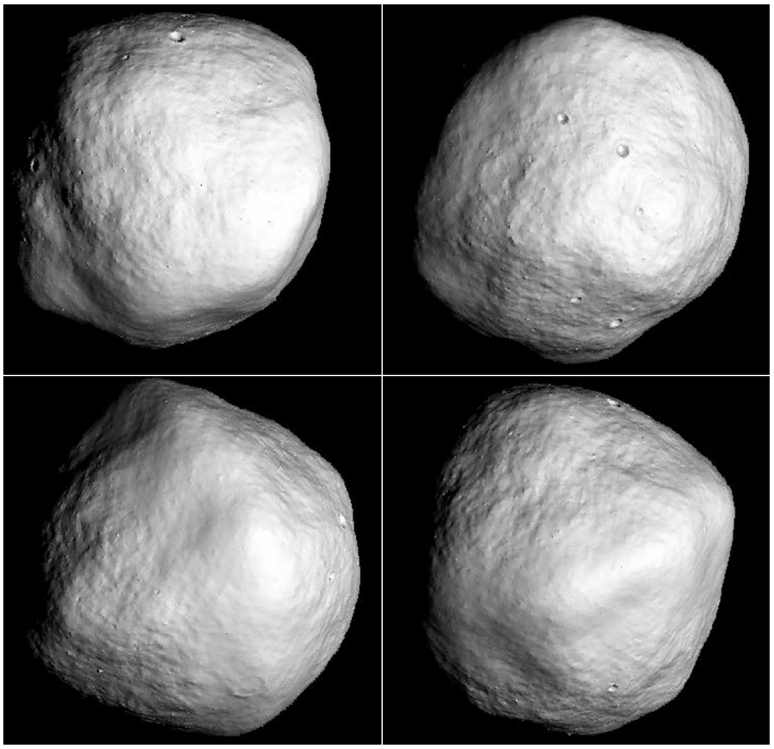

Figure 3.7: Computer generated Bennu polyhedron model with shadowing.

in general, means that there is no device cooling. However, there could be drawbacks when high SNR are desired. Conveniently, the thermal detector uses the same irradiance which was calculated for the photon detector, E_{IR}. By using the irradiance value and the telescope aperture area, the incident power on the pixel array can be determined by

$$P_i = \frac{E_{IR}\tau_{opt}\pi\left(D_o\right)^2}{4n_{pix}} \tag{3.37}$$

where P_i is the incident power per pixel on the sensitive element. This power will be needed when calculating the SNR. Since the incident power is estimated, the noise equivalent power (NEP) for each pixel must be found. The expression for the NEP found in [63] is

$$NEP = \frac{V_n}{R_v} \tag{3.38}$$

where V_n is the noise voltage and R_v(V/W) is the voltage responsivity of the detector. The voltage responsivity is calculated in [60] by

$$R_v = \frac{\alpha_B V_B}{G_{th}\sqrt{1+\omega_{Ch}^2\tau_{th}^2}} \tag{3.39}$$

where α_B is the materials temperature coefficient of resistance (TCR) and is negative for semiconductors, V_B is the device's biased voltage, G_{th}(W/K) is the thermal conductance , ω_{Ch} is the chopper frequency, and τ_{th} is the thermal time constant. Now that the responsivity is found, the only portion of the NEP unknown is the noise voltage.

The noise voltage has three dominating sources for a microbolometer. These three are 1/f noise, Johnson Noise, and temperature fluctuation noise [Cite IR book]. An expression for a normalized 1/f noise is given in [60] and [64] as

$$V_{n_{1/f}}^2 = V_B\frac{n}{f} \tag{3.40}$$

where n is the material dependent factor and f is a frequency. This equation can also be expressed as a non-normalized equality, which incorporates the device integration time and measuring time. The expression in [60] and similarly in [65], which uses bandwidth, gives

$$V_{1/f} = V_B\sqrt{nln\left(\frac{2t_O}{t_i}\right)} \tag{3.41}$$

where t_O is the observation time, which is usually set as the time between shutter actions and t_i is the integration time for the detector process. As it can be seen, the integration time can never be two times longer than the observation time nor the observation time half that of the integration time.

Johnson noise voltage, as given in [60] and [66], is

$$V_J = \sqrt{\frac{2k_B T_d R_d}{t_i}} \tag{3.42}$$

where T_d is the cell's temperature (similar to photon detectors) and R_d is the cell's resistance at the device temperature. The third major contributing noise voltage is from

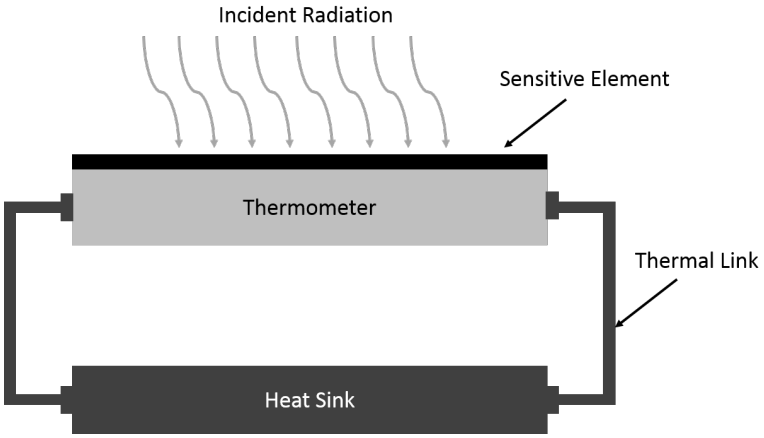

Figure 3.8: Microbolometer detector illustration.

the temperature fluctuation. This expression, after equation substitutions, is given in [60] by

$$V_{TF} = R_v \sqrt{\frac{4\epsilon k_B \sigma T_d^2 A_p + k_B G_{th} T_d^2}{\tau_{th}}} \tag{3.43}$$

where σ is the Stefan-Boltzmann constant ($5.670373\times10^{-8}\mathrm{Wm^{-2}K^{-4}}$) and A_p is the area of a microbolometer pixel. Since the three major contributing noise voltages are estimated, the total noise voltage calculated. These noises are assumed to be statistically independent. Therefore, the total noise voltage is given by

$$V_n = \sqrt{V_{1/f}^2 + V_J^2 + V_{TF}^2} \tag{3.44}$$

All of the components have been found for the NEP. With the NEP, the SNR can be found by dividing the incident power on the pixel by the NEP [67]. It was also shown in [68] that averaging the number of exposures increases the SNR by a factor of the square-root of the number of exposures. The expression is given by

$$SNR_{IR} = \sqrt{N}\frac{P_i}{NEP} \tag{3.45}$$

3.2.4 Image Rendering and Solid-Angle Approximation

The visual camera is simulated by incorporating the albedo of a given target and assigning values to polyhedron shape model faces according to the direction of the sun

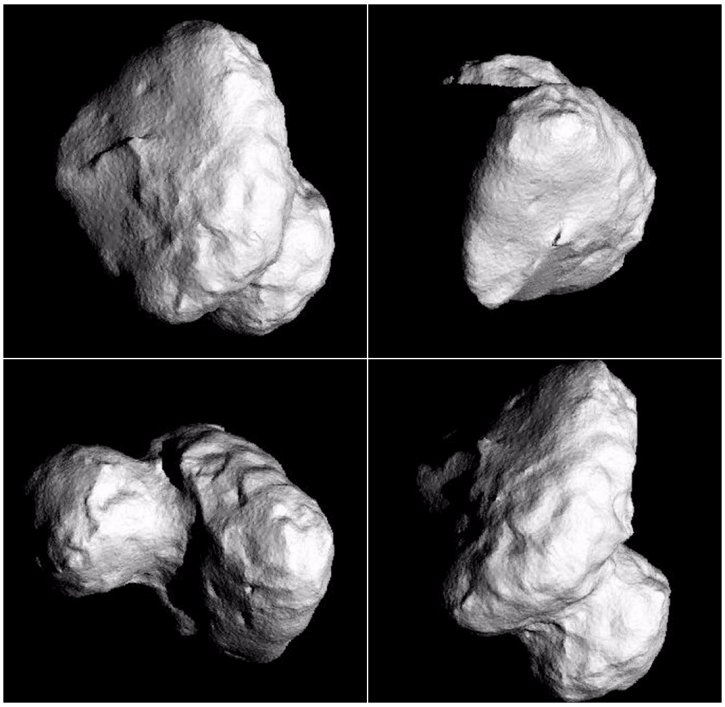

Figure 3.9: Computer-generated 67P/Churyumov-Gerasimenko polyhedron model with shadowing.

vector with the asteroid. This sun vector, $\hat{\boldsymbol{s}}$, is the unit vector pointing from the sun to the target [18], which is found by

$$\hat{\mathbf{s}} = \frac{\mathbf{r}_T}{\|\mathbf{r}_T\|_2} \tag{3.46}$$

Witht this direction to the target define, each polyhedron face coefficient is described as

$$C_i = \begin{cases} k_d\left(\hat{\boldsymbol{n}}_i \cdot -\hat{\boldsymbol{s}}\right) + k_a & \text{if } \left(\hat{\boldsymbol{n}}_i \cdot -\hat{\boldsymbol{s}}\right) > 0 \\ 0 & \text{if } \left(\hat{\boldsymbol{n}}_i \cdot -\hat{\boldsymbol{s}}\right) \leq 0 \end{cases} \tag{3.47}$$

where i is the face index, $\hat{\boldsymbol{n}}_i$ is the outward pointing unit normal vector of each face, k_d is the diffuse lighting coefficient associated with the object's albedo, and k_a is the ambient lighting coefficient. By using this vector, including a ray trace algorithm for shadowing, and exploiting the advantages of parallel computing, realistic images can be generated

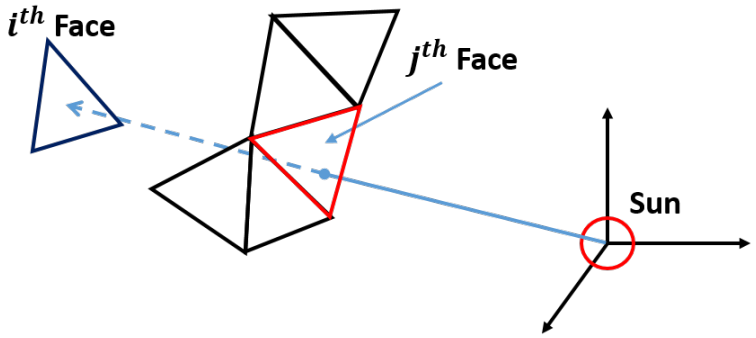

Figure 3.10: Depiction of j^{th} face intersecting a vector to the i^{th} face.

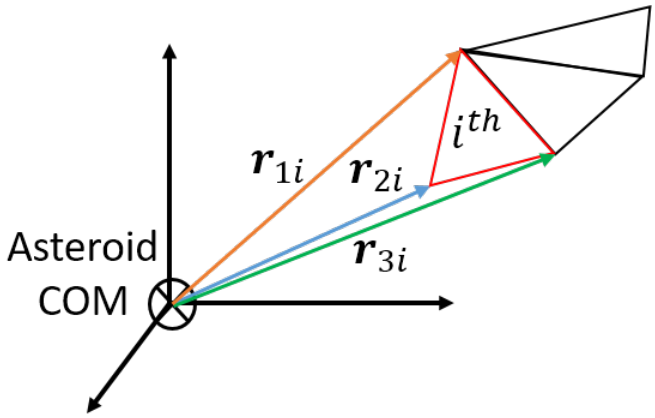

Figure 3.11: The face and vertex vectors of asteroid polyhedron model. Coordinates of each face are relative to the center-of-mass of the object.

quickly. Such images can be seen in Figures 3.7 and 3.9. These images, however, are computed in greyscale.

These computer generated images are depictions of Bennu and Comet 67P/C-G, which are taken at different times within a simulation where the respective body is rotating about a reference axis. As can be seen in these figures, there is crater shadowing. The shadowing is obtained by a GPU-accelerated ray tracing algorithm. By applying this algorithm, the face coefficient for any given face i becomes zero under the following condition: there exists a face j that intersects the vector from the sun to the ith face, where the intersecting jth face is located between the sun and the ith face. An illustration of the face intersection can be seen in Figure 3.10. This shadowing effect will help simulating landing on a target or tracking rendezvous locations.

After the coefficients for the visible faces of the polyhedron are calculated, the solid angle for an extended object can be found. This can be done by projecting the triangular faces visible to the spacecraft onto a plane that is perpendicular to the line-of-sight vector and summing the areas of these projected faces. Figure 3.11 shows the vectors associated with the i^{th} face vertex. The equations for the projected i^{th} face's vertex vectors are given by

$$\mathbf{r}'_{1i} = \mathbf{r}_{1i} - \left(\mathbf{r}_{1i} \cdot \hat{\mathbf{\Lambda}}\right) \hat{\mathbf{\Lambda}} \tag{3.48}$$

$$\mathbf{r}'_{2i} = \mathbf{r}_{2i} - \left(\mathbf{r}_{2i} \cdot \hat{\mathbf{\Lambda}}\right) \hat{\mathbf{\Lambda}} \tag{3.49}$$

$$\mathbf{r}'_{3i} = \mathbf{r}_{3i} - \left(\mathbf{r}_{3i} \cdot \hat{\mathbf{\Lambda}}\right) \hat{\mathbf{\Lambda}} \tag{3.50}$$

where $\mathbf{r}_{1i}$, $\mathbf{r}_{2i}$, and $\mathbf{r}_{3i}$ are the i^{th} face's vertices, $\hat{\mathbf{\Lambda}}$ is the line-of-sight from the spacecraft to the asteroid, and $\mathbf{r}'_{1i}$ through $\mathbf{r}'_{3i}$ are the projected faces. With the projected vertices found, the areas of each triangular face can be calculated. Each i^{th} faces' area is given by

$$S_i = \frac{\left| \left(\mathbf{r}'_{3i} - \mathbf{r}'_{1i}\right) \times \left(\mathbf{r}'_{3i} - \mathbf{r}'_{2i}\right) \right|}{2} \tag{3.51}$$

where S_i is the area of the i^{th} face corresponding to it's projected triangle. The sum of all the visible triangles' area becomes the solid angle as

$$\Omega \approx \frac{\sum_{i=1}^{n} S_i}{\|\mathbf{r}\|_2^2} \tag{3.52}$$

where Ω is the object's solid angle and n is the total number of visible faces. This is done for both the emitted and reflected portions of the irradiance, which would give $\Omega_{emitted}$ and $\Omega_{reflected}$. Note that this approximation only holds when the radius of the object is much smaller than the distance between itself and the spacecraft, $\|\mathbf{r}\|_2$.

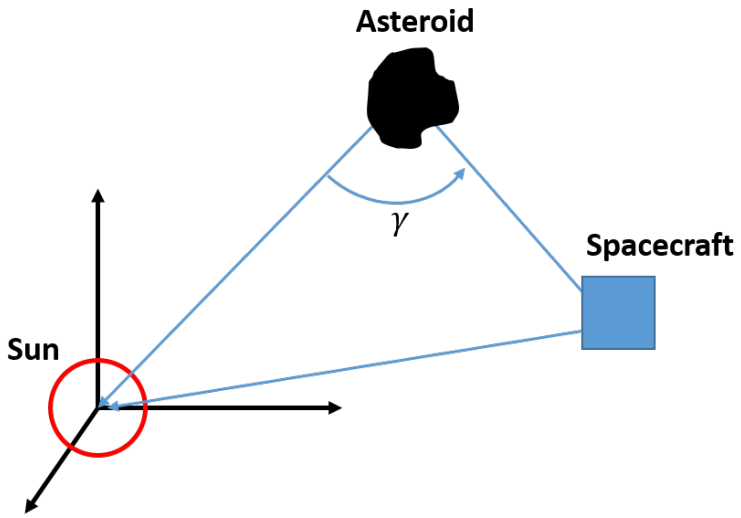

Figure 3.12: Depiction of γ angle, where the axis are of the sun-fixed frame.

Reflected irradiance solid angle is calculated on the GPU by finding the surface area of each triangle that can be seen by both the sun and the spacecraft. These are the intersection faces of both the views. Emitted irradiance solid angle is calculated in a similar manner. However, the triangular areas needed are only from those viewed by the spacecraft. The process for finding the solid angle approximation is done at each time step.

However, when such tools are not available, the solid angle can be estimated using a circular approximation of the object. This can be done by using the angle created by the sun, asteroid, and spacecraft, γ, which can be seen in Figure 3.12, the distance from the spacecraft and the asteroid, as well as the asteroid's radius. The approximation is as follows

$$\Omega \approx \cos\left(\frac{\gamma}{2}\right) \frac{\pi r_{obj}^2}{\|\mathbf{r}\|_2^2} \tag{3.53}$$

where r_{obj} is the radius of the object given in the same units as the distance from the spacecraft to the asteroid, $|\mathbf{x}_R|$. When considering the emitted case, the angle γ, which is then the angle of the source (asteroid) and the receiver (spacecraft), is zero.

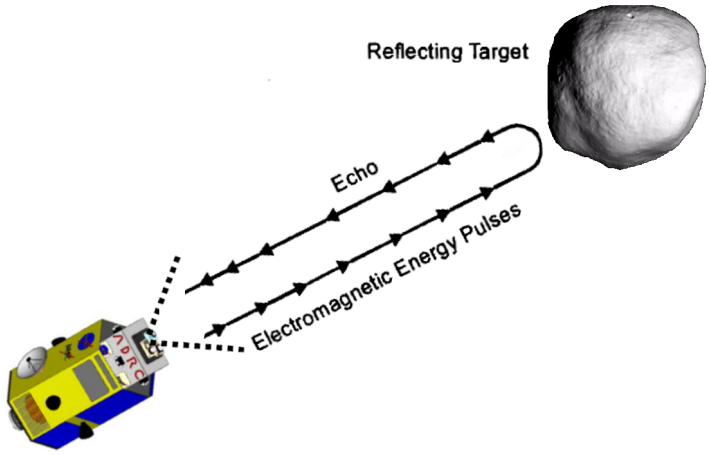

Figure 3.13: Illustration of a monostatic radar system (not to scale).

3.2.5 Radar

Object range determination for a monostatic system (transmitter and receiver are collocated) is found. An illustration of a monostatic system is depicted in Figure 3.13. The radar expression is manipulated to find the maximum detection distance. A minimum detection distance is also required since there is a transition from the near-field to the far-field of the signal. The transition distance from the near-field to the far-field is given in [69]. There is still signal received in the near-field, but may give incorrect values. These two equations are given by

$$R_{max} = \sqrt[4]{\frac{P_t K_{losses} (G_R)^2 \lambda_R^2 \, \sigma_R \, (N_R)^{1/2}}{(4\pi)^3 k_B T_e \, \Delta f \, (SNR_R)}} \tag{3.54}$$

$$R_{min} = \frac{2D_R^2}{\lambda_R} \tag{3.55}$$

where P_t is the peak pulse power transmitted, K_{losses} are the losses of the device, G_R is the antenna gain, λ_R is the radar wavelength, σ_R is the object's radar cross section, N_R is the number of samples, T_e is the equivalent noise temperature, Δf is the bandwidth, (SNR_R) is the desired signal-to-noise ratio, and D_R is the primary signal-collecting dish's

diameter (assuming a circular dish). Variables of other devices should not be confused with radar parameters.

3.3 Sensor Comparison and Simulation Results

3.3.1 Sensor Comparison

Comparison of the sensing devices discussed in the preceding sections is provided herein. This entails the asteroid's detection distance, which corresponds to device's SNR, and image representation given SNR values. These images are plotted using a Matlab program and the calculated standard deviation of the noise.

3.3.1.1 WISE Telescope Comparison

Parameters for the WISE telescope are used to compare with literature and visible band sensors. These parameters for the Si:Ar detector and optics can be found in [57, 70, 71]. By using a detector temperature of 8 Kelvin, integration time of 8.8 seconds, and other parameters of the Si:Ar detector and WISE optics, it was found that a 250 meter diameter object could be detected with a SNR of 5 at approximately 0.5 AU. This confirms what is stated in [72]. However, a few assumptions are made for the asteroid: the asteroid is spherical, has an emissivity of 0.9, which is similar to values in [73, 74], but is lower than values given in [75, 76], and has a β coefficient value of one. Figure 3.14 shows the detection distance compared to a telescope with comparable optics. The visible band sensor has a read noise of 10 e^-/sec/pixel RMS, detector temperature of approximately 230 Kelvin, integration time of 8.8 seconds, and other parameters to that of the IR sensor and optics. It can be seen that the detection distance is linear with the asteroid diameter. This is due to the solid angle approximation using a circumscribing sphere.

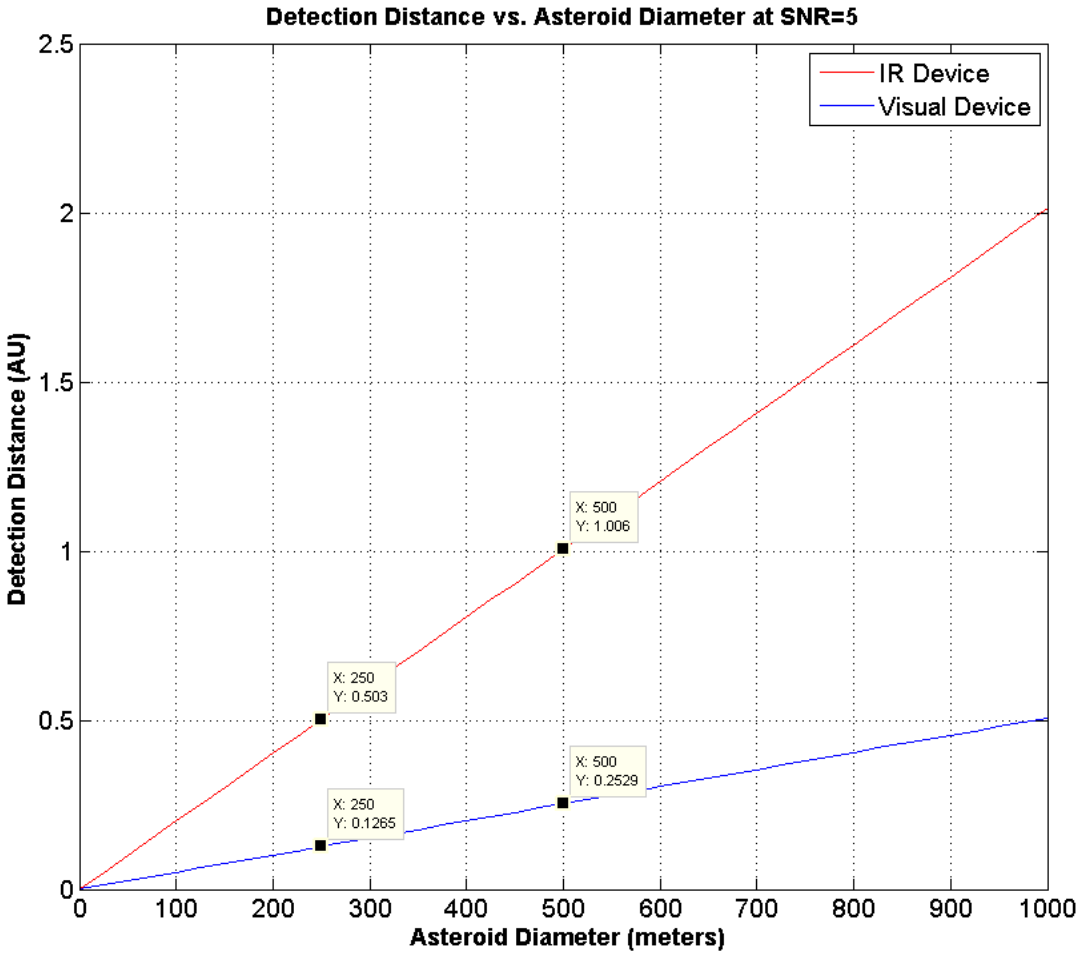

Figure 3.14: Detection distances vs. asteroid diameter of IR and visible band sensors using WISE telescope parameters.

Table 3.1: Visible band sensor design results and asteroid parameters

Instrument Characteristics	Value	Asteroid Parameters	Value
F	1.35 m	T_{ast}	300 K
M	8	r_{ast}	25 m
D_o	0.2 m	$d_{s/obj}$	1.496e8 km
b^*	0.0115 m	$d_{obj/sc}$	$\approx$ 7.75e5 km
η	0.7	α	0.25
G_V	6.83	β	1
τ_{optics}	0.504		
N	1		
τ_{int}	1 sec		
T_d	230 K		
R_r	10 e/pix/sec		
D_v	2.8 DN/e		
κ_1	1.03212649e7 DN/pix/sec		
κ_2	$-$3752.58 K		
n_{pix}	1024$\times$1024 = 1048576 pixels		
Pixel Pitch	18μm		
λ_1, λ_2	380, 800 nm		

3.3.1.2 Infrared and Visible Band Sensor Comparison

Various parameter values of the visible and IR detection devices are kept very similar to those of the NEOWISE telescope, except for a reduction in primary mirror size and operating temperature. By using the formulation for the signal-to-noise ratio and the values given in Tables 3.1 and 3.2, the results for the SNR value of approximately 5 are provided in Tables 3.4 and 3.5. Results illustrate the geometric pixel fill corresponding to the largest dimension of the object, as well as the visual magnitude. These tables show that the geometric pixel fill of the object is less than one, which means there is no object detail resolved but detected. The visual magnitude is calculated from the flux density of the object in both IR and visible wavelengths. In both cases, the reference celestial object is Vega, with an assumed visual magnitude of 0.03 (N band and visual band).

Table 3.2: IR device design results and asteroid parameters

Instrument Characteristics	Value	Asteroid Parameters	Value
F	1.35 m	T_{ast}	300 K
M	8	r_{ast}	25 m
D_o	0.2 m	$d_{s/obj}$	1.496e8 km
b^*	0.0115 m	$d_{obj/sc}$	$\approx$ 7.55e5 km
η	0.7	ϵ	0.9
G_{IR}	6.83	β	1
τ_{optics}	0.504		
N	1		
τ_{int}	1 sec		
T_d	10 K		
κ_1	8.5057355e13 e/pix/sec		
κ_2	$-$225.5617 K		
E_a	0.01943 eV		
R_{sp}	0.5$e-$6 V/e		
ρ_o	7.99742$e-$9 Ω m		
n_{pix}	1024$\times$1024 = 1048576 pixels		
Pixel Pitch	18μm		
λ_1, λ_2	7.5, 16.5μm		

Table 3.3: IR Thermal device design results and asteroid parameters

Instrument Characteristics	Value	Asteroid Parameters	Value
F	4 m	T_{ast}	300 K
M	4	r_{ast}	25 m
D_o	0.8 m	$d_{s/obj}$	1.496e8 km
b^*	0.08m	$d_{obj/sc}$	70.19 km
τ_{th}	1.1$\times 10^{-3}$ s	ϵ	0.9
τ_{opt}	.8		
t_i	1.0 s		
t_o	1.1 s		
N	100		
V_B	0.5 V		
G_{th}	1.02$\times 10^{-7}$ W/K		
n_{pix}	1024$\times$1024 = 1048576 pixels		
R_d	1.577e05Ω		
Pixel Pitch	18μm		
T_d	213.9K		
λ_1, λ_2	7.5, 16.5μm		

Table 3.4: Asteroid detection results for a visible band sensor

Parameters	Value
Geometric Optics Pixel Fill	<1
Visual Magnitude	≈ 12.5
SNR_V	≈ 10.06

Table 3.5: Asteroid detection results for an IR sensor

Parameters	Value
Geometric Optics Pixel Fill	<1
Visual Magnitude (N band)	≈ 4.47
SNR_{IR}	≈ 10.04

Notice, the distance from the object to the spacecraft is almost identical between the visible band and IR sensor. This means that the IR device can detect a 50-meter object, with N band emissivity of 0.9, at about the same distance as the visual device. The detection distances using an IR sensor are not as great as the visible band sensor, which is primarily due to the increase of operation temperature. Moreover, in the visible band, the albedo of the asteroid is set at 0.25, which is a high value for an asteroid. If the phase angle were to be increased, correlating to a smaller β coefficient, the visible band sensor would not out perform the IR sensor for these instrument characteristics. With these parameters, the detection distances and selected asteroid sizes can be seen in Figure 3.15. In these plots, the lines for detection distance are linear due to the assumption of the solid angle being subtended by a circular approximation, along with other approximations using polyhedron face plane projections. The microbolometer thermal device array was not plotted due to the poor performance. Parameters and results for the thermal device can be seen in Table 3.3. It can be seen that this device can detect the asteroid at a distance of approximately 70 km, which is not appropriate for the terminal guidance specifications and will not be considered further in this study. This is primarily due to the resistance increase in the semiconductor with the decrease of operation temperature. When the temperature decreases below 213.9 Kelvin, the SNR begins to increase. A possible solution is to use a different material than non-hydrogenated amorphous silicon.

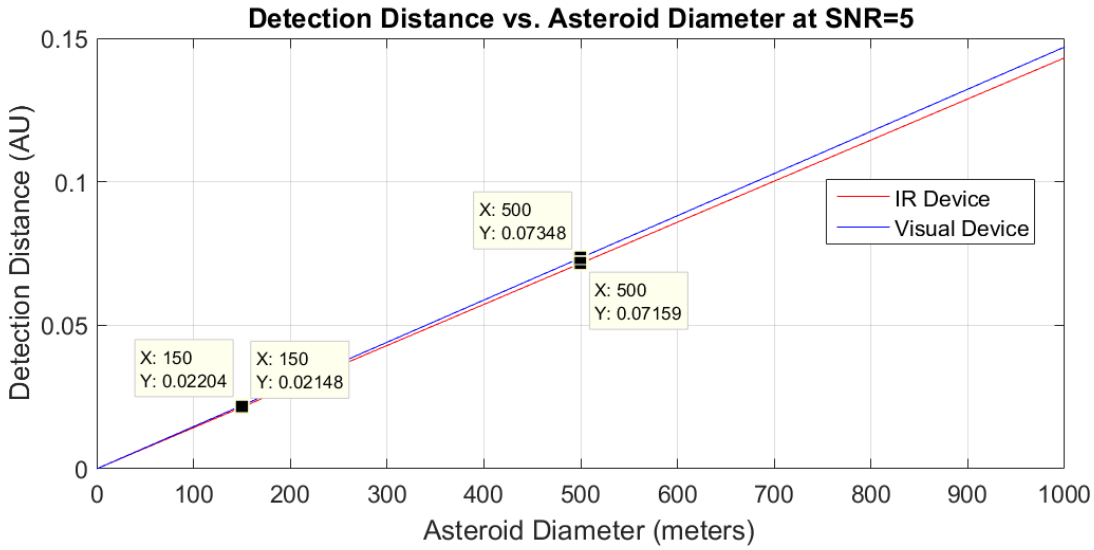

Figure 3.15: Detection distances vs. asteroid diameter of IR and visible band sensors.

Table 3.6: A reference radar design

Instrument Characteristics	Value
P_t	500 W
K_{losses}	0.55
scale	1/10
G_R	8.0568e5
λ_R (scaled)	3.5 mm
σ_R (scaled)	340 m^2
N_R	1000
t_s (Pulse Width)	1μs
T_e	70 K
$\Delta f(1/t_s)$	1.0e6 Hz
(SNR_R)	10
D_R	1 m

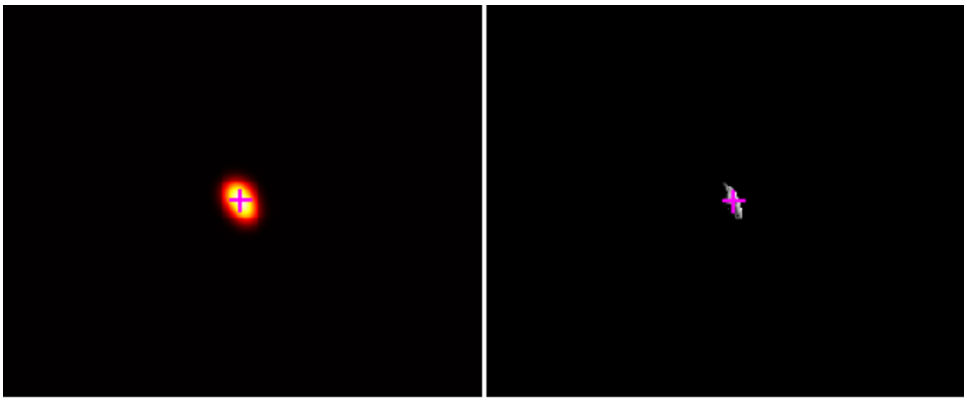

Figure 3.16: Examples of IR and visible band sensor images at 60 seconds prior to final impact.

As stated previously, parameters of the radar device are different from the other two sensing devices. By using the equations describing the radar, an estimation of minimum and maximum detection distances can be found. A scaled Bennu model is used here to evaluate the radar performance. Bennu is scaled by 1/10, resulting in a diameter around 50 meters. When scaling Bennu, the transmitted signal's wavelength must also be scaled by the same factor, if similar detection distances are desired. At a wavelength of 3.5 cm, a unscaled Bennu has a radar cross-section of 3.4×10^4 m^2, which correlates to a scaled σ_r of 340 meters and a wavelength of 3.5 mm. This creates a needed wavelength that is near the edge of the radar regime of the electromagnetic spectrum but is still obtainable.

By using the values in Table 3.6, the radar equations result in a maximum detection distance of 9.062×10^2 km. However, the minimum distance is dictated by the far-field and near-field transition, if there are no filtering techniques applied. This minimum distance before near-field transition measures 571 meters. Rendezvousing with a target body and landing on its surface would need a radar device that has a lower minimum detection range.

Table 3.7: Comparison of IR and visible band sensors during asteroid intercept phase (optical components are the same as in previous comparison)

Simulation Results	IR	Visible
$d_{obj/sc}$ at 2 hours	7.2e4 km	7.2e4 km
Visual Magnitude at 2 hours	-0.654	7.312
Geom. Pixel Fill at 2 hours	< 1	< 1
SNR at 2 hours	1.098e3	1.105e3
$d_{obj/sc}$ at 60 seconds	600 km	600 km
Visual Magnitude at 60 seconds	-11.10	-3.134
Geom. Pixel Fill at 60 seconds	≈ 7	≈ 7
SNR at 60 seconds	1.09e6	4.145e5

3.3.2 Terminal Guidance Simulation Results

Hypervelocity intercept missions are simulated using a scaled 433 Eros polyhedron model. The points of interest are at two hours and 60 seconds before impact. Figure 3.16 compares the visible band and infrared sensors at 60 seconds before asteroid intercept. These simulated images were obtained by using the parameters given in Table 3.1 and Table 3.2, along with Cassegrain telescope design. It can be seen that the asteroid does not fill many pixels on the sensor array. The calculated amount of pixels filled for the maximum dimension of the asteroid can be seen in Table 3.7. This table also includes the SNR for both times of interest. Two hours before impact, each sensor array displays sub-pixel pixel fill. However, at 60 seconds before impact, the horizontal pixel fill is at approximately 37 pixels. In both the sensor scenarios, 2 hours or 60 seconds before impact, the pixel fill does not provide detailed target images.

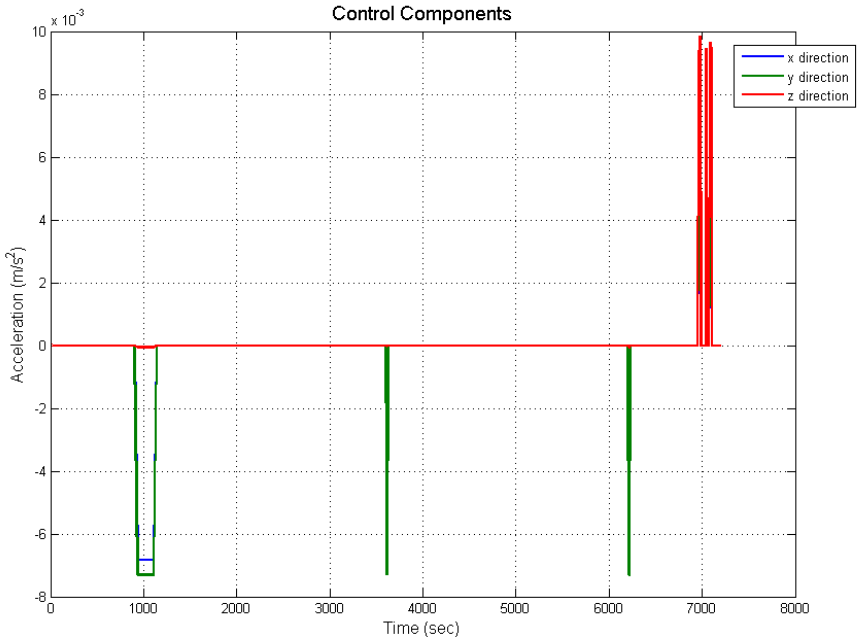

Figure 3.17: Control acceleration time history of an IR-based terminal guidance system (t=0 implies 2 hours before impact).

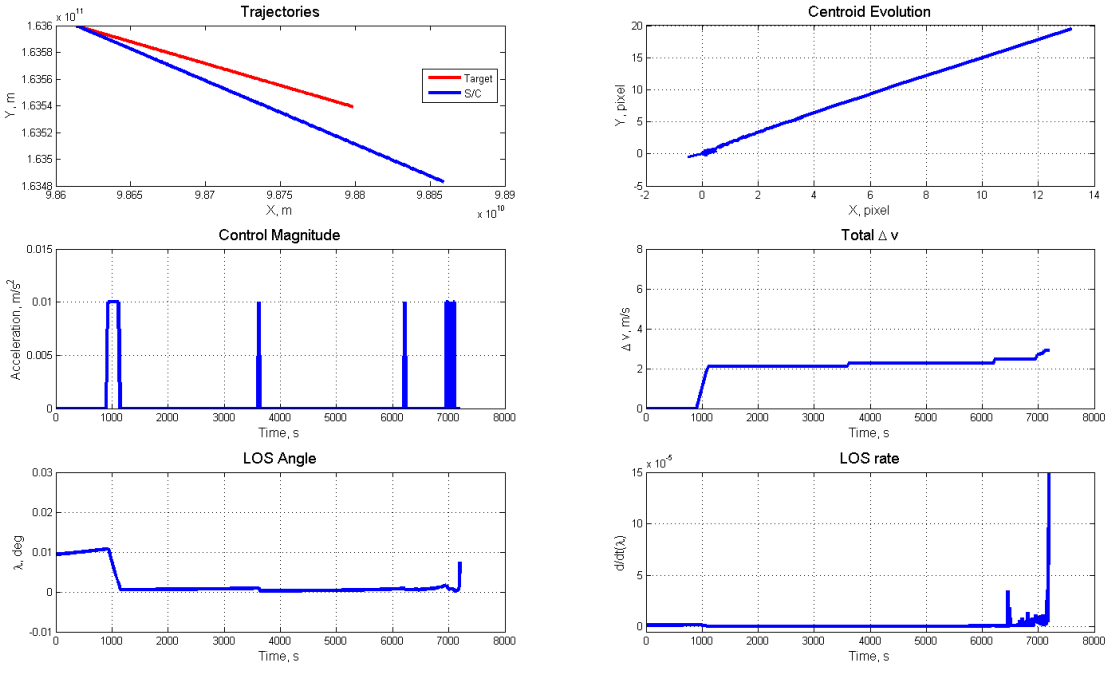

Figure 3.18: Mission specific variables vs. time (or pixel centroid locations) for an IR-based terminal guidance system (t=0 implies 2 hours before impact).

It can be seen that the SNRs at two hours before impact are quite different for both devices. At this point, the IR device can discern the asteroid, whereas the visual device does not have an adequate SNR. This shows for lower albedo asteroids, which are small and have higher emissivity, that the IR device may out-perform the visual device. Consequently, the guidance algorithms use the information from the IR device and radar. Radar is used once the distance from the asteroid to the spacecraft is sufficient for radar detection, which was stated to be about 900 km.

For the guidance simulations, a hybrid algorithm is used. This includes kinematic intercept guidance, which uses predetermined control pulses and proportional navigation. During the beginning of the terminal phase of the mission, the spacecraft undergoes kinematic impulse guidance, and once a sufficient amount of pixels is filled on the sensor array by the target, the guidance algorithm is switched to proportional navigation guidance to ensure mission success. A depiction of the control accelerations can be seen in Figure 3.17. Spacecraft Δv requirements and other mission specifications can be seen in Figure 3.18. For this scenario, the velocity requirement is small, because this is done during the terminal phase of the mission. These requirements assume that the major trajectory maneuvers have been completed prior to the terminal phase. The resulting intercept speed is approximately 10 kilometers per second.

Using this same control acceleration, at 60 seconds before impact, the spacecraft will separate into a fore and aft body system[77]. At this separation time, a position and velocity error are placed on the fore and aft bodies. This simulation is conducted 3,000 times. After these simulations, approximately 98.5 percent of the fore bodies and 98.7 percent of the aft bodies impact in the IR case. In comparison, only 93.4 percent impacted of both fore and aft bodies for the visible case. A depiction of these simulations are shown in Figure 3.19. This figure, green dots represent the fore body, while red dots represent the aft body. In this scenario, the impact percentage utilizing an IR sensor barely out performed the visual camera case. This is due to the sun-asteroid-spacecraft

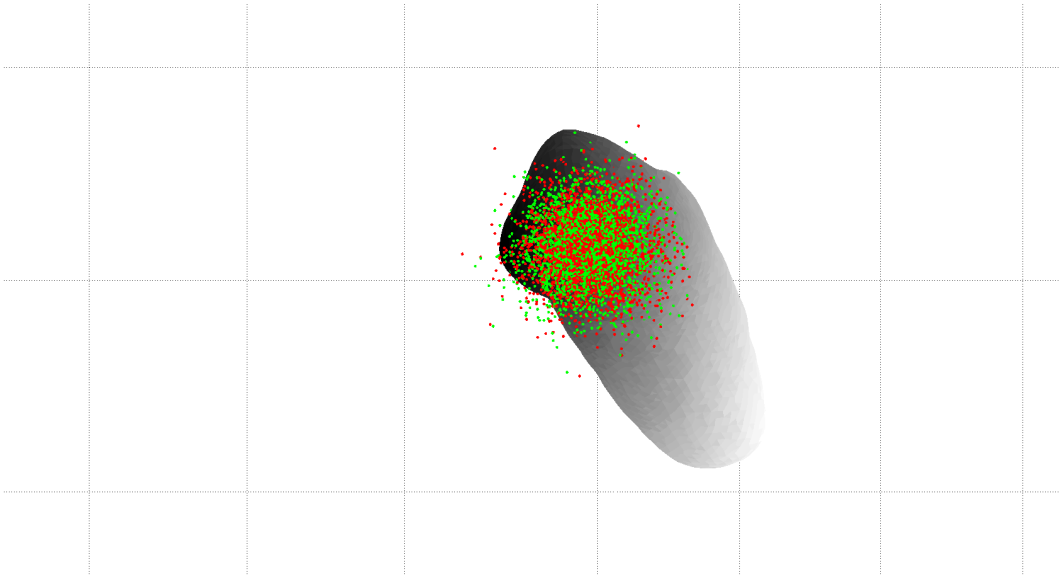

Figure 3.19: Monte Carlo simulation result for intercepting a 50-meter asteroid using an IR-based terminal guidance system.

phase angle. If the β coefficient were to be closer to zero, larger phase angle, less light would be illuminating the surface of the asteroid in the spacecraft's line-of-sight, which would cause a lower percentage of successful impacts.

3.4 Conclusion

In this chapter, the signal-to-noise ratio estimation and detection distance estimation for IR and visible band sensing devices have been examined for asteroid intercept/rendezvous applications. In addition, estimation of the solid angle of an object due to shadowing was studied, which relates to object irradiance. By following the procedures described within this chapter, maximum detection distances were found for all three sensing devices. These distances, corresponding to a 50-meter asteroid, were estimated to be 7.75×10^5 km for the the visual device, 7.55×10^5 km for the IR device, and 906.2 km for the radar. These results show that for an asteroid with an IR emissivity of 0.9 and a visible albedo of 0.25, the IR sensing device detects the asteroid at a distance approximately the same as the visible band sensing device. To evaluate the performance

of a terminal guidance system equipped with such sensors, Monte Carlo simulations were performed, which resulted in approximately 98.5% impact success using an IR device and only 93.4% for a visual device. Further research must consider more accurate solid angle approximations, as well as device functionality in close asteroid proximity situations and asteroid polyhedron gravitation.

CHAPTER 4. TERMINAL GUIDANCE SYSTEM MODELING AND SIMULATION FOR A MULTIPLE KINETIC-ENERGY IMPACTOR VEHICLE (MKIV)

4.1 Introduction

NASA's Deep Impact mission to intercept a 5-km comet by a kinetic-energy impactor has been successfully accomplished in 2005. Its terminal guidance system used visual cameras and preplanned trajectory maneuvers to intercept Comet 9P/Tempel (Comet Tempel 1). An observer spacecraft performed a flyby of the comet while the impactor spacecraft collided with the comet at 10.2 km/s [40].

On a smaller scale, systems have been designed to intercept ballistic missiles, along with any decoy objects. Missile defense organizations and companies have been developing several innovative solutions to intercepting ballistic missiles in the presence of interceptor decoys [78, 79]. One such example is the Multiple Kill Vehicles (MKVs) designed by Lockheed Martin and Raytheon Company. A MKV system architecture by Lockheed Martin uses a Carrier Vehicle (CV) containing smaller Kill Vehicles (KVs) to intercept ballistic missiles [80, 81]. Several KVs detach from the CV, obtain orientation information, and position information of themselves as well as the CV. While target acquisition impact locations are determined on-board the CV for the KVs, each KV remains in contact with the CV. Commands calculated by the CV will be distributed to the KVs, which incorporate the decoys or target positions. Each KV has "minimal functionality," which includes sensors and actuators. A mono-camera system suffers due to

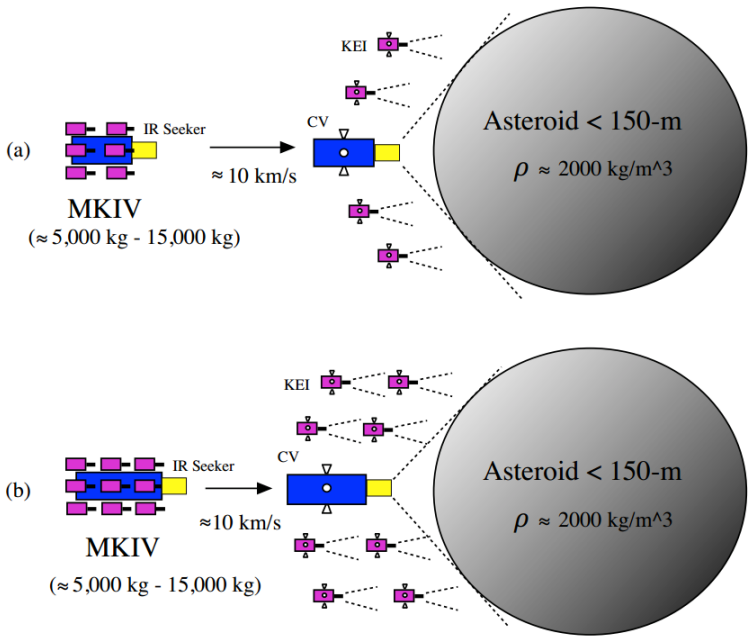

Figure 4.1: Illustration of the MKIV concept [14].

the potential of important targets leaving the view of the CV. However, another MKV architecture by Raytheon incorporates a targeting system on each KV, including the CV. All vehicles communicate amongst each other to identify and intercept the ballistic missile, in addition to decoys.

In [14], a Multiple Kinetic-energy Impactor Vehicle (MKIV) concept was proposed for effective disruption or pulverization of small asteroids without using nuclear explosive devices (NEDs). Similar to the MKV system architectures briefly described above, we can consider two types of the MKIV concept. Either concept could be used for a single target or multiple targets. The single target case would have multiple KEIs intercepting a single asteroid target. For the concept and visualization, refer to Figure 4.1. Preliminary MKIV impact simulation study results based on a GPU-accelerated hydrodynamics code are presented in [13, 82].

This chapter will focus on image processing algorithms for such coordinated terminal guidance and control of multiple KEIs. GPU-based simulation results of the proposed image processing algorithm will be discussed to verify the feasibility of impacting a small

asteroid by multiple KEIs. Simulation results using noiseless as well as noisy visible band and IR images will be presented for scaled polyhedron models of 433 Eros and 216 Kleopatra. These images are needed to estimate the line-of-sight (LOS) for each KEI to its respective impact location. The preliminary results presented within this chapter will support that it is technically feasible to impact a small asteroid near-simultaneously at its multiple locations using the proposed MKIV system architecture.

4.2 Noiseless Image Processing and Line-of-Sight Determination

The noiseless situation arises in the most ideal image array cases. This scenario considers the best case and test bed for calculating line-of-sight (LOS) to the target or targets along with the needed digital image processing. Two cases are considered when impacting a single asteroid: single KEI or a MKIV with only the CV equipped with an asteroid targeting device.

4.2.1 Single Kinetic-Energy Impactor

A single KEI case occurs when only one impactor is sent to intercept and fragment the target. In the noiseless image case, the target may appear as seen in Figure 4.2. This is a depiction of a scaled 433 Eros, but other scaled models will be used to show the robustness of the multi-impact algorithm. There is no noise associated with the pixels on the image array. Pixel illumination occurs only when signal from the target is present. The center of figure (COF), infrared sensor, or center of bright (COB), visible band sensor, may be determined from this image. By using pixel values on the sensor array, the COF and COB are determined as

$$O_{x_{COB}} = \frac{\sum_{i=1}^{n} \sum_{j=1}^{m} \mathrm{G}(i,j)\ j}{n\ m} \qquad \text{if } \mathrm{G}(i,j) \geq \xi_{COB} \tag{4.1}$$

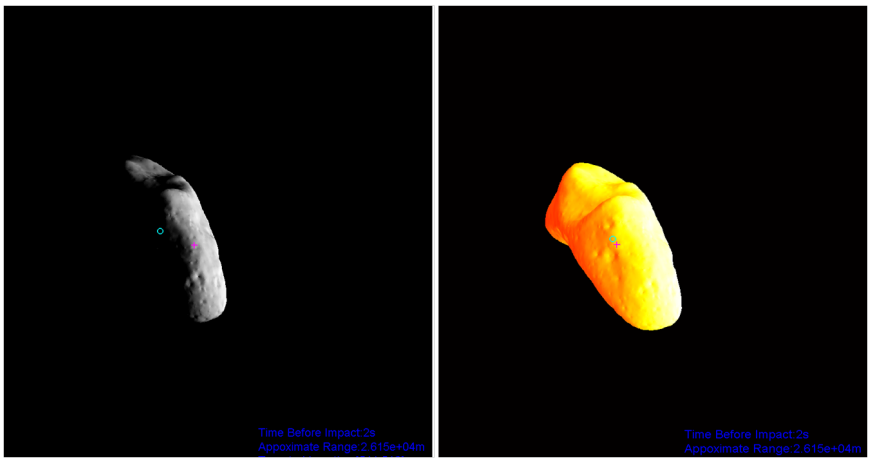

Figure 4.2: Noiseless visible band (left) and IR (right) images of 433 Eros used for terminal guidance simulation.

$$O_{y_{COB}} = \frac{\sum_{i=1}^{n} \sum_{j=1}^{m} \mathrm{G}(i,j)\ i}{n\ m} \qquad \text{if } \mathrm{G}(i,j) \geq \xi_{COB} \tag{4.2}$$

$$O_{x_{COF}} = \frac{\sum_{i=1}^{n} \sum_{j=1}^{m} j}{n\ m} \qquad \text{if } \mathrm{G}(i,j) \geq \xi_{COF} \tag{4.3}$$

$$O_{y_{COF}} = \frac{\sum_{i=1}^{n} \sum_{j=1}^{m} i}{n\ m} \qquad \text{if } \mathrm{G}(i,j) \geq \xi_{COF} \tag{4.4}$$

where O_x and O_y are the IR or visible band image's horizontal and vertical centroid pixel location, n is the horizontal number of pixels, m is the vertical number of pixels, i is the horizontal pixel location, j is vertical pixel location, $\mathrm{G}(i,j)$ is value of image at horizontal and vertical pixel coordinate, and ξ_{COB} and ξ_{COF} are image pixel minimum inclusion limits. These limits are significant when calculating COB and COF for an image with the inclusion of noise. Recall that the basic structure and camera formulations are discussed in Chapter 2. For simplicity, in later sections the subscripts of COB and COF are dropped due to the estimation of multiple impact locations.

4.2.2 Multiple Kinetic-Energy Impactors

The MKIV architecture explores the use of a single spacecraft platform which detaches multiple KEIs. Each KEI communicates with the main spacecraft, called the CV. Due to communication, the CV is the only spacecraft that is required to carry an asteroid targeting sensor device. Doing so will cause multiple KEIs to impact over the asteroid's surface and cause distributed damage. An illustration of the intercept concept can be seen in Figure 4.1. These varying locations of impact are difficult to determine when the shape of the target is not well known. However, these locations can be found by implementing digital image processing.

4.2.3 KEI Impact-Location Determination

When an image of a target body is obtained, the target-body image is split into chunks according to the size of the asteroid, the orientation, and the number of KEIs impacting the target. The COB or COF locations found in Section 2.1 are used to separate the image into either an upper and lower image (horizontal split) or a left and right image (vertical split). By dividing the image, half of the impactors impact one side where as the other half impact the opposite side. To determine whether the image is split horizontally or vertically, the following criterion must be met

$$\frac{y_{max}-O_y}{x_{max}-x_{min}} \geq \frac{1}{2} \quad \text{(horizontal split)} \tag{4.5}$$

where y_{max} is maximum vertical pixel that the asteroid fills in the upper half of the image, and x_{min} and x_{max} are the minimum and maximum horizontal pixels that are filled by the asteroid. If this criterion is not met, the image is split vertically.

Once the image has been split, the number of impact channels can be determined, along with the half-image asteroid pixel fill number. Impact channels limit the number

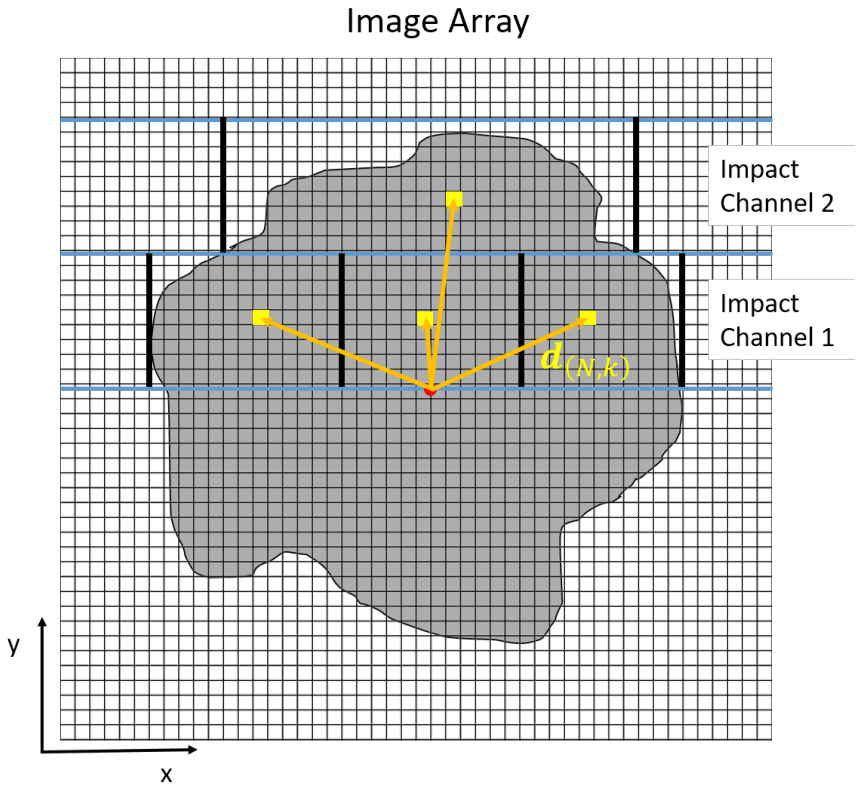

Figure 4.3: Upper image analysis for a 9-impact situation (1 CV and 8 KEIs). Red square indicates the COF and CV impact location, blue horizontal lines indicate the impact channel boundaries, black vertical lines are the chunk centroid boundaries, yellow rectangles are KEI impact locations, and orange arrows indicate the image plane targeting vectors. Image is not proportionate to actual situation.

of rows on the asteroid's image that the impactors will be allowed to impact in. The maximum number of channels can be calculated as

$$N_{Channel} = \frac{N_{cr}-1}{2} - \text{FLOOR}\left(\frac{N_{cr}-1}{4}\right) \tag{4.6}$$

where $N_{Channel}$ is the number of impact channels and N_{cr} is the number of impactor spacecrafts. This equation only holds when there are an odd number of impactors, which includes the main body impactor impacting at the center of figure of the target. For a general purpose, Equation 4.6 can be used for the total number of impact channels. The number of impactors in each channel can be calculated as

$$N_{k_{craft}} = \text{NINT}\left(\frac{A_{k_{Channel}}(N_{cr}-1)}{2\ A_{half}}\right) \tag{4.7}$$

where $N_{k_{craft}}$ is the number of impactors in the k$^{\text{th}}$ channel, $A_{k_{Channel}}$ is the asteroid pixel area of the k$^{\text{th}}$ channel, and A_{half} is the pixel area of the asteroid on half the image.

Once the number impactors are determined for each channel, the impact location can be calculated. Dividing the k$^{\text{th}}$ channel area by the number of k$^{\text{th}}$ channel impacting spacecrafts results in an impact area estimation. This area is the criterion for placing an impact location. The algorithm determines the asteroid's image filled pixels in each channel. After the pixel area reaches the divided channel's area, an impact location is placed in the centroid of the channel sector. The centroid estimation for the channel sector and the upper half of the image is then processed as

$$O_x(k,N) = \frac{\sum_{j=x_{sN}}^{x_{eN}} \sum_{i=O_y+(k-1)\frac{y_{max}}{N_{Channel}}}^{O_y+k\frac{y_{max}}{N_{Channel}}} j}{(x_{eN}-x_{sN})\left(\frac{y_{max}}{N_{Channel}}\right)} \quad \text{if} \quad \text{G}(i,j) \geq \xi \tag{4.8}$$

$$O_y(k,N) = \frac{\sum_{j=x_{sN}}^{x_{eN}} \sum_{i=O_y+(k-1)\frac{y_{max}}{N_{Channel}}}^{O_y+k\frac{y_{max}}{N_{Channel}}} i}{(x_{eN}-x_{sN})\left(\frac{y_{max}}{N_{Channel}}\right)} \quad \text{if} \quad \text{G}(i,j) \geq \xi \tag{4.9}$$

$$\mathbf{d}_{k,N} = \begin{bmatrix} \left(O_x(k,N) - \frac{m}{2}\right) h_{pix} \\ \left(O_y(k,N) - \frac{n}{2}\right) v_{pix} \\ 0 \end{bmatrix} \tag{4.10}$$

where k is the channel number, N is the KEI number within the channel, x_{sN} is the starting x-value pixel for the N$^{\text{th}}$ spacecraft impact location in the k$^{\text{th}}$ channel, x_{eN} is the ending x-value pixel for the N$^{\text{th}}$ spacecraft impact location in the k$^{\text{th}}$ channel, h_{pix} is estimated horizontal pixel resolution in meters, v_{pix} is estimated vertical pixel resolution in meter, m is the vertical number of sensor pixels, n is the horizontal number of pixels, and $\mathbf{d}_{k,N}$ is the deviation vector for each impactor intercept location in the camera frame. The starting location of the (N+1)$^{\text{th}}$ spacecraft, in general, is the ending x-value for the N$^{\text{th}}$ spacecraft. Note, this is the formulation for only the upper half of the image. A similar process can be done for the bottom of the image and when the image is separated into right and left instead of upper and lower halves. A depiction of the impact channels, channel subdivision, and centroid corresponding to an upper and lower half split can be seen in Figure 4.3.

Once an impact location is calculated for all impactors, the locations need to be related to the corresponding LOS. This is simply done by taking the coordinates of the centroids and transforming them into the inertial reference frame. The estimated LOS pointing vector for each spacecraft is then

$$\hat{\mathbf{\Lambda}} = \frac{\mathbf{r}_T - \mathbf{r}_{sc_{k,N}} + C^{I/A}\mathbf{d}_{k,N}}{\left|\left|\mathbf{r}_T - \mathbf{r}_{sc_{k,N}} + C^{I/A}\mathbf{d}_{k,N}\right|\right|} \tag{4.11}$$

where $\mathbf{r}_T$ is the target's estimated location in the inertial frame, $\mathbf{r}_{sc_{k,N}}$ is the inertial location of the N$^{\text{th}}$ impactor spacecraft in the k$^{\text{th}}$ channel, and $C^{I/A}$ is the transformation matrix from the camera frame, A, to the inertial frame, I.

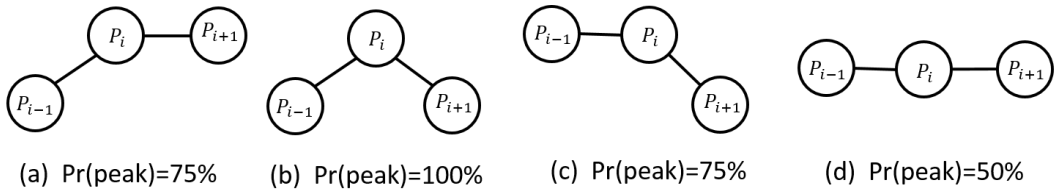

Figure 4.4: Probabilities of each binned histogram location point, P_i. All other combinations not listed result in a 0% peak probability.

4.3 Image Processing and LOS Determination With Noise

Gaussian random noise, with zero mean, is added to the noiseless image, G, using a conversion of a random uniform distribution to random normal distribution by Box-Muller transform [83]. The standard deviation of the noise is determined from the amount of electrons excited by the target and device parameters. Such parameters and processes can be found in [84]. Once the full image is simulated, the actual object on the image plane must be detected and other image noise eliminated. Once the objects are detected, the targeting of the asteroid is the same as the noiseless system.

4.3.1 Object Detection and Elimination of Noise

The noisy image, W, is first subjected to a median filter, converted into greyscale, and converted into a binary image. Otsu's method is used to determine an initial thresholding limit, P_o. The values of the greyscale image (GSI) range from 0 to 255, and the values for the normalized greyscale image (NGSI) range from 0 to 1. Otsu's method is described in detail in [85]. However, in most cases, Otsu's method finds a lower thresholding limit than what is desired when trying to eliminate noise. A solution is to use Otsu's method threshold value, which is normalized by 256, to help find a higher threshold. By binning the GSI information into a 32 bin collection, peaks may be found. Figure 4.4 depicts how to decide if the histogram value is a peak, which is similar to [86], where histogram valleys are found. If the peak falls into the probability being greater or equal to 75

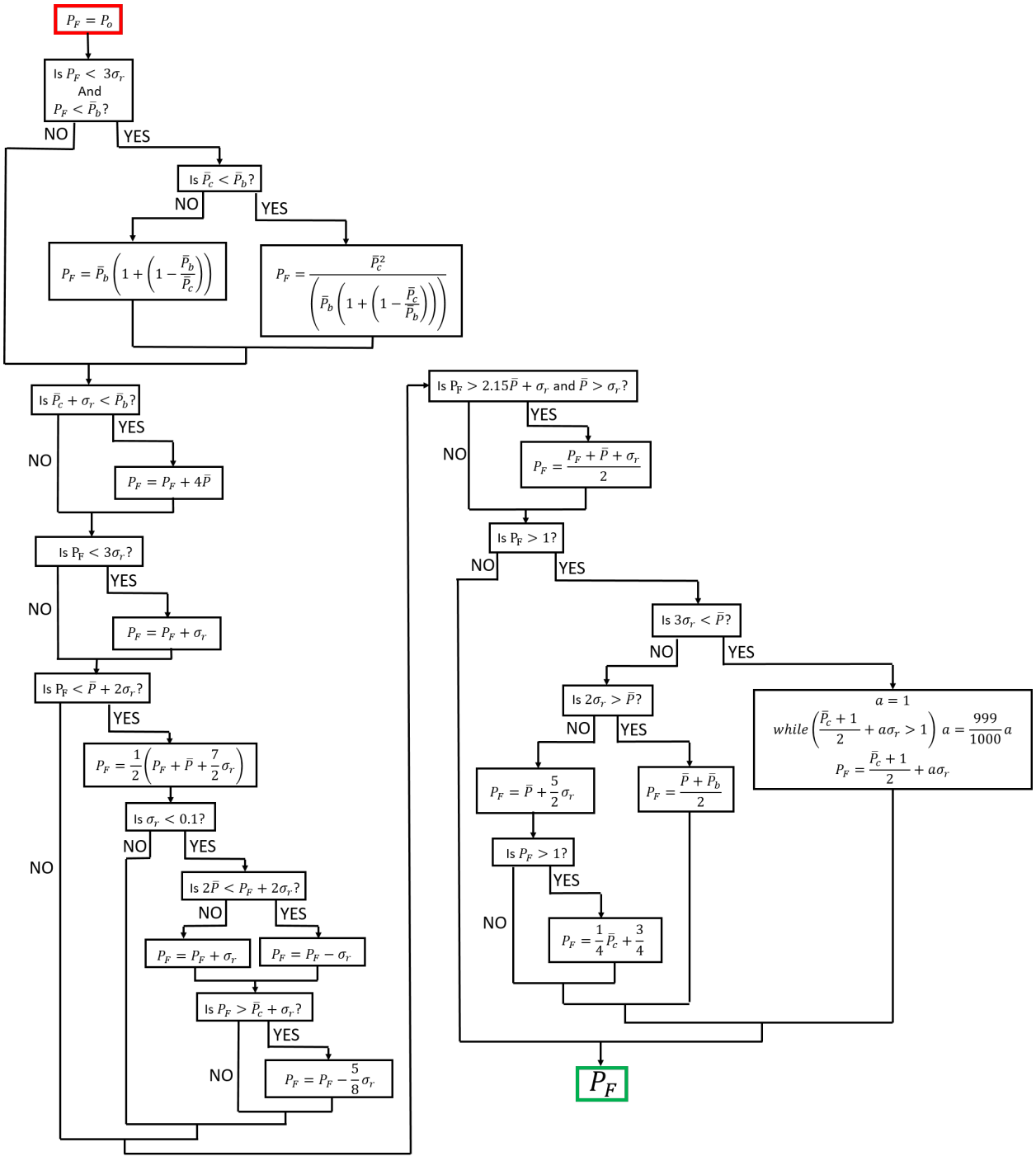

Figure 4.5: Thresholding logic for calculating the final binary threshold, P_F.

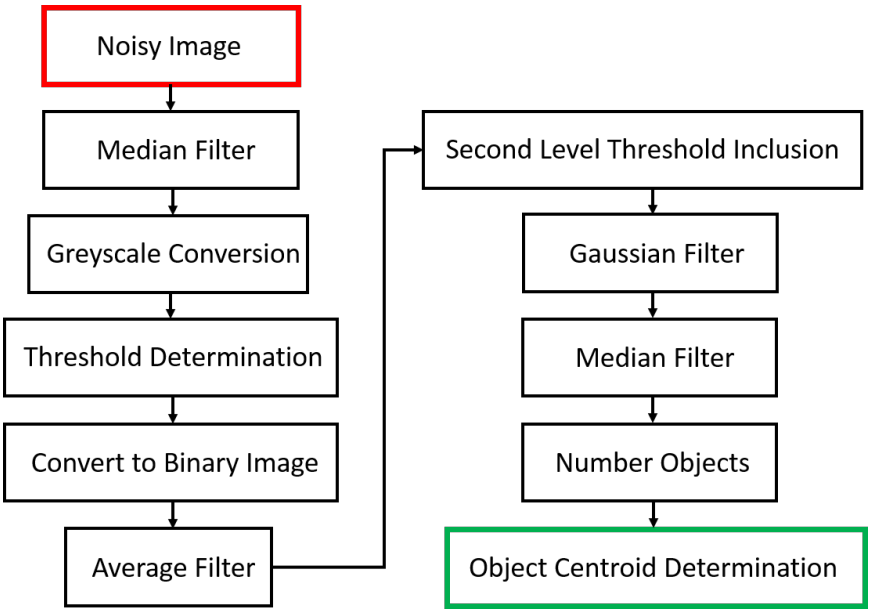

Figure 4.6: Noise cancellation, object determination, and object centroid scheme flow chart.

percent, this location within the binned histogram is considered a peak. Once each peak is determined, a value of interest is found as

$$\bar{P}_b = \frac{1}{32\ \bar{n}} \sum_{i=1}^{\bar{n}} P_b(i) \tag{4.12}$$

where P_b is the value at which a peak occurs in the binned histogram, $\bar{n}$ is the number of peaks, and $\bar{P}_b$ is the average of the peak locations. This value ranges from 0 to 1, hence the division by the binned size value. If, however, $\bar{n} = 0$, $\bar{P}_b$ can be estimated using a variable which will be discussed later.

The overall average of the NGSI is computed as

$$\bar{P} = \frac{1}{m\ n} \sum_{j=1}^{n} \sum_{i=1}^{m} \mathrm{W}_n(i,j) \tag{4.13}$$

where $\bar{P}$ is the average value of the image array, and W_n is the filtered NGSI. By using $\bar{P}$, an upper threshold estimate can be obtained as

$$\bar{P}_c = \frac{\bar{P}+1}{2} \tag{4.14}$$

where $\bar{P}_c$ can be used to estimate a peak location value, $\bar{P}_b$, when $\bar{n} = 0$. The peak value can be found as

$$\bar{P}_b = \frac{\bar{P}_c}{2} \tag{4.15}$$

Another value needed, is the average row standard deviation of the NGSI, σ_r. This should not be confused with the total standard deviation of the NGSI. The average row standard deviation is found by

$$\sigma_r = \frac{1}{n}\sum_{i=1}^{n}\sqrt{\frac{1}{m}\sum_{j=1}^{m}\left(\mathrm{W}_n(i,j)-\bar{P}\right)^2} \tag{4.16}$$

As it may be noticed, when calculating the row standard deviation, the biased formulation is used instead of implementing the Bessel correction, $n-1$. Using P_o and the variables from Equations 4.12 to 4.16, a threshold, P_F can be determined for locating image objects of interest. Figure 4.5 shows the logic for determining a final threshold. A second level threshold is calculated for use within the algorithm. This is found by

$$P_2 = \frac{P_o+P_F}{2} \tag{4.17}$$

By using filtering logic and steps depicted in the flow chart of Figure 4.6, the noise elimination, object detection, and centroid locations can be found. An illustration of object detection and centroid using Otsu's method as well as the thresholding described here can be found in Figures 4.7 and 4.8. In these images, zero mean random Gaussian noise, with differing standard deviations is implemented. The brighter objects in the scene are objects of interest, since this is mostly likely to be the situation in space. As it can be seen in Figure 4.7, Otsu's Method fails to have a threshold which properly separates the bright objects from the rest of the image. The thresholding algorithm

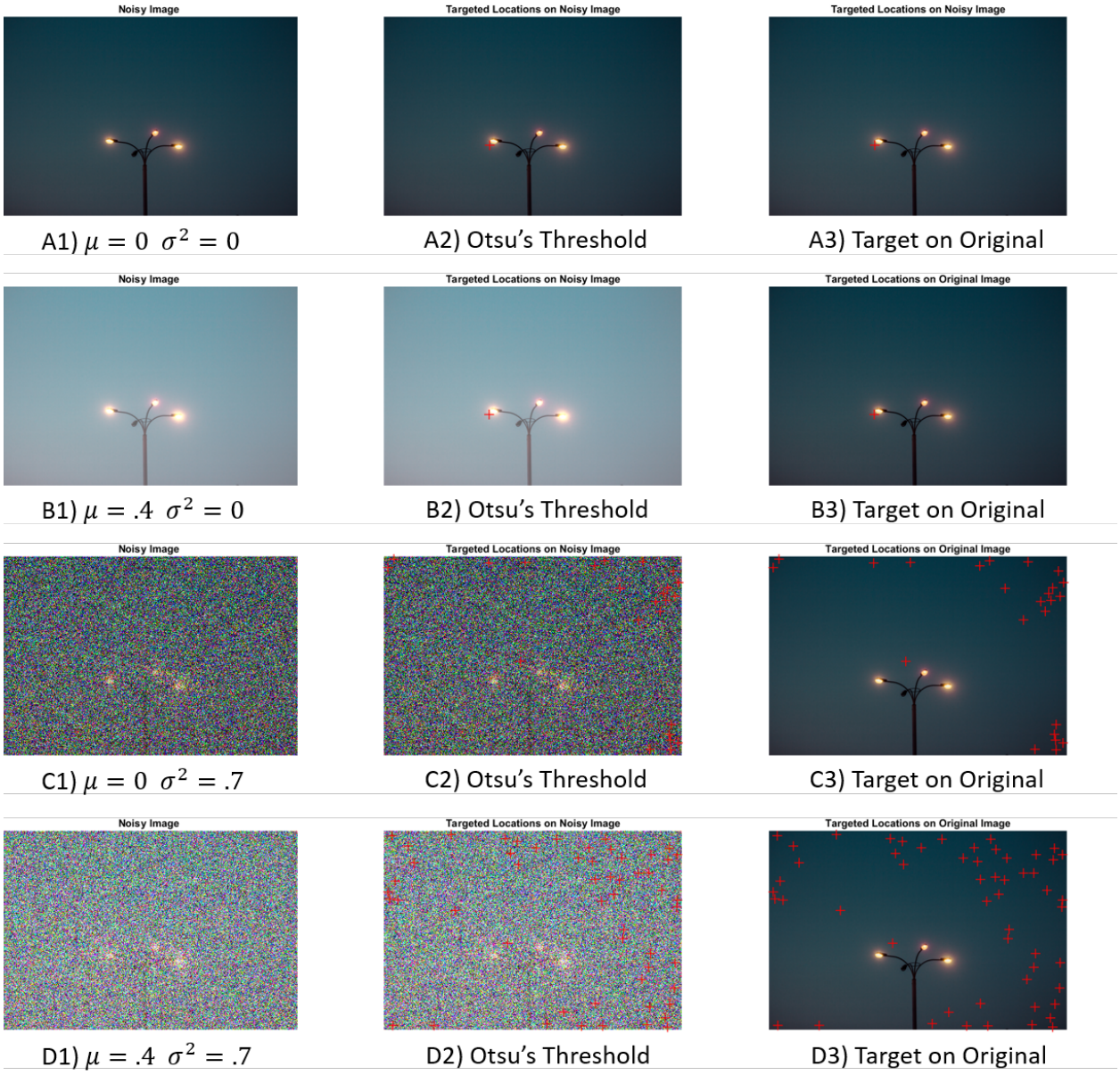

Figure 4.7: Otsu's method of threshold being used for various degrees of random Gaussian noise. Left image specifies noise addition, middle is detected objects centroids in the noisy image, right depicts targeted locations on original image. Noise was added using the "imnoise" function of Matlab. Original image courtesy of Angelina Litvin on https://stocksnap.io/photo/U4JKNI8126.

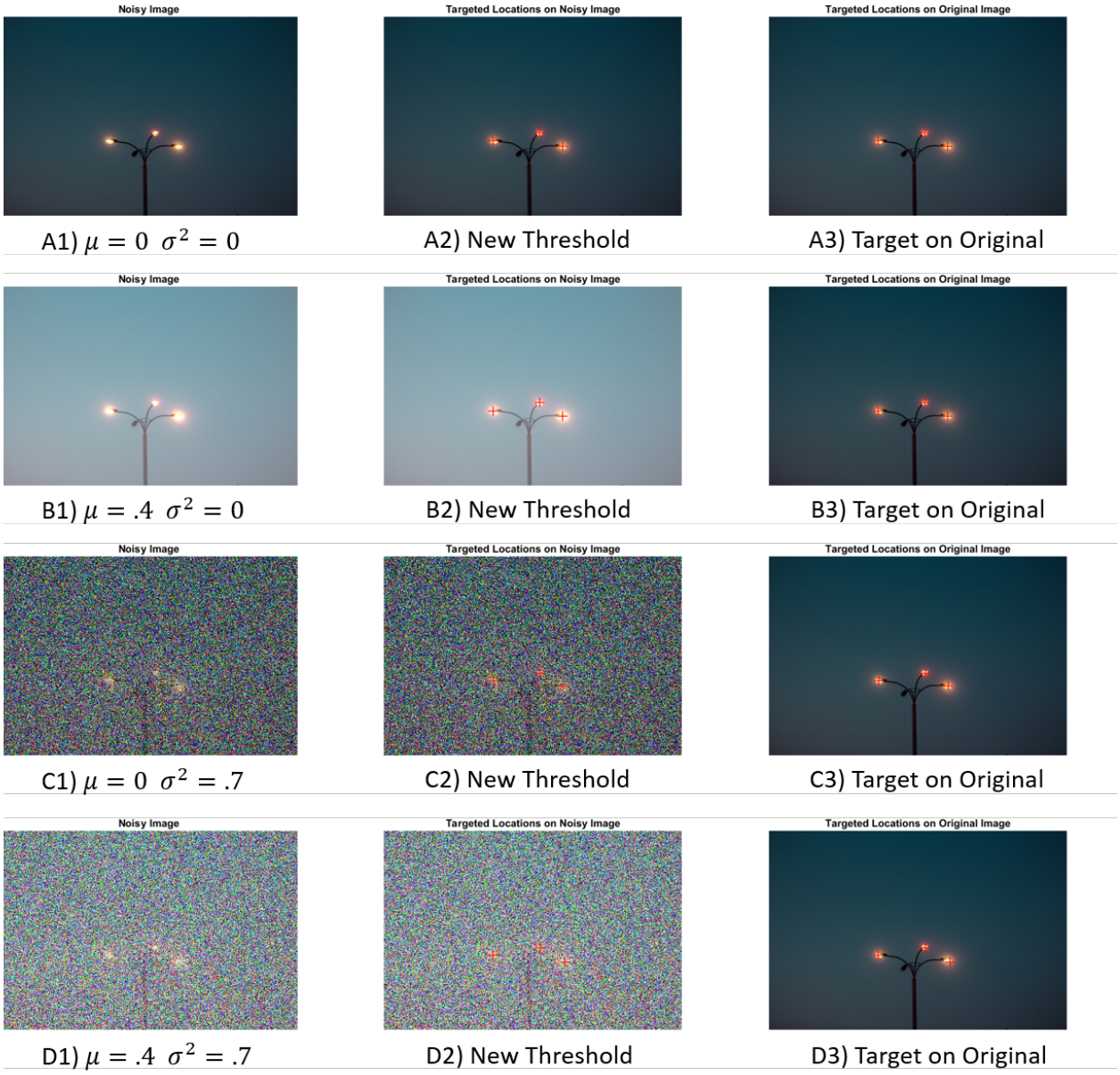

Figure 4.8: Otsu's method of threshold being used for various degrees of random Gaussian noise. Left image specifies noise addition, middle is detected objects centroids in the noisy image, right depicts targeted locations on original image. Noise was added using the "imnoise" function of Matlab. Original image courtesy of Angelina Litvin on https://stocksnap.io/photo/U4JKNI8126.

presented here is not guaranteed to detect all bright objects, but may also include random areas of higher valued pixel clusters. A pixel area comparison would be needed to establish if the object detected is a product of the noise or the actual object of interest. The case shown in Figure 4.8 does however, detect the three bright lights of interest. In addition, implementation of the Local Area Signal-to-Noise Ratio (LASNR) algorithm given in [87] could help to further confirm exact objects of interest and object segmentation. However, the LASNR has not demonstrated its full capabilities when the image is diluted by substantial quantities of noise.

4.4 Simulations and Results

Simulations were ran using the same scenario as presented in [34], except for incorporating multiple impactors. Both infrared sensor cases and visible band sensor cases are presented. During the simulations, it was found that taking pure camera data resulted in control acceleration jitter. Jitter was due to the impact locations differing for each sample, which at greater distances from the asteroid, affects the amount of change the LOS vector undergoes. To remedy this situation, a five sample averaging filter was implemented on the calculated impact locations. The calculated LOS no longer had the sharp changes due to the changing of pixels once this filter was incorporated. However, this does cause a delay when large changes are present. An example of the commanded control acceleration components for an unfiltered sequence of images can be seen in Figure 4.9, which is in reference to one of the kinetic-energy impactors.

4.4.1 Noiseless Image for MKIV

The MKIV concept, using a noiseless image, implements a five impactor system. This consists of four KEI's and the CV, which contains the target sensing device and will be used as the main/fifth impactor. All of the four kinetic-energy impactors target locations

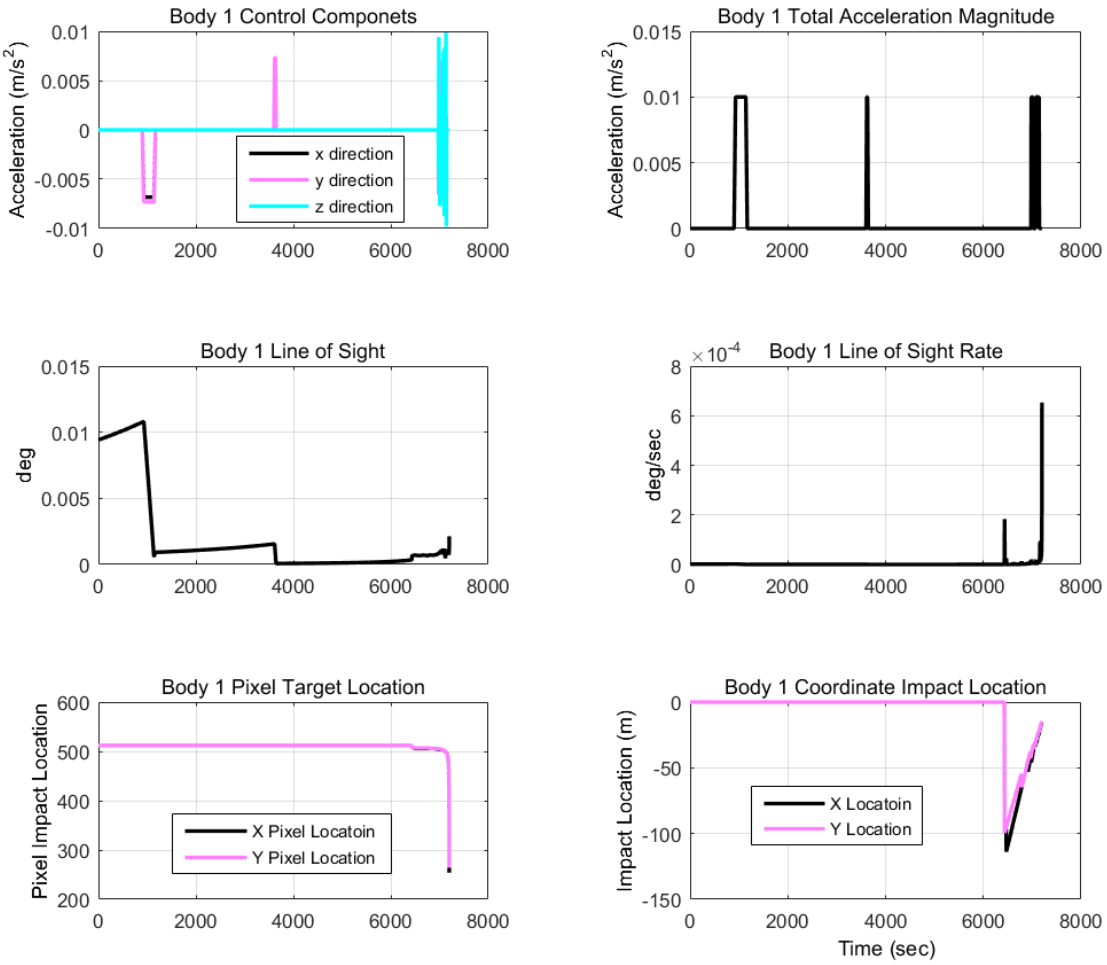

Figure 4.9: Control accelerations and mission variables with regards to one of the KEI's using unfiltered camera information.

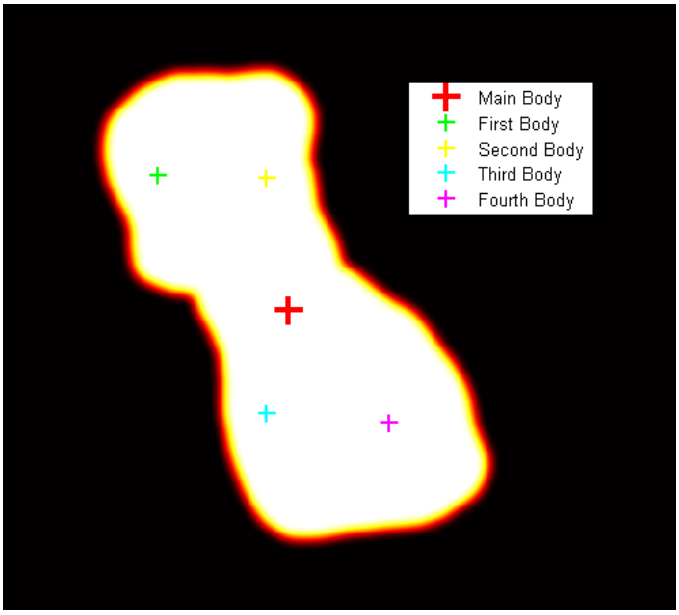

Figure 4.10: Predicted impact locations using an infrared sensing device.

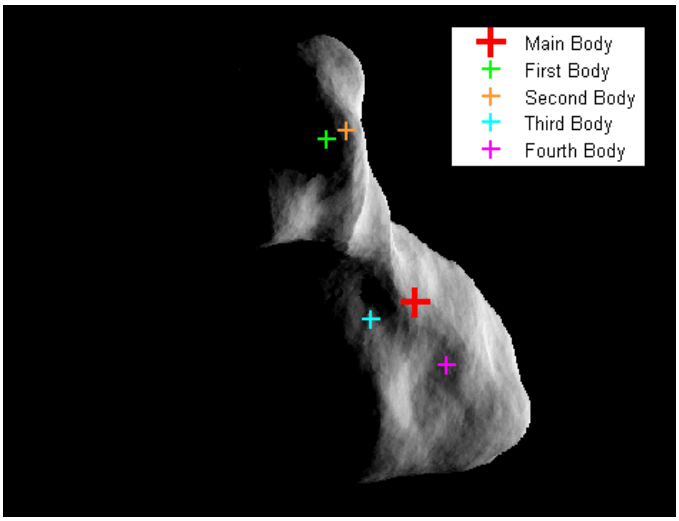

Figure 4.11: Predicted impact locations using a visible band sensing device.

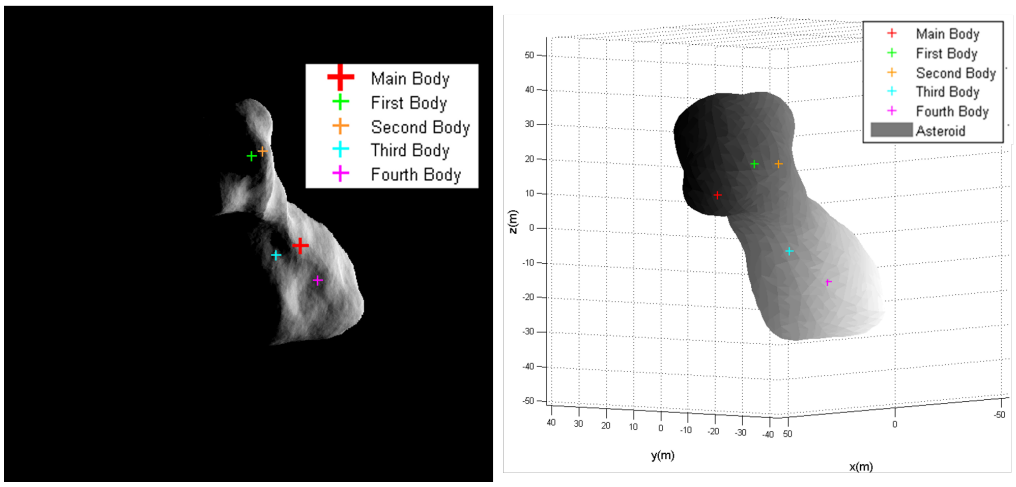

Figure 4.12: Predicted impact locations (left) and actual impact locations (right) using a visible band sensing device.

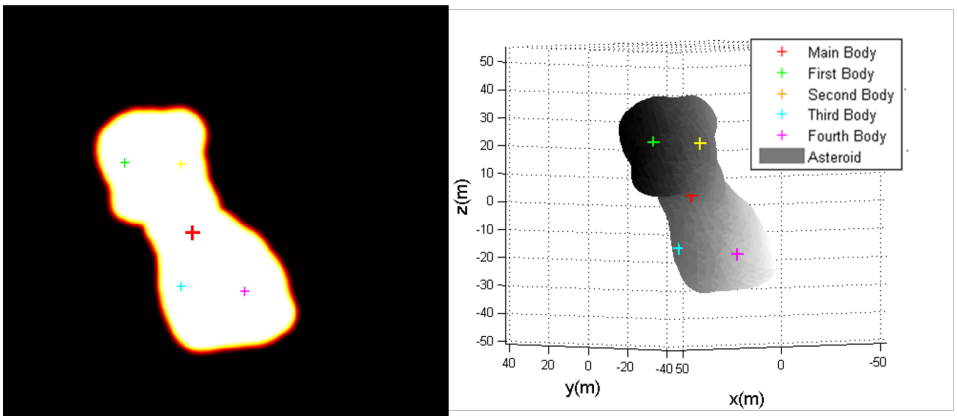

Figure 4.13: Predicted impact locations (left) and actual impact locations (right) using an infrared sensing device.

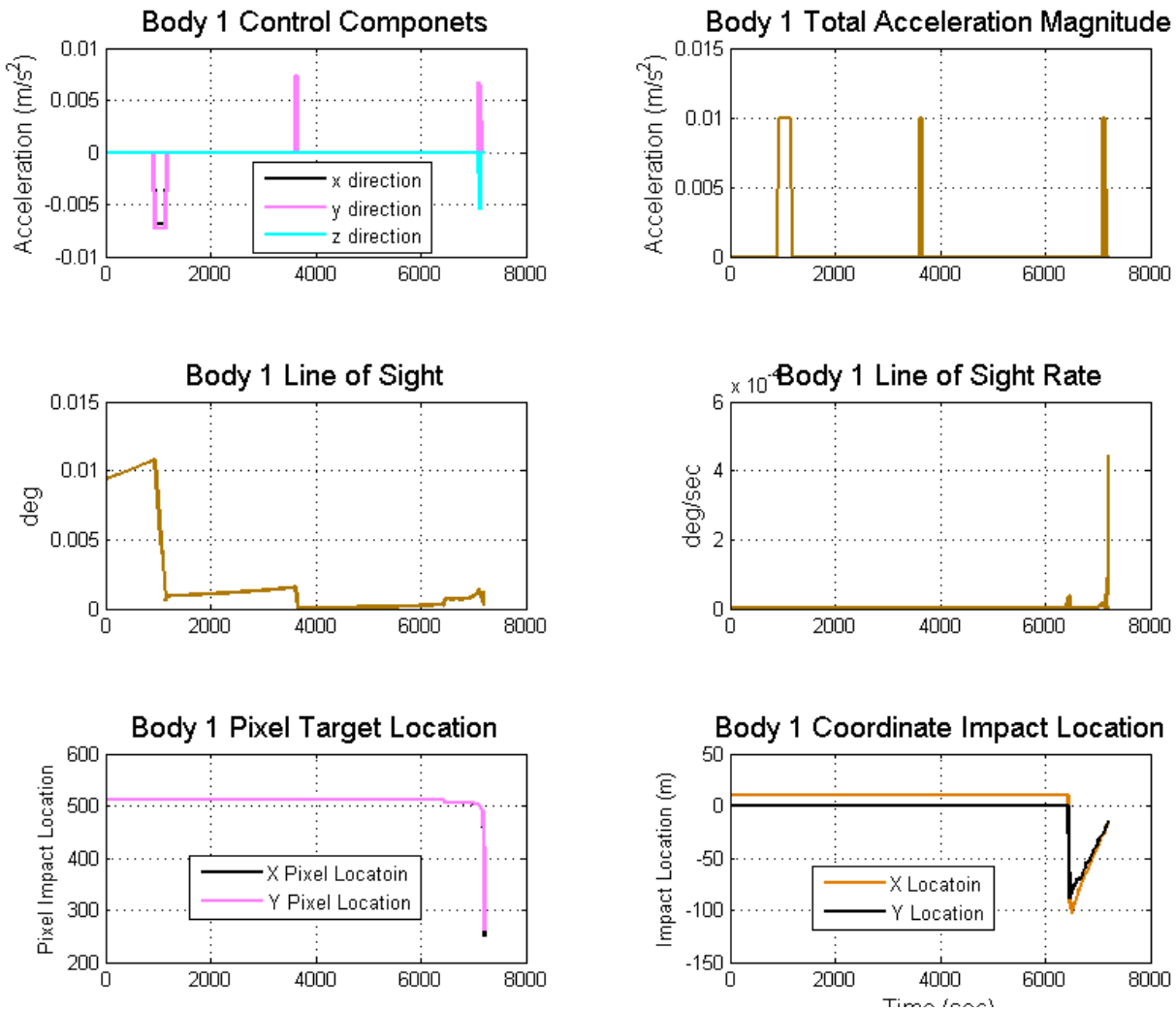

Figure 4.14: Control accelerations and mission variables of the KEI using filtered camera information.

Figure 4.15: Simulated infrared image at approximately 2 hours from impact with a signal-to-noise ratio of approximately 22.

are distributed on the body. In addition, the CV spacecraft targets the COF or COB. Figure 4.10 and Figure 4.11 show the predicted impact locations on a scaled model (100 m) of 216 Kleopatra corresponding to a simulated infrared image and a simulated visual image.

As it can be seen in Figures 4.10 and 4.11, the impact locations on the infrared image are distributed over the entire target body, while the impact locations on the visual image are limited by the illumination of the asteroid's surface. Actual impact locations and a comparison with the targeted locations can be seen in Figure 4.12 and Figure 4.13. As the figures show, the impact locations on the body failed to impact precisely where targeted. This is due to the thrusters no longer being active when the KEIs are 60 seconds before impact. By doing so, it causes a targeting jitter while maintaining marginal accuracy in impact location.

All KEIs perform terminal guidance thrusting maneuvers. For ease, solely the first KEI will be shown. This is due to a comparison with the first body of the unfiltered case. An illustration of the mission components can be seen in Figure 4.14. As shown in this figure, the KEI does not have an uncontrollable amount of system jitter. This

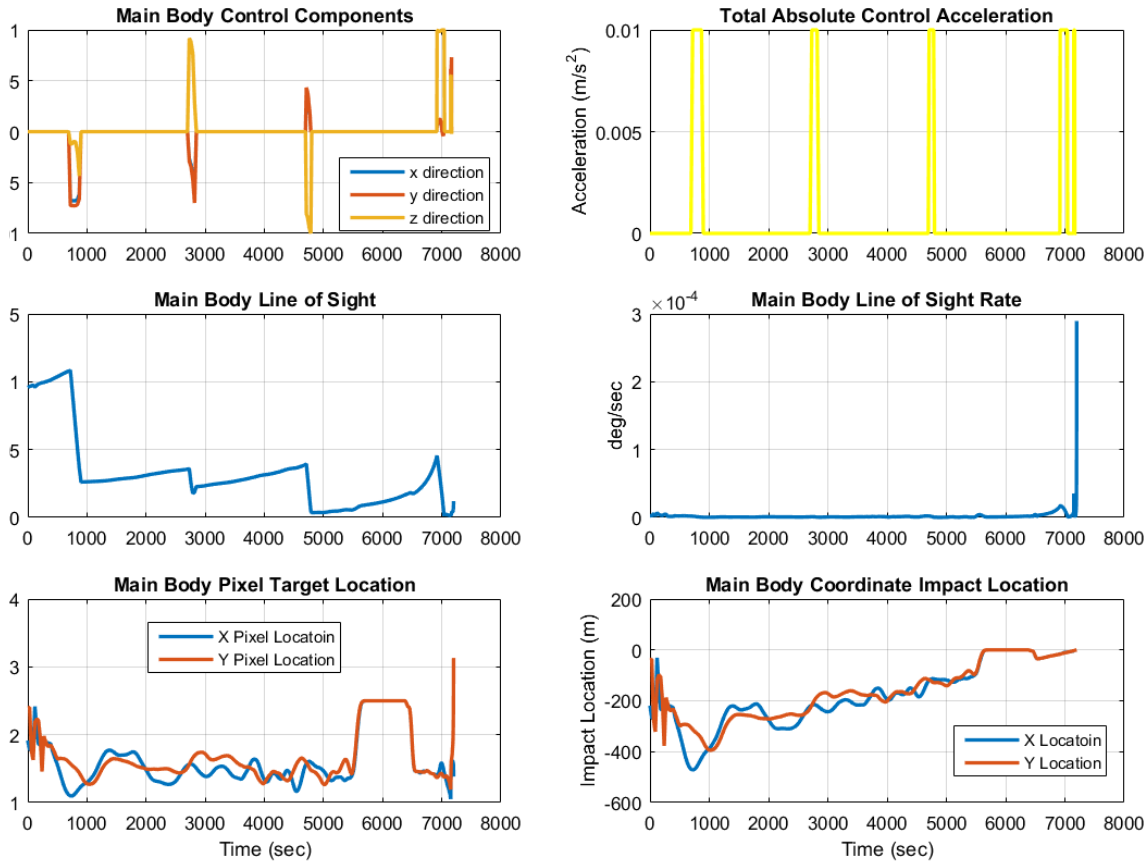

Figure 4.16: CV control accelerations and mission variables using filtered camera information.

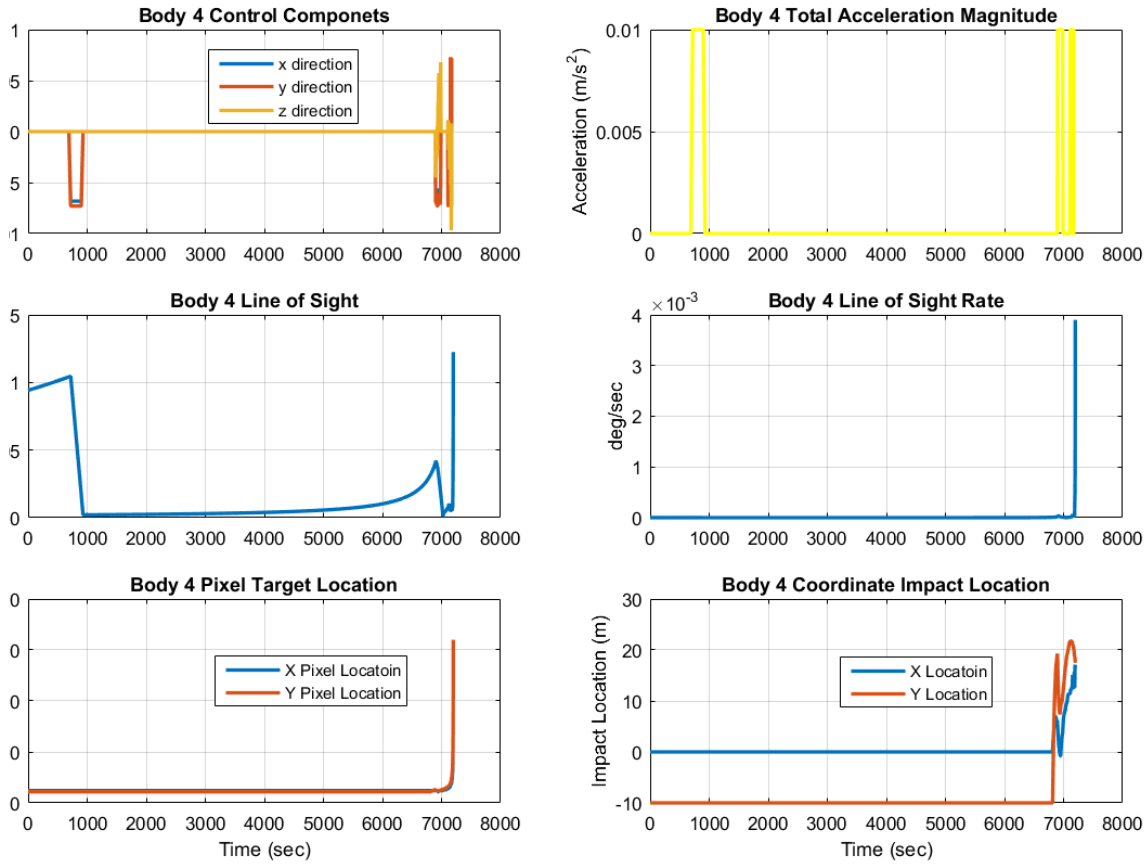

Figure 4.17: KEI-4 control accelerations and mission variables using filtered camera information.

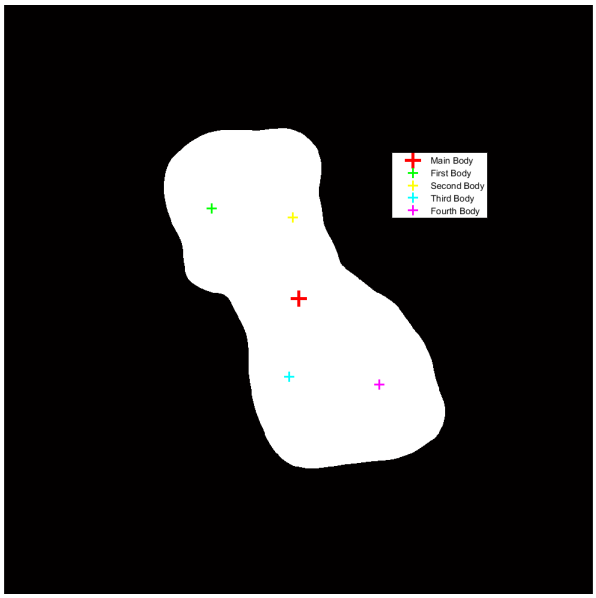

Figure 4.18: Object blob detection and targeted impact locations.

can be compared with the identical KEI using unfiltered camera information, which is depicted in Figure 4.9.

4.4.2 Noisy Image for MKIV

A similar mission scenario is conducted, where the KEI has thruster firings until 30 seconds before the final impact, using a simulated infrared camera with the addition of camera noise. A simulated image at 2 hours before asteroid intercept can be seen in Figure 4.15. At this point, the asteroid on the image array has a signal-to-noise ratio of approximately 22. Digital image processing schemes are used to eliminate the noise caused by the asteroid and detector. Object blob detection and noise elimination is completed by the threshold method described in Section 4.3.1 following the flow in Figures 4.5 and 4.6.

Due to this threshold technique, the impact locations may vary slightly. The actual target location, commanded accelerations, and other mission points of interest are shown in Figure 4.16. It can be seen that the information for the impact location is not constant, but has undergone an averaging filter. Using an averaging filter results in the guidance

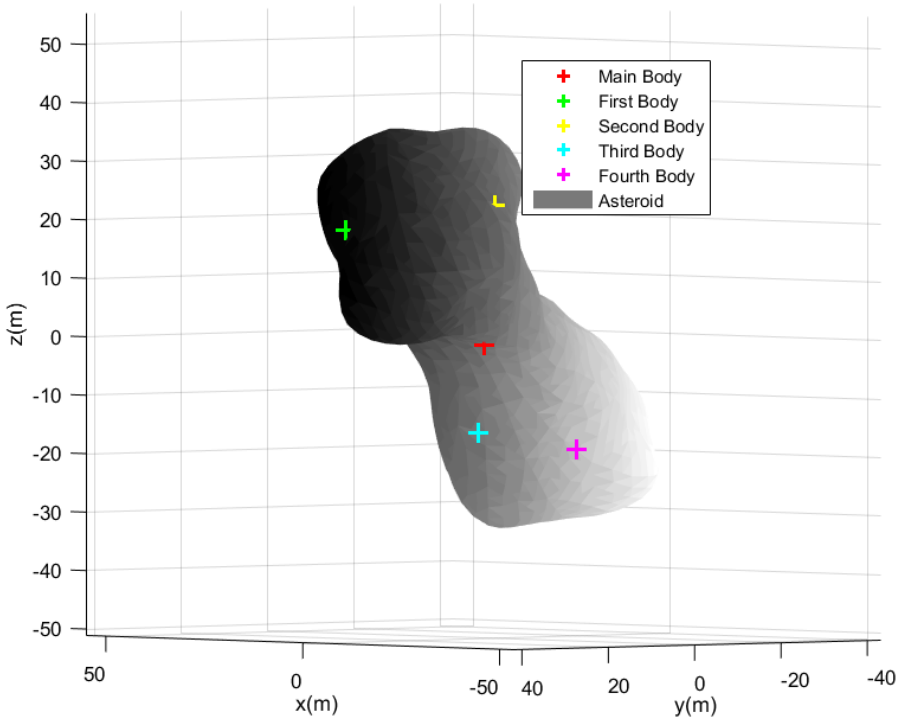

Figure 4.19: CV and KEI's impact location on a scaled 216 Kleopatra (100 m diameter).

scheme not reacting to sharp changes in the LOS rate value due to pixel location changes. By doing so, however, the averaging filter creates a dampened response, which may cause the intercepting spacecraft to miss the target. If this situation were simulated, a weighted averaging smoothing scheme could be used. The depiction of one of the KEI's can be seen in Figure 4.17, which shows similar time histories to that of the CV. This KEI uses a weighted average due to needing to shift impact location when the asteroid begins to be resolved. A delay in the actual impact location could cause a failure in intercepting the target.

After the image undergoes thresholding, the targeted locations for the detected blob object are found by using the same method for a noiseless system. The targeted impact locations for the CV and KEI's are shown in Figure 4.18. It can be seen that this image is binary; either white or black. The white indicates the object. These impact locations are very similar to the locations found by the noiseless system since the blob detected

is of similar shape to that of the actual asteroid. Information shown in Figures 4.16 to 4.18, along with other KEI's information, result in asteroid intercept. Asteroid intercept locations can be seen in Figure 4.19, where the colored pluses indicated a KEI or the CV. All interceptors impact the small, 100 meter asteroid. Not all KEIs intercept at the targeted locations, which is due to the average filter, triggering scheme, and image resolution at the time of thrusters turning off.

4.5 Future Work

While impacting one target using multiple KEIs is a starting point of our research, future work will involve the incorporations of targeting and impacting multiple targets using a single or multiple camera system implemented on each KEI. The proposed scheme would include the use of object recognition for multiple images. Since this scheme uses blob detection, Hu's moments could be used to determine common objects in multiple images. Other directions include star inclusion, star illumination, background saturation, and background estimation as well as subtraction, all of which have been explored by other researchers in the past.

4.6 Conclusion

This chapter has described a new non-nuclear MKIV (Multiple Kinetic-energy Impactor Vehicle) system that can fragment or pulverize small asteroids (< 150 m) detected with short mission lead times (< 10 years). A brief description of the image segmentation, image thresholding, and impact-location predictions on the target using image processing on a mono-camera system has been presented. It was assumed that terminal guidance and control commands can be generated from the main carrier vehicle for all other KEIs. It has also been shown, through simulations, that the MKIV system can

successfully intercept a target asteroid that is as small as 100 meters in diameter using visual camera data.

CHAPTER 5. ORBITAL CHARACTERIZATION OF A BINARY-ASTEROID TARGET

5.1 Introduction

This chapter investigates the Minimum Orbit Intersection Distance (MOID) estimation and the Full-Two-Body Problem (F2BP) formulation, which play a key role for a rendezvous mission to an asteroid. The MOID value determines, not including position as a function of time, what the minimum distance between two objects of interest is. In this case, one object of interest is the Earth. Computing this value helps to give an impact risk estimation of objects that come close to Earth's orbit. The other topic, the F2BP, explores the mutual gravitational and mutual torques experienced between two bodies. This is particularly helpful when conducting simulation around complex binary geometries such as the Didymos system. If necessary, the formulation can be extended to multiple bodies, which could include the orbiting dynamics of a spacecraft. The research objective herein is to estimate the fuel required to maintain a stable orbit in complex gravity fields, while observing both the self-orbiting bodies.

5.2 Minimum Orbit Intersection Distance (MOID) Computation

Minimum Orbit Intersection Distances (MOIDs) for objects are used to help evaluate the potential of an asteroid collision event [88]. Sitarski [19] found a method that

estimates the MOID for any two given orbits. This method was developed the 1960's, and has been considered, sometimes modified, and occasionally used during the past few decades [89, 90, 91].

5.2.1 MOID Problem Formulation and Solution

The research work herein will follow the formulation for the MOID computation described in [19]. First, two objects of interest must be selected. In general, any object's orbit can be compared with another as long as both orbits are given in the same reference frame. Here, the positions of both objects, given in the same heliocentric coordinate system, are described as

$$\mathbf{R}_1 = \begin{bmatrix} x_1 \\ y_1 \\ z_1 \end{bmatrix} \quad \text{and} \quad \mathbf{R}_2 = \begin{bmatrix} x_2 \\ y_2 \\ z_2 \end{bmatrix} \tag{5.1}$$

These vectors can also be represented by a coordinate transformation in the form of

$$\mathbf{R}_1 = \mathbf{H}_1 \, \mathbf{U}_1, \quad \mathbf{R}_2 = \mathbf{H}_2 \, \mathbf{U}_2 \tag{5.2}$$

where

$$\mathbf{U}_1 = \begin{bmatrix} R_1 \cos(\nu_1) \\ R_1 \sin(\nu_1) \\ 0 \end{bmatrix}, \quad \mathbf{U}_2 = \begin{bmatrix} R_2 \cos(\nu_2) \\ R_2 \sin(\nu_2) \\ 0 \end{bmatrix},$$

$$R_1 = \frac{p_1}{1+e_1 \cos(\nu_1)} \quad \text{and} \quad R_2 = \frac{p_2}{1+e_2 \cos(\nu_2)}$$

and

$$\mathbf{H}_1 = \begin{bmatrix} 1 & 0 & 0 \\ 0 & \cos(i_1) & -\sin(i_1) \\ 0 & \sin(i_1) & \cos(i_1) \end{bmatrix} \begin{bmatrix} \cos(\omega_1) & -\sin(\omega_1) & 0 \\ \sin(\omega_1) & \cos(\omega_1) & 0 \\ 0 & 0 & 1 \end{bmatrix}$$

$$\mathbf{H}_2 = \begin{bmatrix} \cos(\Omega_2-\Omega_1) & -\sin(\Omega_2-\Omega_1) & 0 \\ \sin(\Omega_2-\Omega_1) & \cos(\Omega_2-\Omega_1) & 0 \\ 0 & 0 & 1 \end{bmatrix} \begin{bmatrix} 1 & 0 & 0 \\ 0 & \cos(i_2) & -\sin(i_2) \\ 0 & \sin(i_2) & \cos(i_2) \end{bmatrix} \begin{bmatrix} \cos(\omega_2) & -\sin(\omega_2) & 0 \\ \sin(\omega_2) & \cos(\omega_2) & 0 \\ 0 & 0 & 1 \end{bmatrix}$$

where $p = q\ (1+e)$, q is the corresponding orbit's perihelion distance, e is the orbit's eccentricity, $p = a\ (1-e^2)$ (when $e < 1$), and a is the orbit's semi-major axis. For each equation, the subscripts indicate the orbit parameters that belong to the corresponding orbit, 1 is orbit one and 2 is orbit two. The orbital elements are: a is the semi-major axis, e is the eccentricity, Ω is the longitude of ascending node, i is the inclination, ν is the true anomaly, and ω is the argument of periapsis. From here, the objective is to minimize the distance between the two orbits or by minimizing the square of the distance. This function is then given by

$$f(\nu_1, \nu_2) = \frac{1}{2} \left\| \mathbf{H}_1\ \mathbf{U}_1 - \mathbf{H}_2\ \mathbf{U}_2 \right\|^2 \tag{5.3}$$

The minimum values for the function can be found by differentiating Equation 5.3. After completing the differentiation, further detail can be found in [19] Equation 4 to 8, derivatives with respect to each orbit's ν are

$$\frac{\partial f}{\partial \nu_1} = \frac{R_1}{p_1} \left[e_1 R_1 Y_1 + Y_1(KX_2 + MY_2) - (e_1 R_1 + X_1)(LX_2 + NY_2) \right] \tag{5.4a}$$

$$\frac{\partial f}{\partial \nu_2} = \frac{R_2}{p_2} \left[e_2 R_2 Y_2 + Y_2(KX_1 + LY_1) - (e_2 R_2 + X_2)(MX_1 + NY_1) \right] \tag{5.4b}$$

where

$$X_1 = R_1\ \cos(\nu_1), \quad X_2 = R_2\ \cos(\nu_2)$$

$$Y_1 = R_1\ \sin(\nu_1), \quad Y_2 = R_2\ \sin(\nu_2)$$

and

$$K = \sum_{i=1}^{3} \mathbf{H}_1(i,1)\ \mathbf{H}_2(i,1)$$

$$L = \sum_{i=1}^{3} \mathbf{H}_1(i,2)\ \mathbf{H}_2(i,1)$$

$$M = \sum_{i=1}^{3} \mathbf{H}_1(i,1)\ \mathbf{H}_2(i,2)$$

$$N = \sum_{i=1}^{3} \mathbf{H}_1(i,2)\ \mathbf{H}_2(i,2)$$

where i indicates the row access, while the second number in the matrix parentheses access the matrix's column. However, Equations 5.4 have conditions that will result in the existence of an minimum of Equation 5.3. These conditions are given by

$$\frac{\partial f}{\partial \nu_1} = 0, \quad \frac{\partial f}{\partial \nu_2} = 0$$

and

$$\frac{\partial^2 f}{\partial \nu_1^2}\ \frac{\partial^2 f}{\partial \nu_2^2} - \left(\frac{\partial^2 f}{\partial \nu_1 \partial \nu_2}\right)^2 > 0, \quad \text{and} \quad \frac{\partial^2 f}{\partial \nu_1^2} > 0$$

where

$$\frac{\partial^2 f}{\partial \nu_1^2} = \frac{R_1}{p_1}\left[2e_1R_1Y_1\frac{\partial f}{\partial \nu_1} + e_1R_1\frac{R_1}{p_1}(e_1R_1+X_1) + X_1(KX_2+MY_2) + Y_1(LX_2+NY_2)\right]$$

$$\frac{\partial^2 f}{\partial \nu_2^2} = \frac{R_2}{p_2}\left[2e_2R_2Y_2\frac{\partial f}{\partial \nu_2} + e_2R_2\frac{R_2}{p_2}(e_2R_2+X_2) + X_2(KX_1+LY_1) + Y_2(MX_1+NY_1)\right]$$

$$\frac{\partial^2 f}{\partial \nu_1 \partial \nu_2} = \frac{R_1}{p_1}\frac{R_2}{p_2}\left[(e_2R_2+X_2)[N(e_1R_1+X_1) - MY_1] - Y_2[L(e_1R_1+X_1) - KY_1]\right]$$

Implementing these conditions into Equations 5.4a and 5.4b result in two trigonometric forms that are functions of ν_1 and ν_2, which are

$$e_1R_1Y_1 + Y_1(KX_2+MY_2) - (e_1R_1+X_1)(LX_2+NY_2) = 0 \tag{5.7a}$$

$$e_2R_2Y_2+Y_2(KX_1+LY_1)-(e_2R_2+X_2)(MX_1+NY_1)=0 \tag{5.7b}$$

Equations 5.7a and 5.7b can be solved numerically. However, we consider rewriting Equation 5.7a as

$$s+t\ \sin(\nu_2)+w\ \cos(\nu_2)=0 \tag{5.8}$$

where

$$s=\frac{e_1R_1Y_1}{p_2},\quad t=MY_1-N(e_1R_1+X_1),\quad \text{and}\quad w=e_2s+KY_1-L(e_1R_1+X_1) \tag{5.9}$$

By making these variable definitions, we obtain the solutions to Equation 5.8 as

$$1)\quad \sin(\nu_2)=\frac{-t\ s+w\sqrt{l}}{m}\qquad \cos(\nu_2)=\frac{-w\ s-t\sqrt{l}}{m} \tag{5.10a}$$

$$2)\quad \sin(\nu_2)=\frac{-t\ s-w\sqrt{l}}{m}\qquad \cos(\nu_2)=\frac{-w\ s+t\sqrt{l}}{m} \tag{5.10b}$$

where $m=t^2+w^2$ and $l=m-s^2$. The variable ν_1 can only ever vary from 0 to $2pi$, if the eccentricity of the orbit is less than or equal one. If e_1 is greater than one, ν_1 varies from $-\cos^{-1}(-1/e_1)$ to $\cos^{-1}(-1/e_1)$. Since these bounds for ν_1 are established, an iterative solution can be determined.

This method is done by varying ν_1 from the lower bound to the upper bound. At each iteration, the value of l must greater than 0 to evaluate the solutions of Equations 5.10a and 5.10b, ν_2. Remember, X_1 and Y_1 must be evaluated at each step. After this is completed, evaluate X_2, Y_2 and Equation 5.7b using the solution of Equation 5.10a. Be sure to save the value of 5.7b at the current and previous iterations, which will be denoted as Q_i and Q_{i-1}. The goal is to find the points where Equation 5.7b switches sign, the zero crossing. With this current and previous evaluation memory, the values of

ν_1 must also be stored in a similar manner, which will be given by ν_{1_i} and $\nu_{1_{i-1}}$. Once a zero crossing point is found, a new ν_1, ν_{1_N}, can be evaluated as

$$\nu_{1_N} = (1-z)\ \nu_{1_i} + z\ \nu_{1_{i-1}} \tag{5.11}$$

where z is given by

$$z = \left| \frac{Q_i}{Q_i - Q_{i-1}} \right| \tag{5.12}$$

A new X_1 and Y_1 are then evaluated using the new estimated ν_1 at zero crossing of Equation 5.7b. Use these values to solve for the corresponding ν_2 value using Regular False method, which solves for the zero of Equation 5.7b. The inputs for the method are the new X_1, Y_1, p_2, e_2, K, L, M, N, the two values of ν_2 that were found to have a zero crossing of Equation 5.7b (these values serve as the beginning bounds) and an exit tolerance. A solution is then found. Recalculate the new X_2 and Y_2. Then perform the evaluation of Equation 5.3 to find a value, and store this value. However, Equation 5.3 must be multiplied by two and taken to the power of one-half. This is given by

$$distance = \|\mathbf{H}_1\mathbf{U}_1 - \mathbf{H}_2\mathbf{U}_2\|_2 \tag{5.13}$$

Repeat the afore mentioned process for the solution of Equation 5.10b. At the end, find the minimum values from both the solutions of 5.10. A recommendation is to not store the values from Equation 5.3, but to check if the new value calculated is less than the current and re-save the minimum value. A list of steps can be seen in the list below.

1. Evaluate $\mathbf{H}_1$ and $\mathbf{H}_2$.
2. Evaluate K, L, N, and M.
3. Start ν_1 step through. 2000 steps from beginning to end will suffice. If $e_2 > .95$, then 50000 steps should be used.

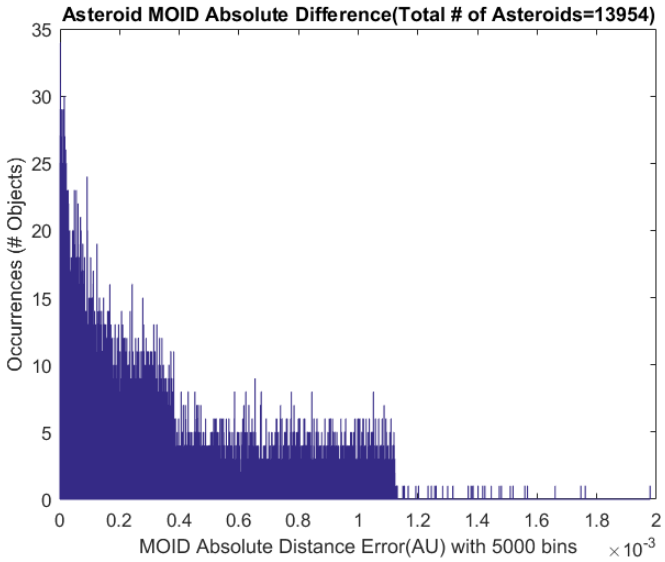

Figure 5.1: 13954 object histogram of absolute MOID difference compared to SBDB.

4. Calculate X_1 and Y_1 at ν_1, s, t, w, m, and l.

5. Check to see if $l > 0$. If it is, continue with the calculations.

6. Calculate ν_2 from Equation 5.10a and store value.

7. Calculate X_2 and Y_2 at ν_2.

8. Evaluate Equation 5.7b and store value.

9. Step forward and check to see if Equation 5.7b changes signs. If it does continue.

10. Calculate ν_{1_N}, X_1, and Y_1.

11. Use Regula Falsi to solve Equation 5.7b using the current and previous value of ν_2 and obtain the zero solution of Equation 5.7b, ν_2.

12. Evaluate new X_2 and Y_2.

13. Solve for the distance given by Equation 5.13.

14. Do steps 6 through 12 for ν_2 from Equation 5.10b.

15. Find minimum distance value.

If large databases of objects need to perform MOID calculations, this process can be parallelized. Currently, this method is parallelized using MATLAB's "parfor" structure.

5.2.2 Results and Comparison

Results, when using Earth as the main orbit, are compared with the MOID values given by the Small Bodies Database (SBDB) and single orbit evaluation of Gronchi's method [89]. Parameters for Earth can be found in Table 5.1 A FORTRAN code of Gronchi's method can be found at [92]. First 13954 Near Earth Asteroids (NEA's) were gathered from the SBDB. A histogram of the absolute differences between the MOID's from the SBDB and the method provided here are given in Figure 5.1. The statistics are as follows: μ = 3.4658e-4, σ = 3.2257e-4, min = 3.3248e-9, and max = 1.9786e-3. These agree to at least the max difference, $\approx 2e{-}3$.

A second test was ran using 702746 asteroids. Yet again, a comparison was done with the SBDB. However, as it can be seen in Figure 5.2, the MOID values do not match well for some objects. The statistics corresponding to the values given for the absolute differences are given as follows: μ = 6.4802e-4, σ = 4.5805e-3, min = N/A, and max = 1.9766. These agree to at least the max difference, $\approx$ 1.9766. The minimum was not recorded due to a population of asteroids in the SBDB failing to have a MOID evaluation. As it may be seen, there are a few asteroids that may appear to be outliers. Four asteroids, corresponding to the top four maximum absolute error, are examined. Table 5.2 presents the results for four outlying absolute error objects and MOID comparison. Gronchi's method shows that the minimum values found by SBDB are actually saddle points or other local minimum. MOID's from within this section and the Gronchi method match with the grid search method. Distance plots generated by the grid search method for the four asteroids given can be seen in Figures 5.3 through 5.6. The Points on each plot correspond to values for the top four large absolute errors in Table 5.2.

Table 5.1: Earth parameter values

Earth Variable Symbol	Variable Value
a	1.000368806233832 (AU)
e	1.705811321949892E-02
i	2.180444240341850E-03 (deg)
Ω	212.0592104472283 (deg)
ω	249.8152155810121 (deg)

Table 5.2: MOID comparison table

Object Name	SBDB MOID	Section Method MOID	Gronchi MOID	Grid Search (10000x10000) MOID	Absolute Errors SBDB Against Section Method
2014 MH55	5.42006	3.44344353398923	3.443443535683821	3.44344358030805	1.97661646601077
2014 TZ33	10.3241	8.45752160875998	8.457521609644864	8.45752165382934	1.86657839124002
2009 FW23	2.1147	0.839425529712386	0.839425523928287	0.839425607433946	1.27527447028761
2005 SB223	2.97832	2.3086025157969	2.308602501239387	2.30860264132135	0.669717484203098

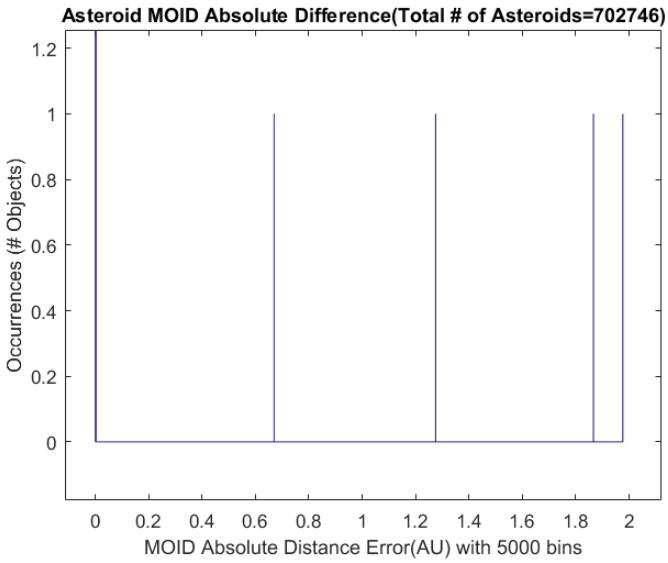

Figure 5.2: 702746 object zoomed histogram of absolute MOID difference compared to SBDB.

Table 5.3: 433 Eros MOID comparison table (out to 15 decimal places, besides SBDB)

Object Name	SBDB MOID	Paper's MOID	Gronchi's MOID	Grid Search (50000x50000) MOID
433 Eros	0.148887	0.148721656899931	0.148721656899935	0.148721657144012

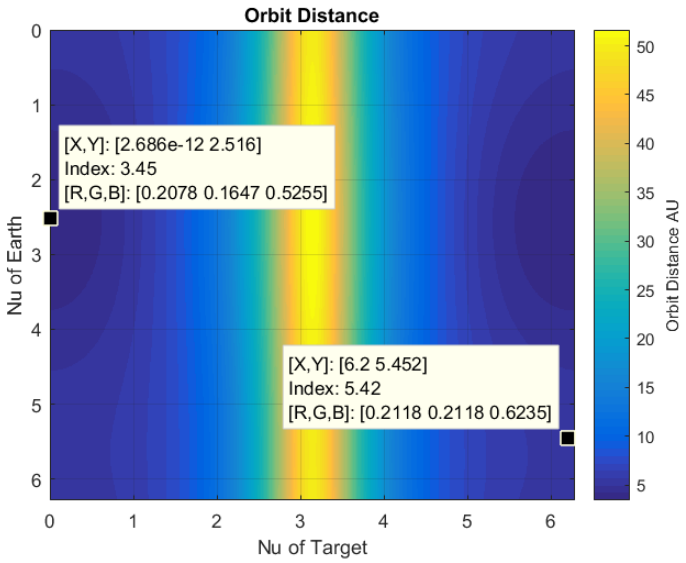

Figure 5.3: Object 2014 MH55 and its distance contour.

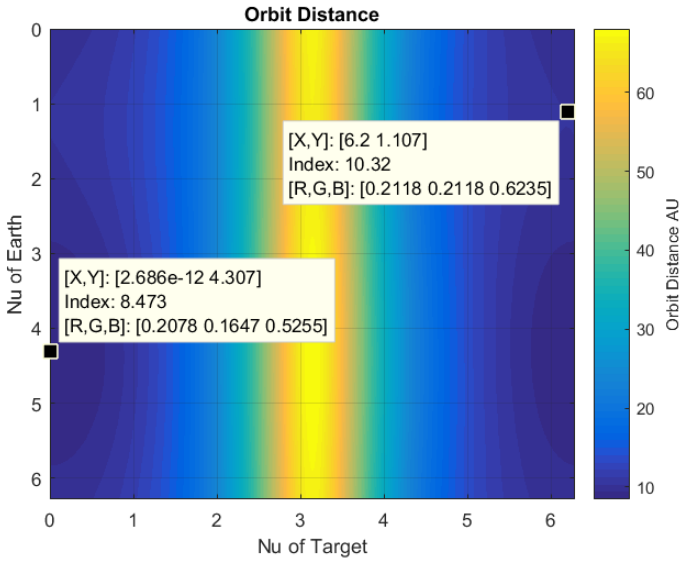

Figure 5.4: Object 2014 TZ33 and its distance contour.

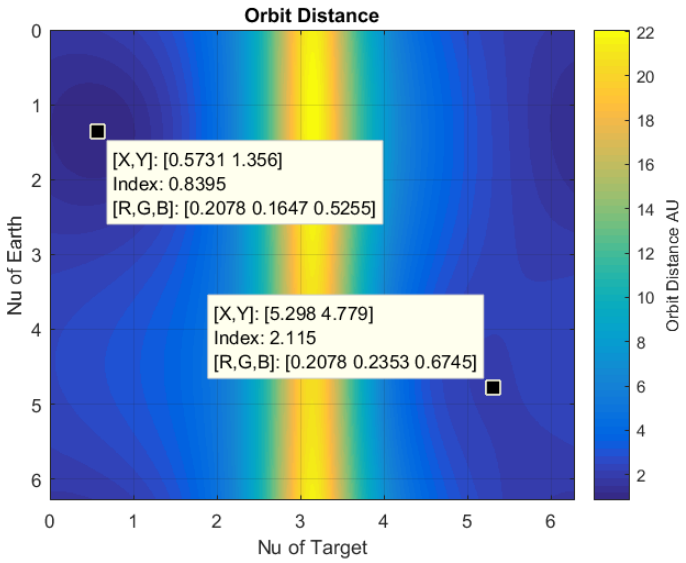

Figure 5.5: Object 2009 FW23 and its distance contour.

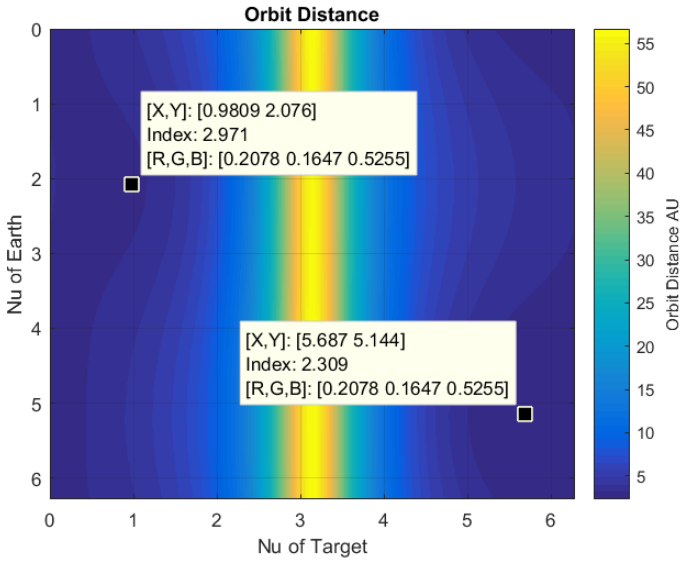

Figure 5.6: Object 2005 SB223 and its distance contour.

Since there are discrepancies between SBDB and the method herein as well as Gronchi, MOID re-evaluation of the 13954 NEA population is conducted. However, for simplicity, a model comparison is done for a single asteroid. This asteroid is 433 Eros. Values corresponding to the compared methods are given in Table 5.3. As it can be seen, the MOID within the SBDB does not match the grid search method out past 4 significant digits, which was the error found between the method in this section and the SBDB. In contrast, the method presented herein, with the ν_{1_N} update, shows to agree with Gronchi's method out to 14 decimal places for this scenario. These values both agree with the grid search method out to 8 decimal places.

5.2.3 Conclusion

This section has gathered and put forth a flow chart for evaluating the MOID for any given two objects of interest. Moreover, an improvement for finding the minimum crossing angle was presented. In addition, each method was evaluated against the grid search method, and the method presented herein was accurate out to at least six decimal places (initial limit of Gronchi's output) when comparing against the grid search method in some scenarios. When expanding the readable output to 15 decimal place, and when considering 433 Eros, the method in this section agrees with Gronchi out to 14 decimal places. Both methods have an agreement to 8 decimal places comparing to the grid search method.

5.3 Full-2-Body Problem (F2BP) Using Polyhedron Objects

5.3.1 Introduction

The Full rigid two-Body Problem (F2BP) as been studied for the case of binary asteroid systems, which include asteroid (66391) 1999 KW4. It has been shown, by using the mutual potential and a discrete equation of motion formulation, that the dynamics of

both bodies can be accurately represented [93, 94]. The discrete integrator used was the Lea Group Variational Integrator (LGVI), which preserves desirable system properties. However, [93] and [94] used the form in [95], which did not incorporate the use of an arbitrary body as was demonstrated by [96]. More computationally intensive schemes, which implement Polyhedron shape models and partial derivatives of mutual potential, were used to determine the mutual forces and mutual torques [97, 21]. In [93] and [94], as well as [97] and [21], the relative motion of the bodies was propagated. For reconstructive purposes, one of the bodies required propagation in the initial frame. Using the relative motion equations was advised by [21] due to "reduced-size state vector for relative EOM compared to inertial EOM."

The implementation presented in this section follows the formulation for inertial forces and moments acting on each body, which was discussed in [21]. However, a slightly different approach is investigated for calculating specific tensors. These rank 4 tensors are found by directly differentiating the polyhedron vertex matrix by their respective orientation matrix transpose (global to body frame). The two bodies are propagated in time using the discrete LGVI while having a 40 second time step. In addition, the simulation can be conducted with any arbitrary shaped asteroid as long as the file uses triangular faces. Moreover, non-convex but closed shapes may be used, which differs from [21] where solely convex shapes may be considered.

5.3.2 Full-Two-Body Problem Formulation

The Full-Two-Body Problem (F2BP) consists of mutual gravitation as well as mutual torque of each body. This is very useful if either body is irregularly shaped. Such a case can be seen in binary asteroid situations, such as 65803 Didymos and the binary asteroid 1999 KW 4 [98, 99]. An effective way to estimate the dynamics of such systems is to implement the mutual potential equation. From that equation, the force on each object

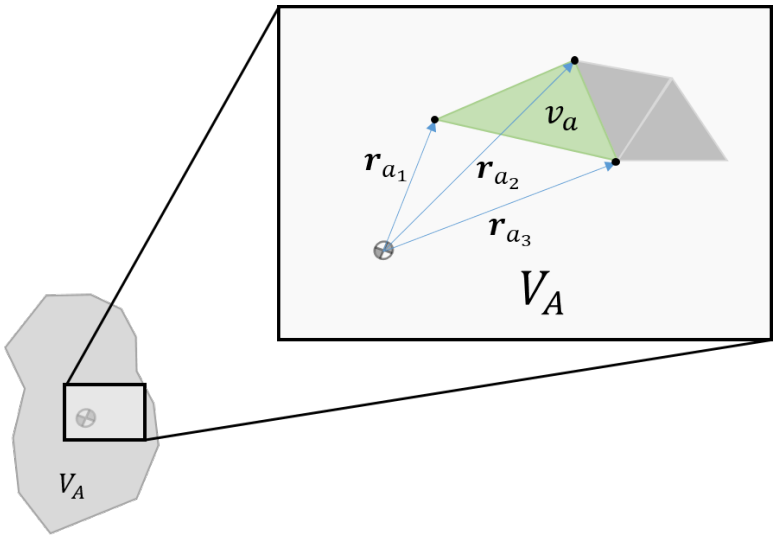

Figure 5.7: Cutout of object A showing how the surface is made up of triangular faces and how simplexes are constructed using vectors to the triangle's vertexes. Each body will have similar definition.

as well as the bodies' torques can be calculated. The following subsections follow the formulation in [100], which can be refereed to for further details and explanations.

5.3.2.1 Mutual Potential and Its Expansion

As given in [100] the mutual potential, in integral form, over both of the bodies' volumes is

$$U = \iiint_{V_A} \iiint_{V_B} \frac{1}{r} \, dV_B \, dV_A \tag{5.14}$$

where r is the distance between each differential volume of the two bodies. Each body is made up of triangular faces, which results in body tetrahedrons or simplexes for each face. One of the vertexes of each tetrahedron lies at the centroid of the body, which corresponds to the center of mass. With this formulation, the potential equation can be

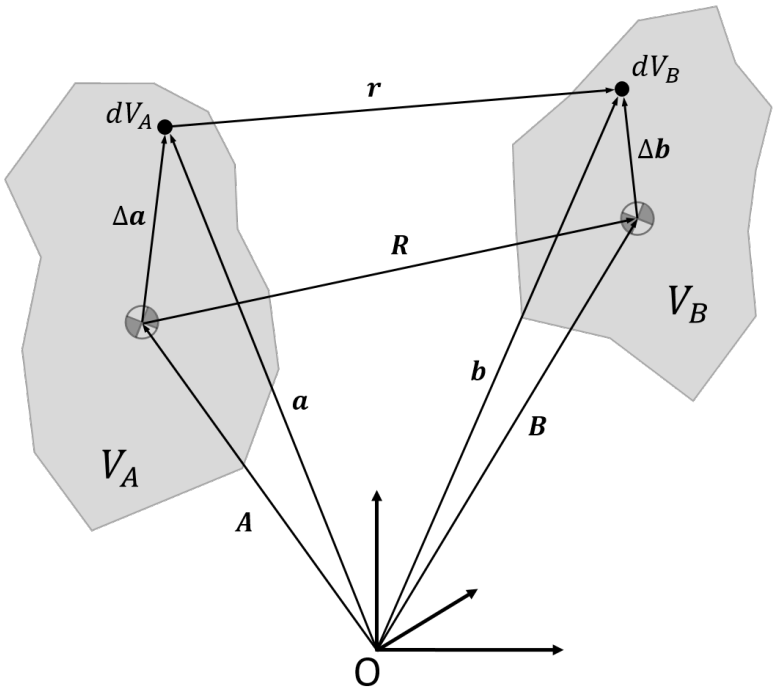

Figure 5.8: Polyhedron depiction and variable display on two polyhedron bodies.

rewritten as the summation over each simplex volume, v_a and v_b. This expression is as follows

$$U = \sum_{v_a \epsilon V_A} \sum_{v_b \epsilon V_B} \iiint_{v_a} \iiint_{v_b} \frac{1}{r} \, dv_b \, dv_a \tag{5.15}$$

An illustration of the triangle faces and how a simplex would form can be seen in Figure 5.7. The variable r can be expressed in vector notation. A depiction of the two-body scenario can be seen in Figure 5.8, which shows specific variables and hence, their definitions. With the visual vector definitions in the Figure, the following equation holds

$$\mathbf{r} = \mathbf{b} - \mathbf{a} = (\mathbf{B} - \mathbf{A}) + (\Delta\mathbf{b} - \Delta\mathbf{a}) \tag{5.16}$$

This can be further condensed by defining two new variables, $\mathbf{R}$ and $\mathbf{h}$, which are given by

$$\mathbf{R} = \mathbf{B} - \mathbf{A}$$

$$\mathbf{h} = \Delta\mathbf{b} - \Delta\mathbf{a}$$

Equation 5.16 can then be rewritten as

$$\mathbf{r} = \mathbf{R} + \mathbf{h} \tag{5.17}$$

From Equation 5.17, the distance between each differential volume, r can be found by the Euclidean norm of $\mathbf{r}$, which is

$$\begin{aligned} r &= \sqrt{(\mathbf{R}+\mathbf{h})\cdot(\mathbf{R}+\mathbf{h})} \\ &= \sqrt{\mathbf{R}\cdot\mathbf{R}+2\mathbf{R}\cdot\mathbf{h}+\mathbf{h}\cdot\mathbf{h}} \end{aligned}$$

$$= \sqrt{R^2+h^2+2\mathbf{R}\cdot\mathbf{h}} \tag{5.18}$$

where R and h are the Euclidean norms of $\mathbf{R}$ and $\mathbf{h}$. Therefore, $1/r$ can be expressed simply as the reciprocal of Equation 5.18

$$\frac{1}{r} = \left(R^2+h^2+2\mathbf{R}\cdot\mathbf{h}\right)^{-1/2} \tag{5.19}$$

5.3.2.2 Expansion of $1/r$

Using Legendre polynomials to expand a portion of the gravity potential is commonly used when estimating the spherical harmonics of a source [101]. Here, a similar formulation is conducted for $1/r$. By factoring $1/R^2$ from Equation 5.19 and slight manipulation, we obtain the following:

$$\frac{1}{r} = \frac{1}{R}\left[1+\left(\frac{h}{R}\right)^2+2\left(\frac{h}{R}\right)\left(\frac{\mathbf{R}\cdot\mathbf{h}}{R\,h}\right)\right]^{-1/2} \tag{5.20}$$

Degree (n)	Polynomial of $P_n(x)$
0	1
1	x
2	$\frac{1}{2}(3x^2-1)$
3	$\frac{1}{2}(5x^3-3x)$
4	$\frac{1}{8}(35x^4-30x^2+3)$
5	$\frac{1}{8}(63x^5-70x^3+15x)$
6	$\frac{1}{16}(231x^6-315x^4+105x^2-5)$
7	$\frac{1}{16}(429x^7-693x^5+315x^3-35x)$
8	$\frac{1}{128}(6435x^8-12012x^6+6930x^4-1260x^2+35)$

Figure 5.9: Legendre Polynomials up to the 8th degree.

By incorporating a summation, this expression can then be rewritten using Legendre polynomial form

$$\frac{1}{r}=\frac{1}{R}\sum_{n=0}^{\infty}\left(\frac{h}{R}\right)^n P_n\left(-\frac{\mathbf{R}\cdot\mathbf{h}}{Rh}\right) \tag{5.21}$$

where P_n is the n$^{\text{th}}$ degree Legendre polynomial. A depiction of the polynomials up to the 8th degree can be seen in Figure 5.9. Otherwise, general form for the Legendre polynomial of order n is

$$P_n(x)=\frac{1}{2^n}\sum_{k=0}^{n}\binom{n}{k}^2(x-1)^{n-k}(x+1)^k$$

$$P_n(x)=\frac{1}{2^n}\sum_{k=0}^{n}\left(\frac{n!}{(n-k)!\;k!}\right)^2(x-1)^{n-k}(x+1)^k \tag{5.22}$$

5.3.2.3 Change of Variables and Other Expressions

Since the expansion of $1/r$ is completed, transforming the integral to barycenter location simplifies the preparation of integration. Using this transformation, there must be an introduction to the Jacobian determinant, which can be computed as

$$T_a = det\left([\Delta\mathbf{r}_{a_1}, \Delta\mathbf{r}_{a_2}, \Delta\mathbf{r}_{a_3}]\right) \tag{5.23}$$

where $\Delta\mathbf{r}_{a_1}$, $\Delta\mathbf{r}_{a_2}$, and $\Delta\mathbf{r}_{a_3}$ are the column vectors corresponding to the each triangular face vertex location of body A, measured from the center of mass. Similarly, the determinant corresponding to body B is given as T_b, but must be calculated with respect to body B's triangular faces. The gravitational mutual potential can then be written as

$$U = G \sum_{v_a \epsilon V_A} \sum_{v_b \epsilon V_B} \rho_a T_a \rho_b T_b \iiint_{a'} \iiint_{b'} \frac{1}{r}\, db'\, da' \tag{5.24}$$

where a' and b' are the 'standard' simplexes of each body A and B corresponding to a transformed v_a and v_b, ρ_a is the density of v_a, ρ_b is the density of v_b, and G is the gravitational constant. Further expressions for integration are required. These expressions will have any combination of $\mathbf{h}$ or h. For convenience, the equations hereafter will be expressed in Einstein notation. A stacked matrix that contains elements of each bodies' triangular vertex locations in the inertial frame is constructed as

$$\begin{aligned}\mathbf{v}_j^i &\equiv \begin{bmatrix} \Delta x_{a_1}, & \Delta x_{a_2}, & \Delta x_{a_3}, & -\Delta x_{b_1}, & -\Delta x_{b_2}, & -\Delta x_{b_3} \\ \Delta y_{a_1}, & \Delta y_{a_2}, & \Delta y_{a_3}, & -\Delta y_{b_1}, & -\Delta y_{b_2}, & -\Delta y_{b_3} \\ \Delta z_{a_1}, & \Delta z_{a_2}, & \Delta z_{a_3}, & -\Delta z_{b_1}, & -\Delta z_{b_2}, & -\Delta z_{b_3} \end{bmatrix} \\ &= [\Delta\mathbf{r}_{a_1}, \Delta\mathbf{r}_{a_2}, \Delta\mathbf{r}_{a_3}, -\Delta\mathbf{r}_{b_1}, -\Delta\mathbf{r}_{b_2}, -\Delta\mathbf{r}_{b_3}]\end{aligned} \tag{5.25}$$

where Δx, Δy, and Δz are the x, y, and z coordinates of the triangular face vertexes with respect to each bodies' centroid location but given in inertial coordinates. A kernel variable is then defined as

$$\mathbf{q}_i \equiv [m_a, n_a, o_a, m_b, n_b, o_b] \tag{5.26}$$

where m, n, and o are the barycenter variables used for the transformation. With these definitions, $\mathbf{h}$, $\mathbf{R}\cdot\mathbf{h}$, and h^2 can be rewritten as

$$\mathbf{h}_j = \mathbf{q}_i \mathbf{v}^i_j \tag{5.27}$$

$$\mathbf{R}\cdot\mathbf{h} = \mathbf{q}_i \mathbf{w}^i \tag{5.28}$$

where $\mathbf{w}^i \equiv \mathbf{R}^j \mathbf{v}^i_j$.

$$h^2 = \mathbf{q}_{ij} \mathbf{r}^{ij} \tag{5.29}$$

where $\mathbf{r}^{ij}$ is a 6×6 rank-2 tensor given by

$$\mathbf{r}^{ij} = \mathbf{v}^i_k \mathbf{v}^j_k \tag{5.30}$$

For simplicity and generalization for the outer product of the kernel $\mathbf{q}$, a rank-k integrand can be written as

$$\mathbf{q}_{i_1 i_2 \ldots i_k} = \mathbf{q}_{i_1} \mathbf{q}_{i_2} \ldots . \mathbf{q}_{i_k}$$

5.3.2.4 Integration for Mutual Potential

When substituting tetrahedron variables into the transformed mutual potential, Equation 5.24, it can be noticed that they are not independent of the integration. This forms different rank integrands of $\mathbf{q}$. Since the transformation is conducted, the elements for

any rank of $\mathbf{q}$ can be written as a sum collection of exponents in each integrand socket, which is then denoted as $\bar{\mathbf{q}}$. For example, the rank-1 integrand is

$$\bar{\mathbf{q}}_i = \begin{bmatrix} (100|000) & (010|000) & (001|000) & (000|100) & (000|010) & (000|001) \end{bmatrix}$$

The rank-2 integrand is then given by

$$\bar{\mathbf{q}}_{ij} = \begin{bmatrix} (200|000) & (110|000) & (101|000) & (100|100) & (100|010) & (100|001) \\ (110|000) & (020|000) & (011|000) & (010|100) & (010|010) & (010|001) \\ (101|000) & (011|000) & (002|000) & (001|100) & (001|010) & (001|001) \\ (100|100) & (010|100) & (001|100) & (000|200) & (000|110) & (000|101) \\ (100|010) & (010|010) & (001|010) & (000|110) & (000|020) & (000|011) \\ (100|001) & (010|001) & (001|001) & (000|101) & (000|011) & (000|002) \end{bmatrix}$$

The vertical line separating the collection of 3 exponents denotes the independence of the variable sets associated for each body during the iterated volume integrals. This volume integral, due to the change of variables, can then be written as

$$\int_0^1 \int_0^{1-m} \int_0^{1-m-n} m^I n^J o^K \, do \, dm \, dn = \frac{I! \; J! \; K!}{(I+J+K+3)!} \tag{5.31}$$

where I, J, and K are the values of the collection in each matrix element. The double volume integral result is then written as

$$\mathbf{Q}_{i_1 \ldots i_k} = \iiint_{01} \iiint_{01} \mathbf{q}_{i_1 \ldots i_k} db' da' \tag{5.32}$$

The values for $\mathbf{Q}_i$, using the matrix element collection from $\bar{\mathbf{q}}_i$ and evaluating them with Equation 5.31, are

$$\mathbf{Q}_i = \frac{1}{144} \begin{bmatrix} 1 & 1 & 1 & 1 & 1 & 1 \end{bmatrix}$$

Each collection result per matrix element must be multiplied by the result of the collection on the other side of the horizontal bar. For example, $\mathbf{Q}_1 = \frac{1! \; 0! \; 0!}{(1+0+0+3)!} \frac{0! \; 0! \; 0!}{(0+0+0+3)!} = \frac{1}{144}$. Another example can be seen with evaluating $\mathbf{Q}_{ij}$

```
! Rank 0
slide = 0
Q = eval(slide)
slide = 0


! Rank 1
slide = 0
DO i = 1,6
    slide(i) = 1

    Qi(i) = eval(slide)
    slide = 0
END DO


! Rank 2
slide = 0
DO i = 1,6
    DO j = 1,6
        slide(i) = 1
        slide(j) = slide(j) + 1

        Qij(i,j) = eval(slide)
        slide = 0
    END DO
END DO
```

```
! Rank 3
slide = 0
DO k = 1,6
    DO i = 1,6
        DO j = 1,6
            slide(k) = 1
            slide(j) = slide(j) + 1
            slide(i) = slide(i) + 1

            Qijk(i,j,k) = eval(slide)
            slide = 0
        END DO
    END DO
END DO

! Rank 4
slide = 0
DO m = 1,6
    DO k = 1,6
        DO i = 1,6
            DO j = 1,6
                slide(m) = 1
                slide(k) = slide(k) + 1
                slide(j) = slide(j) + 1
                slide(i) = slide(i) + 1

                Qijkm(i,j,k,m) = eval(slide)
                slide = 0
            END DO
        END DO
    END DO
END DO
```

Figure 5.10: Rank-0 to Rank-4 $\mathbf{Q}$ matrix. The variable "slide" is a 1×6 vector.

$$\mathbf{Q}_{ij} = \frac{1}{2880}\begin{bmatrix} 8 & 4 & 4 & 5 & 5 & 5 \\ 4 & 8 & 4 & 5 & 5 & 5 \\ 4 & 4 & 8 & 5 & 5 & 5 \\ 5 & 5 & 5 & 8 & 4 & 4 \\ 5 & 5 & 5 & 4 & 8 & 4 \\ 5 & 5 & 5 & 4 & 4 & 8 \end{bmatrix}$$

Another evaluation example for the first element of $\mathbf{Q}_{ij}$ is: $\mathbf{Q}_{11} = \frac{2!\ 0!\ 0!}{(2+0+0+3)!}\frac{0!\ 0!\ 0!}{(0+0+0+3)!} = \frac{2}{720} = \frac{8}{2880}$. Example FORTRAN code for generating rank-0 to rank-4 tensors can be seen in Figure 5.10. Moreover, the "eval" and "fac" functions within the FORTRAN code can be found in Figure 5.11. From these figures, it can be seen that any rank tensor, $\mathbf{Q}_{i_1 \ldots i_k}$, can be generated by including another loop as well as another line for the "slide" variable. This current implementation will fail when exploring higher rank

```
!*****************************************************************************

INTEGER FUNCTION fac(n)
IMPLICIT NONE
INTEGER, INTENT(IN) :: n
INTEGER :: i, Ans

Ans = 1
DO i = 1,n
    Ans = Ans*i
END DO

fac = Ans

END FUNCTION

!*****************************************************************************

REAL(8) FUNCTION eval(sl)
IMPLICIT NONE
INTEGER, INTENT(IN) :: sl(6)
INTEGER :: fac

eval = DBLE(fac(sl(1))*fac(sl(2))*fac(sl(3)))/DBLE(fac(sl(1)+sl(2)+sl(3)+3))


eval = eval * DBLE(fac(sl(4))*fac(sl(5))*fac(sl(6)))/DBLE(fac(sl(4)+sl(5)+sl(6)+3))

END FUNCTION


!*****************************************************************************
```

Figure 5.11: Evaluation function corresponding to Equation 5.31 and used in Figure 5.10.

tensors (>15) due to compiler limitations. With everything able to be determined, the mutual potential, out to the 3rd degree, is then

$$
\begin{aligned}
U &= G \sum_{v_a \epsilon V_A} \sum_{v_b \epsilon V_B} \rho_a T_a \rho_b T_b \iiint_{a'} \iiint_{b'} \frac{1}{r}\, db'\, da' \\
&= G \sum_{a \epsilon A} \sum_{b \epsilon B} \rho_a T_a \rho_b T_b \left(\left[\frac{\mathbf{Q}}{R} \right] + \left[-\frac{\mathbf{Q}_i \mathbf{w}^i}{R^3} \right] + \left[-\frac{\mathbf{Q}_{ij} \mathbf{r}^{ij}}{2R^3} + \frac{3\mathbf{Q}_{ij} \mathbf{w}^i \mathbf{w}^j}{2R^5} \right] \right. \\
&\quad \left. + \left[\frac{3\mathbf{Q}_{ijk} \mathbf{r}^{ij} \mathbf{w}^k}{2R^5} - \frac{5\mathbf{Q}_{ijk} \mathbf{w}^i \mathbf{w}^j \mathbf{w}^k}{2R^7} \right] + \ldots\ldots \right)
\end{aligned}
\tag{5.33}
$$

Further details can be found in [100]. For convenience, the terms shown will be written as: U_0, U_1, U_2, and U_3. Note, there are further terms that can be expanded to. The redefined terms are as follows

$$U_0 = \frac{\mathbf{Q}}{R}$$
$$U_1 = -\frac{\mathbf{Q}_i \mathbf{w}^i}{R^3}$$
$$U_2 = -\frac{\mathbf{Q}_{ij} \mathbf{r}^{ij}}{2R^3} + \frac{3\mathbf{Q}_{ij} \mathbf{w}^i \mathbf{w}^j}{2R^5}$$
$$U_3 = \frac{3\mathbf{Q}_{ijk} \mathbf{r}^{ij} \mathbf{w}^k}{2R^5} - \frac{5\mathbf{Q}_{ijk} \mathbf{w}^i \mathbf{w}^j \mathbf{w}^k}{2R^7}$$

Through this formulation, it seems that, if there was to be a cavity within the polyhedron or a non-convex shape, the model would still assume the cavity or empty space to have a density. This would cause for a "double count" of mass from that location and would result in faulty gravitation and torque from and on one or both bodies.

5.3.2.5 Mutual Force, Mutual Torque, and Perturbations

Since the mutual potential using tetrahedrons is defined, formulating the equations for mutual forces and torques must be completed. This is done by differentiating the mutual potential, Equation 5.33, by the relative position and separately by each bodies' orientation transformation matrix. Doing so will result in the mutual force and mutual torque, respectively. The formulations below will be for the inertial reference frame and are taken from [21].

5.3.2.5.1 Force Components By definition, a force can be determined by differentiating the potential by its position. This can be seen in simple 2-body dynamics. Here, however, these equations take a different form due to the Einstein notation. The forces for bodies A and B can be found as follows

$$\mathbf{F}_\theta^A = \frac{\partial U}{\partial \mathbf{A}_\theta} = -\mathbf{F}_\theta^B = -\frac{\partial U}{\partial \mathbf{B}_\theta} \tag{5.34}$$

From inspecting Equation 5.33, it can be seen that there are a few useful simplifications that can be made when differentiating. These take the form of

$$\begin{aligned}\frac{\partial R}{\partial \mathbf{A}_\theta} = \frac{\partial \sqrt{\mathbf{R}^j \mathbf{R}_j}}{\partial \mathbf{A}_\theta} = \frac{1}{2\sqrt{\mathbf{R}^j \mathbf{R}_j}} \frac{\partial \left(\mathbf{R}^j \mathbf{R}_j\right)}{\partial \mathbf{A}_\theta} = \frac{1}{2R}\left(\frac{\partial \mathbf{R}^j}{\partial \mathbf{A}_\theta}\mathbf{R}_j + \mathbf{R}^j \frac{\partial \mathbf{R}_j}{\partial \mathbf{A}_\theta}\right) \\ = \frac{1}{2R}\left(-2\delta^j_\theta \mathbf{R}_j\right) = -\frac{\mathbf{R}_\theta}{R}\end{aligned} \tag{5.35}$$

$$\frac{\partial \mathbf{w}^i}{\partial \mathbf{A}_\theta} = \frac{\partial \left(\mathbf{R}^j \mathbf{v}^i_j\right)}{\partial \mathbf{A}_\theta} = \frac{\partial \mathbf{R}^j}{\partial \mathbf{A}_\theta}\mathbf{v}^i_j = -\delta^j_\theta \mathbf{v}^i_j = -\mathbf{v}^i_\theta \tag{5.36}$$

where the Kronecker delta function, δ^j_θ, is 1 when $i = \theta$ and 0 elsewhere. With these simplifications, the components of Equation 5.33 can be differentiated with respect to $\mathbf{A}_\theta$.

$$\frac{\partial U_0}{\partial \mathbf{A}_\theta} = \frac{\partial}{\partial \mathbf{A}_\theta}\left(\frac{\mathbf{Q}}{R}\right) = -\frac{\mathbf{Q}}{R^2}\frac{\partial R}{\partial \mathbf{A}_\theta} = \frac{\mathbf{Q}\mathbf{R}_\theta}{R^3} \tag{5.37}$$

$$\frac{\partial U_1}{\partial \mathbf{A}_\theta} = \frac{\partial}{\partial \mathbf{A}_\theta}\left(-\frac{\mathbf{Q}_i \mathbf{w}^i}{R^3}\right) = \frac{3\mathbf{Q}_i}{R^4}\frac{\partial R}{\partial \mathbf{A}_\theta}\mathbf{w}^i - \frac{\mathbf{Q}_i}{R^3}\frac{\partial \mathbf{w}_i}{\partial \mathbf{A}_\theta} = \frac{\mathbf{Q}_i \mathbf{v}^i_\theta}{R^3} - \frac{3\mathbf{Q}_i \mathbf{R}_\theta \mathbf{w}^i}{R^5} \tag{5.38}$$

$$\begin{aligned}\frac{\partial U_2}{\partial \mathbf{A}_\theta} &= \frac{\partial}{\partial \mathbf{A}_\theta}\left(-\frac{\mathbf{Q}_{ij}\mathbf{r}^{ij}}{2R^3} + \frac{3\mathbf{Q}_{ij}\mathbf{w}^i\mathbf{w}^j}{2R^5}\right) \\ &= \frac{3\mathbf{Q}_{ij}\mathbf{r}^{ij}}{2R^4}\frac{\partial R}{\partial \mathbf{A}_\theta} - \frac{15\mathbf{Q}_{ij}\mathbf{w}^i\mathbf{w}^j}{2R^6}\frac{\partial R}{\partial \mathbf{A}_\theta} + \frac{3\mathbf{Q}_{ij}\mathbf{w}^j}{2R^5}\frac{\partial \mathbf{w}^i}{\partial \mathbf{A}_\theta} + \frac{3\mathbf{Q}_{ij}\mathbf{w}^i}{2R^5}\frac{\partial \mathbf{w}^j}{\partial \mathbf{A}_\theta} \\ &= \frac{15\mathbf{Q}_{ij}\mathbf{w}^i\mathbf{w}^j\mathbf{R}_\theta}{2R^7} - \frac{3\mathbf{Q}_{ij}\mathbf{r}^{ij}\mathbf{R}_\theta}{2R^5} - \frac{3\mathbf{Q}_{ij}\mathbf{w}^i\mathbf{v}^j_\theta}{R^5}\end{aligned} \tag{5.39}$$

$$\begin{aligned}\frac{\partial U_3}{\partial \mathbf{A}_\theta} &= \frac{\partial}{\partial \mathbf{A}_\theta}\left(\frac{3\mathbf{Q}_{ijk}\mathbf{r}^{ij}\mathbf{w}^k}{2R^5} - \frac{5\mathbf{Q}_{ijk}\mathbf{w}^i\mathbf{w}^j\mathbf{w}^k}{2R^7}\right) \\ &= -\frac{15\mathbf{Q}_{ijk}\mathbf{r}^{ij}\mathbf{w}^k}{2R^6}\frac{\partial R}{\partial \mathbf{A}_\theta} + \frac{3\mathbf{Q}_{ijk}\mathbf{r}^{ij}}{2R^5}\frac{\partial \mathbf{w}^k}{\partial \mathbf{A}_\theta} + \frac{35\mathbf{Q}_{ijk}\mathbf{w}^i\mathbf{w}^j\mathbf{w}^k}{2R^8}\frac{\partial R}{\partial \mathbf{A}_\theta} - \frac{5\mathbf{Q}_{ijk}\mathbf{w}^j\mathbf{w}^k}{2R^7}\frac{\partial \mathbf{w}^i}{\partial \mathbf{A}_\theta} \\ &\quad - \frac{5\mathbf{Q}_{ijk}\mathbf{w}^i\mathbf{w}^k}{2R^7}\frac{\partial \mathbf{w}^j}{\partial \mathbf{A}_\theta} - \frac{5\mathbf{Q}_{ijk}\mathbf{w}^i\mathbf{w}^j}{2R^7}\frac{\partial \mathbf{w}^k}{\partial \mathbf{A}_\theta} \\ &= \frac{15\mathbf{Q}_{ijk}\mathbf{r}^{ij}\mathbf{w}^k\mathbf{R}_\theta}{2R^7} + \frac{15\mathbf{Q}_{ijk}\mathbf{w}^i\mathbf{w}^j\mathbf{v}^k_\theta}{2R^7} - \frac{3\mathbf{Q}_{ijk}\mathbf{r}^{ij}\mathbf{v}^k_\theta}{2R^5} - \frac{35\mathbf{Q}_{ijk}\mathbf{w}^i\mathbf{w}^j\mathbf{w}^k\mathbf{R}_\theta}{2R^9}\end{aligned} \tag{5.40}$$

The forces experienced by both bodies are then the summation of the partial derivatives for the mutual potential, which is given by

$$\mathbf{F}_{\theta}^{A} = -\mathbf{F}_{\theta}^{B} = G \sum_{a \epsilon A} \sum_{b \epsilon B} C_{a,b} \ \rho_a T_a \rho_b T_b \left(\frac{\partial U_0}{\partial \mathbf{A}_{\theta}} + \frac{\partial U_1}{\partial \mathbf{A}_{\theta}} + \frac{\partial U_2}{\partial \mathbf{A}_{\theta}} + \frac{\partial U_3}{\partial \mathbf{A}_{\theta}} + ... \right) \tag{5.41}$$

where $C_{a,b}$ is

$$C_{a,b} = \begin{cases} \text{sgn}(\hat{n}_a \cdot \vec{r}_a) \cdot \text{sgn}(\hat{n}_b \cdot \vec{r}_b), & \text{for } (\text{sgn}(\hat{n}_a \cdot \vec{r}_a) + \text{sgn}(\hat{n}_b \cdot \vec{r}_b)) > -2 \\ 0, & \text{for } (\text{sgn}(\hat{n}_a \cdot \vec{r}_a) + \text{sgn}(\hat{n}_b \cdot \vec{r}_b)) = -2 \end{cases} \tag{5.42}$$

with $\hat{n}_a$ and $\hat{n}_b$ being each face's outward pointing normal vector, and $\vec{r}_a$ as well as $\vec{r}_b$ being the location of each face's centroid. When both signs within the minimum function are negative one, which represents to concave portions being calculated, the coefficient, $C_{a,b}$, is zero. Such reason is due to the force components of the two inward pointing faced tetrahedrons have already been considered by the other two combinations (min(-1,1) and min(1,-1)) by the four face combinations. For example, consider two cross-sections of hollow objects A and B as seen in Figure 5.12. For a set of inward and outward face normal vectors on each body, $f_{a(out)}$, $f_{a(in)}$, $f_{b(out)}$, and $f_{b(in)}$ a face force combination is as follows: $\left(f_{a(out)} f_{b(out)}\right)$, $\left(f_{a(out)}, f_{b(in)}\right)$, $\left(f_{a(in)}, f_{b(out)}\right)$ as well as $\left(f_{a(in)}, f_{b(in)}\right)$. The first combination calculates the force as if both objects are solid; the second subtracts out the force corresponding to the inward facing portion (hollow) of A to that of the outward faces of B (solid); the second subtracts out force components corresponding to the inward facing portion (hollow) of B to that of the outward faces of A (solid); and the fourth combination gives the force of hollow portion of A on the hollow portion of B. This last combination has no force component, since is no mass of A acting on no mass of B. Each polyhedron face pair undergoes this process.

5.3.2.5.2 Torque Components Formulation of the torques caused on each body can be seen from the straightforward implementation of moment equation, which states

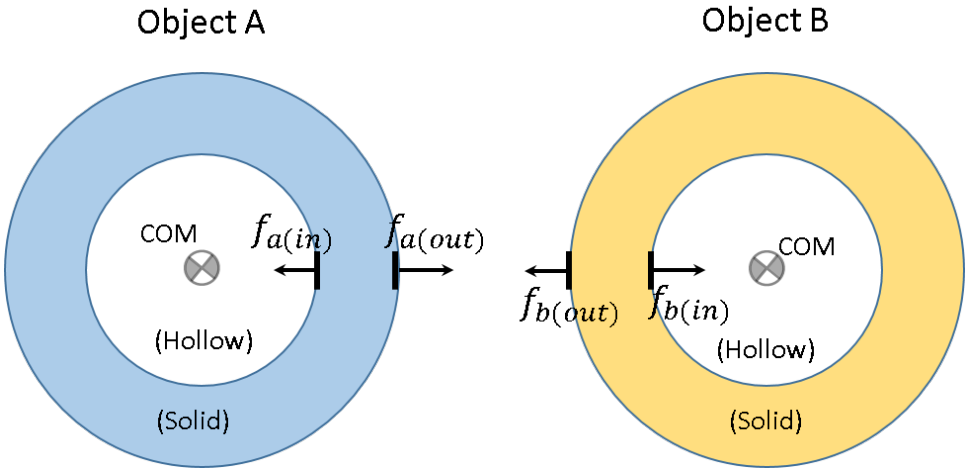

Figure 5.12: Example of a 2 dimensional continuous concave shape which shows a portion represented by inward and outward pointing normal vectors corresponding to faces on each body.

Moment = **vector**×**Force**. However, the orientation and transformation matrices must be defined beforehand. Generally, the torques on each body given in the inertial frame are

$$\mathbf{m}_A = P\mathbf{M}_A$$

and

$$\mathbf{m}_B = S\mathbf{M}_B$$

where P and S are the bodies' rotational transformation matrix from body frame to inertial frame for body A and body B. Furthermore, the transposes of these matrices are defined by

$$P^T = [\alpha_P, \beta_P \gamma_P]$$

and

$$S^T = [\alpha_S, \beta_S \gamma_S]$$

where α, β, and γ are column vectors creating the 3×3 transpose matrix. By applying the definition of moments, the torque on each body from the other is given by the

mutual potential partial differential form. This expression, which is formulated in [95], is as follows

$$\mathbf{M}_A = -\alpha_P \times \frac{\partial U}{\partial \alpha_P} - \beta_P \times \frac{\partial U}{\partial \beta_P} - \gamma_P \times \frac{\partial U}{\partial \gamma_P} \tag{5.43}$$

and

$$\mathbf{M}_B = -\alpha_S \times \frac{\partial U}{\partial \alpha_S} - \beta_S \times \frac{\partial U}{\partial \beta_S} - \gamma_S \times \frac{\partial U}{\partial \gamma_S} \tag{5.44}$$

The partial derivatives are found by differentiating Equation 5.33 by transformation matrix P^T for body A and by S^T for body B. However, some more simplifications can be made when inspecting the mutual potential equation. Recall that for each face on each body, $\mathbf{v}_{ij}$ is defined as

$$\begin{aligned}\mathbf{v}_j^i &\equiv \begin{bmatrix} \Delta x_{a_1}, & \Delta x_{a_2}, & \Delta x_{a_3}, & -\Delta x_{b_1}, & -\Delta x_{b_2}, & -\Delta x_{b_3} \\ \Delta y_{a_1}, & \Delta y_{a_2}, & \Delta y_{a_3}, & -\Delta y_{b_1}, & -\Delta y_{b_2}, & -\Delta y_{b_3} \\ \Delta z_{a_1}, & \Delta z_{a_2}, & \Delta z_{a_3}, & -\Delta z_{b_1}, & -\Delta z_{b_2}, & -\Delta z_{b_3} \end{bmatrix} \\ &= [\Delta \mathbf{r}_{a_1}, \Delta \mathbf{r}_{a_2}, \Delta \mathbf{r}_{a_3}, -\Delta \mathbf{r}_{b_1}, -\Delta \mathbf{r}_{b_2}, -\Delta \mathbf{r}_{b_3}]\end{aligned}$$

which is given in Equation 5.25. Moreover, values within this equation are given in inertial coordinates. Note, i ranges from 1 to 6, while j ranges from 1 to 3. This expression can be rewritten in the form involving P and S as

$$\mathbf{v}_j^i = \left[P\left[\Delta \acute{\mathbf{r}}_{a_1}, \Delta \acute{\mathbf{r}}_{a_2}, \Delta \acute{\mathbf{r}}_{a_3}\right], S\left[-\Delta \acute{\mathbf{r}}_{b_1}, -\Delta \acute{\mathbf{r}}_{b_2}, -\Delta \acute{\mathbf{r}}_{b_3}\right]\right] \tag{5.45}$$

where $\Delta \acute{\mathbf{r}}_a$ and $\Delta \acute{\mathbf{r}}_b$ are each triangular face's vertexes in the body frame with respect to the center of mass of the corresponding object. For simplicity, a new matrix is defined, $\mathbf{c}_j^i$. This matrix contains the non-transformed triangular face vertexes for each body, and is written as

$$\mathbf{c}_j^i = [\Delta \acute{\mathbf{r}}_{a_1}, \Delta \acute{\mathbf{r}}_{a_2}, \Delta \acute{\mathbf{r}}_{a_3}, -\Delta \acute{\mathbf{r}}_{b_1}, -\Delta \acute{\mathbf{r}}_{b_2}, -\Delta \acute{\mathbf{r}}_{b_3}] \tag{5.46}$$

By differentiating Equation 5.45 with respect to P^T, the result yields a rank-4 tensor, which is given as

$$\begin{aligned}\frac{\partial \mathbf{v}_j^i}{\partial P_{\theta\phi}^T} &= \frac{\partial}{\partial P_{\theta\phi}^T}\left(\left[P\left[\Delta\acute{\mathbf{r}}_{a_1}, \Delta\acute{\mathbf{r}}_{a_2}, \Delta\acute{\mathbf{r}}_{a_3}\right], S\left[-\Delta\acute{\mathbf{r}}_{b_1}, -\Delta\acute{\mathbf{r}}_{b_2}, -\Delta\acute{\mathbf{r}}_{b_3}\right]\right]\right) \\ &= \left[\frac{\partial P_{jk}}{\partial P_{\theta\phi}^T}\mathbf{c}_k^i, 0_{j\phi}^{\theta i}\right] = \left[\delta_j^\theta \delta_\phi^k \mathbf{c}_k^i, 0_{j\phi}^{\theta i}\right] = \left[\delta_j^\theta \mathbf{c}_\phi^i, 0_{j\phi}^{\theta i}\right] = \mathbf{D}_{j\theta}^{\phi i}(a)\end{aligned} \tag{5.47}$$

where the i index goes from 1 to 6 (accessing i^{th} column of $\mathbf{c}_j^i$), 1 to 3 on the non-zero portion and 4 to 6 on the zero portion, while all ϕ, θ, and j range from 1 to 3. This is done similarly for body B

$$\begin{aligned}\frac{\partial \mathbf{v}_j^i}{\partial S_{\theta\phi}^T} &= \frac{\partial}{\partial S_{\theta\phi}^T}\left(\left[P\left[\Delta\acute{\mathbf{r}}_{a_1}, \Delta\acute{\mathbf{r}}_{a_2}, \Delta\acute{\mathbf{r}}_{a_3}\right], S\left[-\Delta\acute{\mathbf{r}}_{b_1}, -\Delta\acute{\mathbf{r}}_{b_2}, -\Delta\acute{\mathbf{r}}_{b_3}\right]\right]\right) \\ &= \left[0_{j\phi}^{\theta i}, \frac{\partial S_{jk}}{\partial S_{\theta\phi}^T}\mathbf{c}_k^i\right] = \left[0_{j\phi}^{\theta i}, \delta_j^\theta \delta_\phi^k \mathbf{c}_k^i\right] = \left[0_{j\phi}^{\theta i}, \delta_j^\theta \mathbf{c}_\phi^i\right] = \mathbf{D}_{j\theta}^{\phi i}(b)\end{aligned} \tag{5.48}$$

where, in the case of S^T differentiation, i ranges from 1 to 3 on the zero portion and 4 to 6 on the non-zero part. It has been noted by [21] that the assumption of the general partial matrix differential form, $\frac{\partial T_{ik}}{\partial T_{\theta\phi}^T} = \delta_k^\theta \delta_\phi^i$, does not belong to SO$\{3\}$, however is still suitable. Another option is to use a substitution that follows

$$\frac{\partial T_{ik}^T}{\partial T_{\theta\phi}} = \delta_i^\theta \delta_\phi^k - T_{\phi i} T_{k\theta} \tag{5.49}$$

where T is, in general, a 3×3 rotation transformation matrix. This corresponds to either S^T or P^T when considering the differentiation. Doing so will result in a different form of Equations 5.43 and 5.44 as

$$\mathbf{M}_A = \frac{1}{2}\left(-\alpha_P \times \frac{\partial U}{\partial \alpha_P} - \beta_P \times \frac{\partial U}{\partial \beta_P} - \gamma_P \times \frac{\partial U}{\partial \gamma_P}\right) \tag{5.50}$$

and

$$\mathbf{M}_B = \frac{1}{2}\left(-\alpha_S \times \frac{\partial U}{\partial \alpha_S} - \beta_S \times \frac{\partial U}{\partial \beta_S} - \gamma_S \times \frac{\partial U}{\partial \gamma_S}\right) \tag{5.51}$$

Due to the formulation of $\mathbf{D}$, the following moment equations can be done for either body A or B by switching which $\mathbf{D}$ is used, $\mathbf{D}^{\phi i}_{j\theta}(a)$ or $\mathbf{D}^{\phi i}_{j\theta}(b)$. With this, two more simplification can be made. These are with the partial differentiation of $\mathbf{w}^i$ and $\mathbf{r}^{ij}$ with respect to any general rotational transformation matrix $T_{\phi\theta}$. The simplifications are written as

$$\frac{\partial \mathbf{w}^i}{\partial T_{\phi\theta}} = \frac{\partial \left(\mathbf{R}^j \mathbf{v}^i_j\right)}{\partial T_{\phi\theta}} = \mathbf{R}^j \frac{\partial \mathbf{v}^i_j}{\partial T_{\phi\theta}} = \mathbf{R}^j \mathbf{D}^{\phi i}_{j\theta} \tag{5.52}$$

and

$$\frac{\partial \mathbf{r}^{ij}}{\partial T_{\phi\theta}} = \frac{\partial \mathbf{v}^i_p \, \mathbf{v}^j_p}{\partial T_{\phi\theta}} = \frac{\partial \mathbf{v}^i_p}{\partial T_{\phi\theta}} \mathbf{v}^j_p + \mathbf{v}^i_p \frac{\partial \mathbf{v}^j_p}{\partial T_{\phi\theta}} = \mathbf{D}^{\phi i}_{p\theta} \mathbf{v}^j_p + \mathbf{v}^i_p \mathbf{D}^{\phi j}_{p\theta} = 2\mathbf{v}^i_p \mathbf{D}^{\phi j}_{p\theta} \tag{5.53}$$

For convenience, only the general form of $\mathbf{D}$ will be used. The following equations, Equations 5.54 through 5.57, are found by differentiating the different components of the mutual potential equation, Equation 5.33, by each body's rotational matrix (inertial to body frame). These partial differentiation forms are given by

$$\frac{\partial U_0}{\partial T_{\phi\theta}} = 0_{\phi\theta} \tag{5.54}$$

$$\frac{\partial U_1}{\partial T_{\phi\theta}} = \frac{\partial}{\partial T_{\phi\theta}} \left(-\frac{\mathbf{Q}_i \mathbf{w}^i}{R^3} \right) = -\frac{\mathbf{Q}_i}{R^3} \frac{\partial \mathbf{w}^i}{\partial T_{\phi\theta}} = -\frac{\mathbf{Q}_i \mathbf{R}^j \mathbf{D}^{\phi i}_{j\theta}}{R^3} \tag{5.55}$$

$$\begin{aligned}
\frac{\partial U_2}{\partial T_{\phi\theta}} &= \frac{\partial}{\partial T_{\phi\theta}} \left(-\frac{\mathbf{Q}_{ij} \mathbf{r}^{ij}}{2R^3} + \frac{3\mathbf{Q}_{ij} \mathbf{w}^i \mathbf{w}^j}{2R^5} \right) \\
&= -\frac{\mathbf{Q}_{ij}}{2R^3} \frac{\partial \mathbf{r}^{ij}}{\partial T_{\phi\theta}} + \frac{3\mathbf{Q}_{ij}}{2R^5} \frac{\partial \mathbf{w}^i \mathbf{w}^j}{\partial T_{\phi\theta}} \\
&= -\frac{\mathbf{Q}_{ij} \mathbf{v}^i_p \mathbf{D}^{\phi j}_{p\theta}}{R^3} + \frac{3\mathbf{Q}_{ij}}{2R^5} \left(\frac{\partial \mathbf{w}^i}{\partial T_{\phi\theta}} \mathbf{w}^j + \mathbf{w}^i \frac{\partial \mathbf{w}^j}{\partial T_{\phi\theta}} \right) \\
&= -\frac{\mathbf{Q}_{ij} \mathbf{v}^i_p \mathbf{D}^{\phi j}_{p\theta}}{R^3} + \frac{3\mathbf{Q}_{ij}}{2R^5} \left(\mathbf{R}^p \mathbf{D}^{\phi i}_{p\theta} \mathbf{w}^j + \mathbf{w}^i \mathbf{R}^p \mathbf{D}^{\phi j}_{p\theta} \right) \\
&= -\frac{\mathbf{Q}_{ij} \mathbf{v}^i_p \mathbf{D}^{\phi j}_{p\theta}}{R^3} + \frac{3\mathbf{Q}_{ij} \mathbf{w}^i \mathbf{R}^p \mathbf{D}^{\phi j}_{p\theta}}{R^5}
\end{aligned} \tag{5.56}$$

$$\begin{aligned}
\frac{\partial U_3}{\partial T_{\phi\theta}} &= \frac{\partial}{\partial T_{\phi\theta}}\left(\frac{3\mathbf{Q}_{ijk}\mathbf{r}^{ij}\mathbf{w}^k}{2R^5}-\frac{5\mathbf{Q}_{ijk}\mathbf{w}^i\mathbf{w}^j\mathbf{w}^k}{2R^7}\right)\\
&= \frac{3\mathbf{Q}_{ijk}}{2R^5}\left(\frac{\partial \mathbf{r}^{ij}}{\partial T_{\phi\theta}}\mathbf{w}^k+\mathbf{r}^{ij}\frac{\partial \mathbf{w}^k}{\partial T_{\phi\theta}}\right)\\
&\quad -\frac{5\mathbf{Q}_{ijk}}{2R^7}\left(\frac{\partial \mathbf{w}^i}{\partial T_{\phi\theta}}\mathbf{w}^j\mathbf{w}^k+\mathbf{w}^i\frac{\partial \mathbf{w}^j}{\partial T_{\phi\theta}}\mathbf{w}^k+\mathbf{w}^i\mathbf{w}^j\frac{\partial \mathbf{w}^k}{\partial T_{\phi\theta}}\right)\\
&= \frac{3\mathbf{Q}_{ijk}}{2R^5}\left(2\mathbf{v}_p^i\mathbf{D}_{p\theta}^{\phi j}\mathbf{w}^k+\mathbf{r}^{ij}\mathbf{R}^p\mathbf{D}_{p\theta}^{\phi k}\right)\\
&\quad -\frac{5\mathbf{Q}_{ijk}}{2R^7}\left(\mathbf{R}^p\mathbf{D}_{p\theta}^{\phi i}\mathbf{w}^j\mathbf{w}^k+\mathbf{w}^i\mathbf{R}^p\mathbf{D}_{p\theta}^{\phi j}\mathbf{w}^k+\mathbf{w}^i\mathbf{w}^j\mathbf{R}^p\mathbf{D}_{p\theta}^{\phi k}\right)\\
&= \frac{3\mathbf{Q}_{ijk}}{2R^5}\left(2\mathbf{v}_p^i\mathbf{D}_{p\theta}^{\phi j}\mathbf{w}^k+\mathbf{r}^{ij}\mathbf{R}^p\mathbf{D}_{p\theta}^{\phi k}\right)-\frac{15\mathbf{Q}_{ijk}\mathbf{w}^i\mathbf{w}^j\mathbf{R}^p\mathbf{D}_{p\theta}^{\phi k}}{2R^7}
\end{aligned} \tag{5.57}$$

Refer to [21] for further details about higher order expansion terms and sequencing of different combinations. If this is not desired, Equation 5.33 can be expanded to further terms using the Legendre polynomials of Figure 5.8. With the derivatives constructed, the partial derivative matrix is written as the summation over both bodies

$$\mathbf{E}_{\phi\theta} = G\sum_{a\epsilon A}\sum_{b\epsilon B} C_{a,b}\ \rho_a T_a \rho_b T_b\left(\frac{\partial U_0}{\partial T_{\phi\theta}}+\frac{\partial U_1}{\partial T_{\phi\theta}}+\frac{\partial U_2}{\partial T_{\phi\theta}}+\frac{\partial U_3}{\partial T_{\phi\theta}}+....\right) = \begin{bmatrix}E^\alpha & E^\beta & E^\gamma\end{bmatrix} \tag{5.58}$$

Each body will have a different summation for $E_{\phi\theta}$ due to the fourth order tensor, D. Using the form of Equation 5.43 and 5.44, the torques in each body frame are given as

$$\mathbf{M}_A = -\alpha_P\times E^\alpha-\beta_P\times E^\beta-\gamma_P\times E^\gamma \tag{5.59}$$

where $\mathbf{D}_{j\theta}^{\phi i}(a)$ was used and

$$\mathbf{M}_B = -\alpha_S\times E^\alpha-\beta_S\times E^\beta-\gamma_S\times E^\gamma \tag{5.60}$$

where $\mathbf{D}_{j\theta}^{\phi i}(b)$ was used. However, in the case of using the definition for the matrix partial differentiation as seen in Equation 5.49, the torques on each body can be written as

$$\mathbf{M}_A = \frac{1}{2}\left(-\alpha_P\times E^\alpha-\beta_P\times E^\beta-\gamma_P\times E^\gamma\right) \tag{5.61}$$

$$\mathbf{M}_B = \frac{1}{2}\left(-\alpha_S \times E^{\alpha} - \beta_S \times E^{\beta} - \gamma_S \times E^{\gamma}\right) \tag{5.62}$$

where the correct **D** tensor is used corresponding to each body.

5.3.2.6 Solar Radiation Pressure

Solar radiation, from an illuminating source, causes an outward force opposing the gravitational force caused by the source and orbiting body. This is due to photons being emitted from the source outward to the body of question. These photons are absorbed, reflected, and transmitted through the body. It has been shown in [102] that a "cannonball" representation, or LAGEOS model, of an orbiting body can be used. However, when dealing with irregular shaped bodies, it would be wise to incorporate such shapes into the solar radiation pressure force model. Since polyhedrons are being used, each face can represent a surface and hence a formulation incorporating reflection, absorption, and transmittance can be implemented.

5.3.2.6.1 Solar Radiation Pressure Force In [103] a formulation of solar radiation pressure was found for using the faces of a polyhedron. This formula includes the power density from the sun at the object, which is given in [104] as

$$W = \frac{\sigma R_s^2 T_s^4}{||\mathbf{r}_{obj}||_2} \tag{5.63}$$

where $\sigma = 5.6704 \cdot 10^{-8} (\mathrm{W/m^2/K^4})$ is the Stefan-Boltzmann constant, R_s is the radius of the sun, T_s is the surface temperature of the sun, and $||\mathbf{r}_{obj}||_2$ is the distance from the sun to the orbiting body. Note, this form is derived from the definition of existence and a Lambertian source, which is found in [104] and Chapter 24 of [105]. The pressure can then be described as

$$P(R) = \frac{W}{c} \tag{5.64}$$

where c is the speed of light and W is as defined in Equation 5.63. The force from solar radiation is then given by

$$\mathbf{F}_{SRP} = -P(R)\sum_{k=1}^{n} A_k \cos(\theta_k)\left[(1-s_k)\,\hat{\mathbf{u}} + 2\left(\frac{\rho_k}{3} + s_k\cos(\theta_k)\right)\hat{\mathbf{n}}_k\right] \tag{5.65}$$

where n is the number of faces illuminated by the sun, A_k is each triangular face's area, $\hat{\mathbf{n}}_k$ is the k^{th} face's outward pointing normal vector, $\hat{\mathbf{u}}$ is the unit vector from the body to the sun, θ_k is the angle between $\hat{\mathbf{n}}_k$ and $\hat{\mathbf{u}}$, s_k is the body's specular reflection coefficient, and ρ_k is the body's diffuse reflection coefficient. For simplicity, it is recommended that the computations are calculated in the inertial frame. The last two variables, s_k and ρ_k, must follow

$$a_k + s_k + \rho_k = 1 \tag{5.66}$$

where a_k is the absorption coefficient. Similar expressions can be found in [106], where it is implemented for the dynamics of a solar sail. A condensed form, which will be needed for torque calculations, is given by

$$\mathbf{F}_{SRP} = -P(R)\sum_{k=1}^{n} \mathbf{f}_k \tag{5.67}$$

where $\mathbf{f}_k$ represents the force on each face. However, this solar radiation pressure force model does not take into account self reflection, which would need a more sophisticated ray-trace algorithm.

5.3.2.6.2 Solar Radiation Pressure Torque Since the force on each face caused by the sun's photons has been calculated, the torque on each face can be found. This is done by using, once again, the general form moments, **Moment** = **vector**×**Force**. Each face of each body must undergo this definition, which can calculated by

$$\mathbf{M}_{SRP} = -\frac{P(R)}{3} T_{B/I} \sum_{k=1}^{n} \mathbf{p}_k \times \mathbf{f}_k \tag{5.68}$$

where n is the number of faces, $T_{B/I}$ is inertial to body frame transformation matrix, and $\mathbf{p}_k$ is the k$^{\text{th}}$ face's center point. The center point is found by

$$\mathbf{p}_k = \frac{1}{3}\sum_{j=1}^{3} \Delta\mathbf{r}_j^k \tag{5.69}$$

where k represents the k$^{\text{th}}$ face, $\Delta\mathbf{r}$ corresponds to a single body's triangular face vertex, and j represents each triangular face vertex index. The center point of each face must be found for each body and for each face.

5.3.2.7 Solar Tidal Force

The tidal force occurs when there is stretching or elongation parallel to the sun-to-object vector and contraction or shorten perpendicular to the same vector. This same phenomenon is the cause for ocean tides, which are brought forth by the moon. Consequently, this force represents a separation effect in the object. An approximation for this force found in [107] is given by

$$F_{Tidal} = \frac{2GMmr}{||\mathbf{f_{obj}}||_{\mathbf{2}}^{\mathbf{3}}} \tag{5.70}$$

where M is the mass of the sun, m is the mass of the object, and r is the diameter of the object. It has been noted by [108] that this force, along with tidal torque, is usually not taken into account when using rigid-body polyhedron approximations. This is due to non-deforming bodies and shape preservation, which is already assumed in rigid body dynamics.

5.3.3 Lie Group Variational Integrator (LGVI)

The LGVI is used in [109] due to "desirable properties such as symplecticity, momentum preservation, and good energy stability for exponentially long time periods, while simultaneously preserving the Euclidean Lie group structure." This integrator uses a

discrete formulation of the equations of motion, which are based off the previous step as well as numerical estimation of the rigid body's rotational transformation matrix. Further detail of this integrator can be found in [109] and [110].

5.3.3.1 Equations of Motion

The discrete equations of motion in the inertial frame, found in [109] need predefined information for initial conditions. These would include

$$\gamma_{i_0} = m_i \mathbf{v}_{i_0} \tag{5.71}$$

$$\mathbf{\Pi}_{i_0} = J_i \omega_{i_0} \tag{5.72}$$

$$J_{d_i} = \frac{1}{2}\mathrm{tr}\left[J_i\right] I_{3\times 3} - J_i \tag{5.73}$$

where i represents the body number (A is 1, B is 2,....,n), γ is the linear momentum vector, $\mathbf{v}$ is the object's inertial velocity vector in m/s, $\mathbf{\Pi}$ is the angular momentum vector, J_i is the 3×3 inertia matrix (will later be diagonalized), ω is the angular rate in rad/s, J_d is the nonstandard moment of inertia matrix, $\mathrm{tr}\left[J_i\right]$ is the trace of the moment of inertia matrix, and $I_{3\times 3}$ is the identity matrix. The equations of motion are then

$$\mathbf{x}_{i_{k+1}} = \mathbf{x}_{i_k} + \frac{h}{m_i}\gamma_{i_k} + \frac{h^2}{2m_i}\mathbf{f}_{i_k} \tag{5.74}$$

$$\gamma_{i_{k+1}} = \gamma_{i_k} + \frac{h}{2}\mathbf{f}_{i_k} + \frac{h}{2}\mathbf{f}_{i_{k+1}} \tag{5.75}$$

$$hS\left(\mathbf{\Pi}_{i_k} + \frac{1}{2}\mathbf{M}_{i_k}\right) = F_{i_k} J_{d_i} - J_{d_i} F_{i_k}^T \tag{5.76}$$

$$\mathbf{\Pi}_{i_{k+1}} = F_{i_k}^T \mathbf{\Pi}_{i_k} + \frac{h}{2} F_{i_k}^T \mathbf{M}_{i_k} + \frac{h}{2}\mathbf{M}_{i_{k+1}} \tag{5.77}$$

$$R_{i_{k+1}} = R_{i_k} F_{i_k} \tag{5.78}$$

where k is the current step, $\mathbf{x}$ is the state, $\mathbf{f}$ is the force, h is the time step in seconds, $\mathbf{M}$ is the moment on the body, $S()$ is the skew-symmetric function of a vector, R is the rotational transformation matrix, and F is the time step rotational transformation matrix. This must be done for each body A and B. At every time step, the partial differentiation of the potential is completed. Higher orders for the potential approximation will increase the simulation time due to more nested loops.

5.3.3.2 Determining Time Step Rotational Transformation Matrix

Equation 5.76 is in the form of the Moser–Veselov equation, which can be approximated numerically and was further studied in [111]. The following approach solves Equation 5.76 numerically due to its Lyapunov-like equation

$$FJ_d - J_d F^T = S(\mathbf{g}) \tag{5.79}$$

In [109] and [110] this form was solved using an exponential map, which could be written by using Rodrigues' formula as

$$F = \exp\left(S(\mathbf{g})\right) = I_{3\times 3} + \frac{\sin\left(||\mathbf{f}||_2\right)}{||\mathbf{f}||_2} S(\mathbf{f}) + \frac{1-\cos\left(||\mathbf{f}||_2\right)}{||\mathbf{f}||_2^2} S(\mathbf{f})^2 \tag{5.80}$$

Equation 5.80 can be substituted into Equation 5.79, which will then yield

$$S(\mathbf{g}) = \frac{\sin\left(||\mathbf{f}||_2\right)}{||\mathbf{f}||_2} S(J\mathbf{f}) + \frac{1-\cos\left(||\mathbf{f}||_2\right)}{||\mathbf{f}||_2^2} S(\mathbf{f}\times J\mathbf{f}) \tag{5.81}$$

This expression can then be written in its equivalent vector form

$$G(\mathbf{f}) = \frac{\sin\left(||\mathbf{f}||_2\right)}{||\mathbf{f}||_2} J\mathbf{f} + \frac{1-\cos\left(||\mathbf{f}||_2\right)}{||\mathbf{f}||_2^2} \mathbf{f}\times J\mathbf{f} \tag{5.82}$$

which then leads to the equation for applying Newton's method. The expression, which is solved iteratively, is

$$\mathbf{f}_{i+1} = \mathbf{f}_i + \nabla G(\mathbf{f_i})^{-1}(\mathbf{g} - G(\mathbf{f}_i)) \tag{5.83}$$

By doing so, Equation 5.83 is iterated until $||\mathbf{f}_i - \mathbf{f}_{i+1}||_2 < \epsilon$, where ϵ is a user defined tolerance and $\nabla G(\mathbf{f})$ is given as

$$\begin{aligned}\nabla G(\mathbf{f}) = &\frac{||\mathbf{f}||_2\cos(||\mathbf{f}||_2) - \sin(||\mathbf{f}||_2)}{||\mathbf{f}||_2^3} J(\mathbf{f}\cdot\mathbf{f}^T) + \frac{\sin(||\mathbf{f}||_2)}{||\mathbf{f}||_2} J \\ &+ \frac{||\mathbf{f}||_2\sin(||\mathbf{f}||_2) - 2(1-\cos(||\mathbf{f}||_2))}{||\mathbf{f}||_2^4} \left[(\mathbf{f}\times J\mathbf{f})\cdot\mathbf{f}^T\right] \\ &+ \frac{1-\cos(||\mathbf{f}||_2)}{||\mathbf{f}||_2^2} \left[-S(J\mathbf{f}) + S(\mathbf{f})J\right]\end{aligned} \tag{5.84}$$

A starting value for $\mathbf{f}_0$ is given in [110], which states that $\mathbf{f}_0 = J^{-1}\mathbf{g}$ or $\mathbf{f}_0$ can be taken from the previous solution. Since the formulation for the F2BP is established, further polyhedron properties must be investigated.

5.3.4 Polyhedron Properties

When a polyhedron shape model is created, it may be done by a variety of ways. The methods for determining a polyhedron's mass, center of mass, and inertia matrix described herein are for triangular faced objects. Constant density of each face's tetrahedron is not required. It has been shown in [112], [113], and [114] that the aforementioned characteristics of a polyhedron may be determined.

FORTRAN code for calculating polyhedron properties can be found in Figures 5.13. This code follows what is formulated in [114]. These steps will not be discussed here. However, further details are in [114]. When using this algorithm, it should be noted that the vertexes for each face must be numbered in a counterclockwise fashion, and the shape must be complex. An alteration has been done so that even complex shapes may be considered as well as pockets of varying density.

Once this is completed for each shape, each body must be shifted by the center of mass location. This insures that the center of mass of the object is at the origin of the coordinate system. After the shift, the inertia matrix should be recalculated. The objects must then be rotated to their Eigen axis, which requires a diagonalization of the inertia matrices.

The diagonalization of an n×n matrix, A, requires the solution to

$$D = V^T A V$$

where the columns of V hold the Eigen vectors. This expression can be solved by applying the Jacobi transformation [115], which also presents code for finding the matrix V. Here, the Eigen vectors correlate to the Jacobi rotations. Matrix V is needed to rotate the polyhedron face vertexes so each object is aligned along the Eigen axis, which requires V^T to be matrix multiplied with each polyhedron vertex. Recall, that this must be done independently for each body.

5.3.5 Application to Didymos Binary System

The Didymos system consists of two bodies, which consists of a smaller body (Didymoon) orbiting the primary body (Didymain). A radar shape model has been generated for Didymain, but not for Didymoon. However, there has been a shape generated for use, which takes the shape of an ellipsoidal tear shape. Simulation results herein are compared with work that is being conducted at JPL. Figure 5.14 shows an in-orbit representation of the Didymos binary system.

```
SUBROUTINE PolyProperties_2(Mass,CM,Ins,indV,indF,Poly_v,Poly_f,D,nf)
  USE omp_lib
  IMPLICIT NONE

  INTEGER, INTENT(IN) :: indV,indF
  INTEGER, INTENT(IN) :: Poly_f(indF,3)
  REAL(8), INTENT(IN) :: Poly_v(indV,3), D
  REAL(8), INTENT(INOUT) :: Mass,Ins(3,3),CM(3), nf(indF,4)

  INTEGER :: i, j, k, face(3)
  REAL(8) :: F0(3),F1(3),F2(3),Vol,DelR(3),fc(3)
  REAL(8) :: P(3,3),a1,a2,b1,b2,c1,c2,d0,d1,d2,dp
  !------------------------------------------------------------------------------
  ! Formulation taken from (Dobrovolkis, Anthony R., "Inertia of Any Polyhedron")
  ! Assumes convex shapes
  ! **************Edited Josh Lyzhoft 2016*******************
  ! Can use non-convex shapes
  ! Uses each triangular face's outward normal pointing vector to determine
  ! if to use negative mass.  This is down by taking the dot product with the face's
  ! center vector and the outward pointing vector.  if the value is greater than
  ! 0, then the mass is positive, equal to 0, zero mass, and less than 0, negative
  ! mass.
  !------------------------------------------------------------------------------

  CM = 0.d0
  mass = 0.d0
  P = 0.d0
  Ins = 0.d0


  !$omp parallel default(none) shared(indF,Poly_f,Poly_v,mass,CM,P,nf), &
  !$omp&  private(Vol,i,j,k,DelR,a1,a2,b1,b2,c1,c2,d0,d1,d2,fc,dp),&
  !$omp& firstprivate(face,F0,F1,F2,D)
    !$omp do schedule(static) reduction(+:P,mass,CM)
    DO i = 1, indF
      ! Obtain vertex location for each face i
      face(1) = Poly_f(i,1), face(2) = Poly_f(i,2), face(3) = Poly_f(i,3)
      F0(1) = Poly_v(face(1),1), F0(2) = Poly_v(face(1),2)
      F0(3) = Poly_v(face(1),3), F1(1) = Poly_v(face(2),1)
      F1(2) = Poly_v(face(2),2), F1(3) = Poly_v(face(2),3)
      F2(1) = Poly_v(face(3),1), F2(2) = Poly_v(face(3),2)
      F2(3) = Poly_v(face(3),3)


      ! Get edges and cross product edges
      a1 = (F1(1)-F0(1));  b1 = (F1(2)-F0(2));  c1 = (F1(3)-F0(3))
      a2 = (F2(1)-F0(1));  b2 = (F2(2)-F0(2));  c2 = (F2(3)-F0(3))
      d0 = (b1*c2-b2*c1);  d1 = (a2*c1-a1*c2);  d2 = (a1*b2-a2*b1)
      ! Outward face normal vectors
      dp = SQRT(d0*d0+d1*d1+d2*d2)
      nf(i,1) = d0/dp;  nf(i,2) = d1/dp;  nf(i,3) = d2/dp

      fc(1) = .3333333333333333d0*(F0(1) + F1(1) + F2(1))
      fc(2) = .3333333333333333d0*(F0(2) + F1(2) + F2(2))
      fc(3) = .3333333333333333d0*(F0(3) + F1(3) + F2(3))

      ! Saving outward pointing normal vector direction
      CALL dotprod(nf(i,1:3),fc,dp)
      IF(dp > 0.d0)THEN
          nf(i,4) = 1.d0
      ELSEIF(dp == 0.d0)THEN
          nf(i,4) = 0.d0
      ELSE
          nf(i,4) = -1.d0
      END IF
      dp = nf(i,4)

      ! Compute Tetrahedron volume
      Vol = (1.d0/6.d0)*abs((F1(2)*F2(3)-F2(2)*F1(3))*F0(1) - &
           & (F2(3)*F0(2)-F2(2)*F0(3))*F1(1) + &
           & (F0(2)*F1(3)-F0(3)*F1(2))*F2(1))
      Mass = Mass + dp*Vol * D

      ! Tetrahedron's Center of Mass
      DelR(1) = 0.25*(F0(1)+F1(1)+F2(1)), DelR(2) = 0.25*(F0(2)+F1(2)+F2(2))
      DelR(3) = 0.25*(F0(3)+F1(3)+F2(3))

      CM(1) = CM(1) + dp*Vol*DelR(1), CM(2) = CM(2) + dp*Vol*DelR(2)
      CM(3) = CM(3) + dp*Vol*DelR(3)

      DO j = 1,3
          DO k = 1,3
              P(j,k) = P(j,k) + dp*(0.05d0*D*Vol)*(2.d0*F0(j)*F0(k) + &
                       & 2.d0*F1(j)*F1(k) + 2.d0*F2(j)*F2(k) + &
                       & F0(j)*F1(k) + F0(k)*F1(j) + F0(j)*F2(k) + &
                       & F0(k)*F2(j) + F1(j)*F2(k) + F1(k)*F2(j))
          END DO
      END DO


    END DO
    !$omp enddo
  !$omp end parallel

  Ins(1,1) = P(2,2) + P(3,3), Ins(2,2) = P(1,1) + P(3,3), Ins(3,3) = P(1,1) + P(2,2)
  Ins(2,3) = -P(2,3), Ins(3,2) = -P(2,3), Ins(1,3) = -P(1,3)
  Ins(3,1) = -P(1,3), Ins(1,2) = -P(1,2), Ins(2,1) = -P(1,2)

  CM = CM/(Mass/D)

  write(*,*)CM

  RETURN
END SUBROUTINE
```

Figure 5.13: Polyhedron property FORTRAN Code. Determines mass, Center of Mass, and inertia matrix.

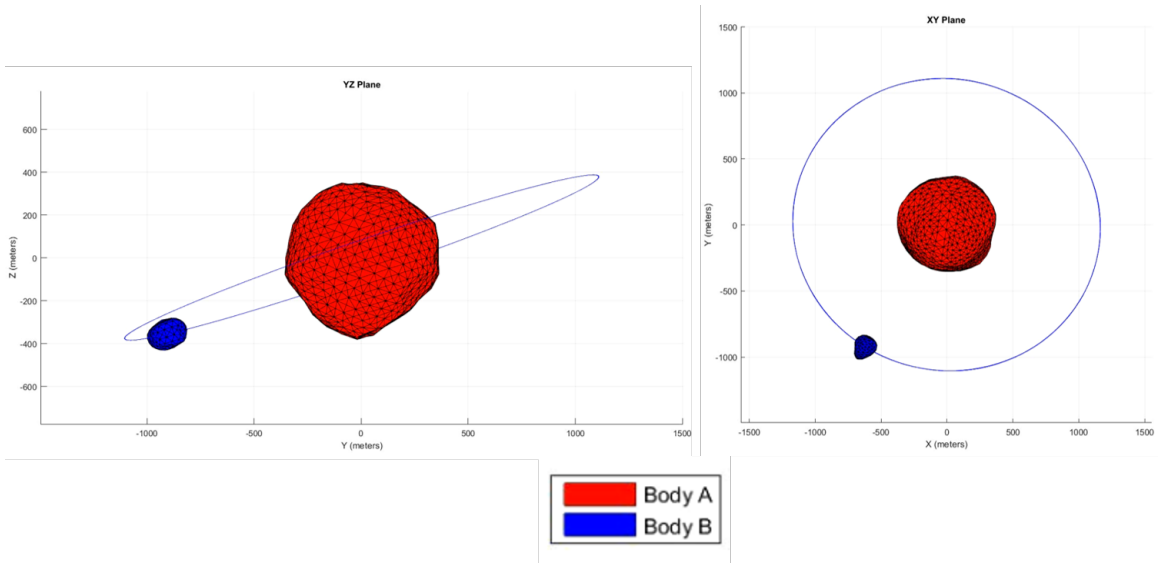

Figure 5.14: Didymos system polyhedron shapes and orbit representation.

Table 5.4: These are the initial conditions given to the Didymos system, Didymain and Didymoon (radar and other shape models).
Note, initial orientation and position manipulation may be needed. This may include re-centering of COM, orienting object along Eigen axis, and Eigen vector direction

asteroid/ Initial Conditions	Didymain (Didymos A)	Didymoon (Didymos B)
Mass (kg)	$5.2294178707036255e11$	$4.8429638900565388e9$
Volume (m^3)	$2.4854815800173700e8$	$2.3018044912530910e6$
Max Radius (m)	427.5185397834427	111.74808546621394
Orientation	$\begin{bmatrix} -0.357348082502793 & -0.931551345940299 & 0.0671895662167409 \\ -0.875890552421066 & 0.359230579402273 & 0.322132163873506 \\ -0.324219197628853 & 0.05626260480216 & -0.944307381730006 \end{bmatrix}$	$\begin{bmatrix} -0.357348082502793 & -0.931551345940299 & 0.0671895662167409 \\ -0.875890552421066 & 0.359230579402273 & 0.322132163873506 \\ -0.324219197628853 & 0.05626260480216 & -0.944307381730006 \end{bmatrix}$
Inert.Matrix (kgm^2)	$\approx \begin{bmatrix} 3.1348425e16 & 0.368129 & -0.419496 \\ 0.368129 & 3.19202483e16 & 7.70503e-2 \\ -0.419496 & 7.70503e-2 & 3.27904162e16 \end{bmatrix}$	$\approx \begin{bmatrix} 1.122145998e13 & -8.517247e-5 & -3.1769855e-4 \\ -8.517247e-5 & 1.4074548e13 & 5.15333e-20 \\ -3.1769855e-4 & 5.15333e-20 & 1.585313898e13 \end{bmatrix}$
COM (m)	$\begin{bmatrix} 1.35893e-15 & -1.99843e-14 & -3.06958e-14 \end{bmatrix}$	$\begin{bmatrix} 5.63076e-15 & 3.28742e-15 & 3.23684e-15 \end{bmatrix}$
X Pos (m)	3.86925948652413	−417.801477866771
Y Pos (m)	9.48388418758507	−1024.06696766927
Z Pos (m)	3.51054970647249	−379.068103495574
X Vel (m/s)	1.47687694130238e−3	−0.159472728787646
Y Vel (m/s)	−5.69522401145143e−4	6.1496857914388e−02
Z Vel (m/s)	−8.91984580904076e−05	9.63162272869109e−03
Body Z axis spin rate (rad/s)	7.72269580528e−4	1.488075e−4

5.3.5.1 Simulation, Results and Comparison

The results presented use a 40 second time step for a 96 hour duration simulated in FORTRAN. Initial conditions for both objects can be found in Table 5.4. Using these conditions in the table, after the 96 hours of simulation time (not actual run time) resulted in a Didymoon max position component difference of approximately -5.71 centimeters and a Didymain max position component difference of -0.529 millimeters. These values were calculated by subtracting the values given by a source at the Jet Propulsion Laboratory (JPL) from the FORTRAN computed simulation values. JPL values are indicated by "Fahnestock," whom of which conducted the analysis. Plots of the radial-transverse-normal (RTN) frame position differences can be found in Figures 5.15 and 5.16.

RTN velocity differences follow a similar trend to the position differences. However, instead of the transverse component seeming to diverge with a linear-like bias, it is the radial component that has this trend. Figures 5.17 and 5.18 show the linear-like trend for Didymain and Didymoon. These plots verify the reasoning of the transverse differences in positions. Since the objects simulated in the FORTRAN code move out radial faster, positive slope, than the JPL code, they must "slowdown" in the transverse direction, hence the negative position difference slope. This is seen in both Didymain and Didymoon. Furthermore, this is due to a transverse difference in the initial forces. These force differences can be seen in Figure 5.19. Further research must be done to determine the cause of the difference.

Similarly, differences for the separation distance between body bodies were calculated. The statistics for the separation distance difference are as follows: average difference is $\approx$ 0.3277 mm and 8.92 mm (1 sigma), root mean square is $\approx$ 8.298 mm, and the minimum and maximum difference values are $\approx$ -20.05 mm and 19.21 mm. An overlay of the separation distances with that of JPL's values can be seen in Figure 5.20. As it can be noticed, the amplitude of the cyclic plot does not match nor does the mean value.

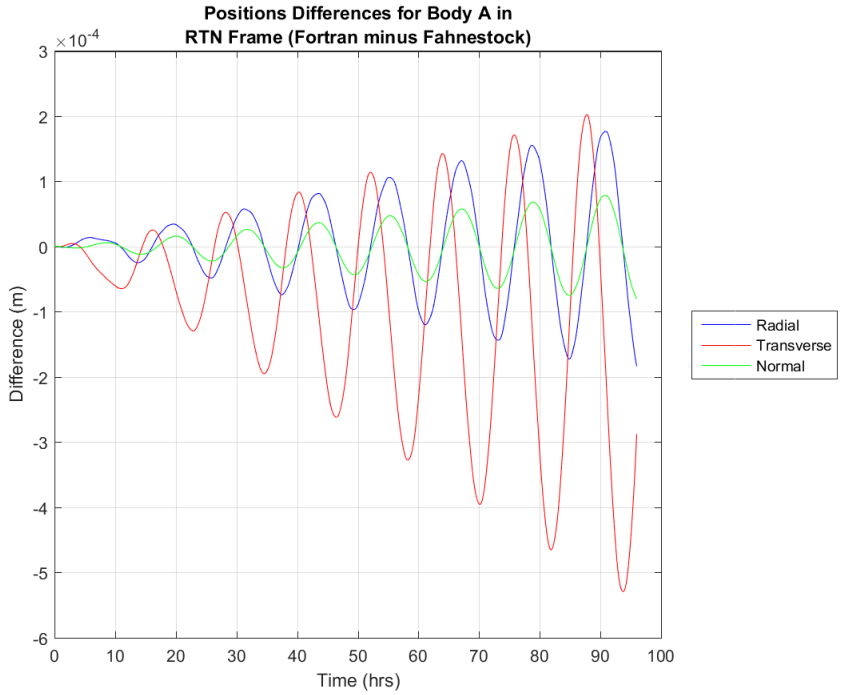

Figure 5.15: RTN frame position difference for Didymain.

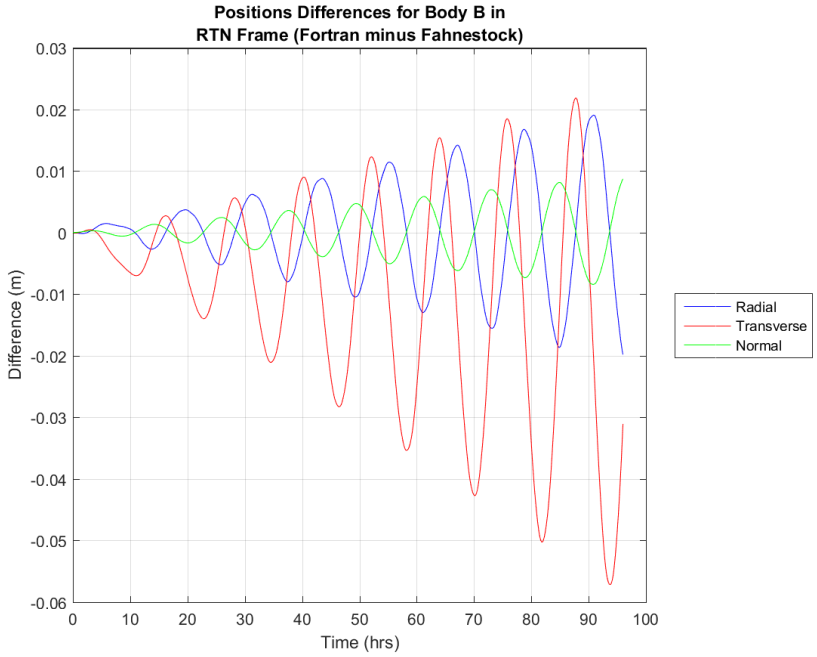

Figure 5.16: RTN frame position difference for Didymoon.

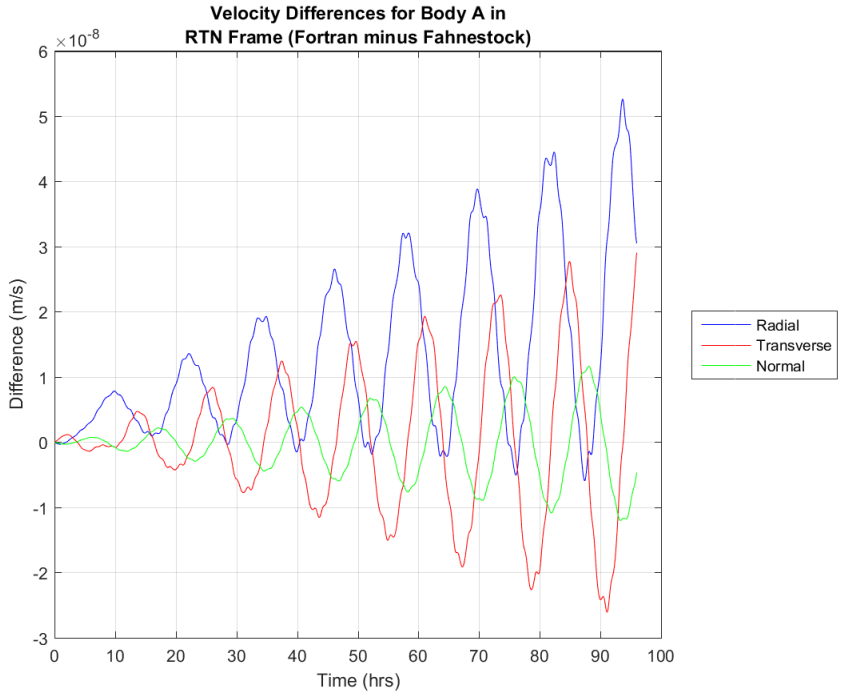

Figure 5.17: RTN frame velocity difference for Didymain.

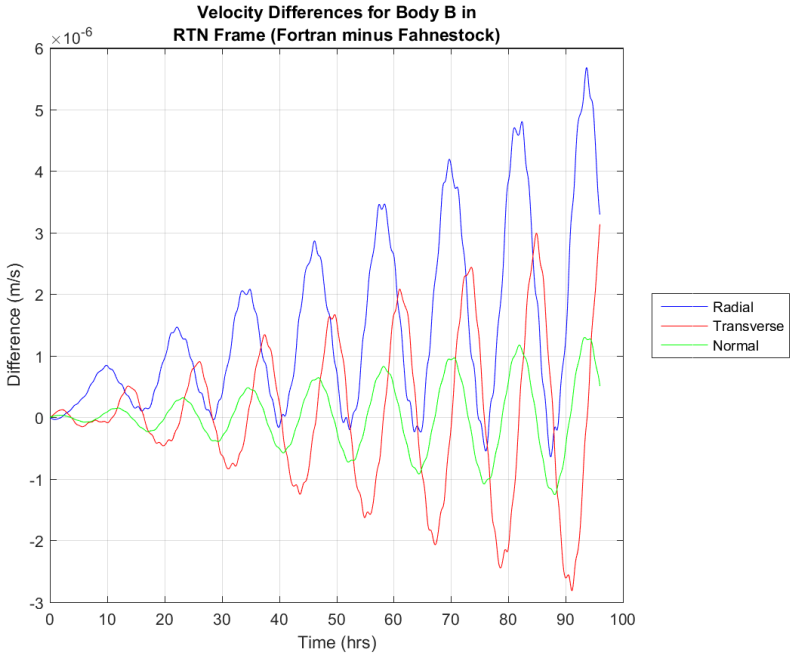

Figure 5.18: RTN frame velocity difference for Didymoon.

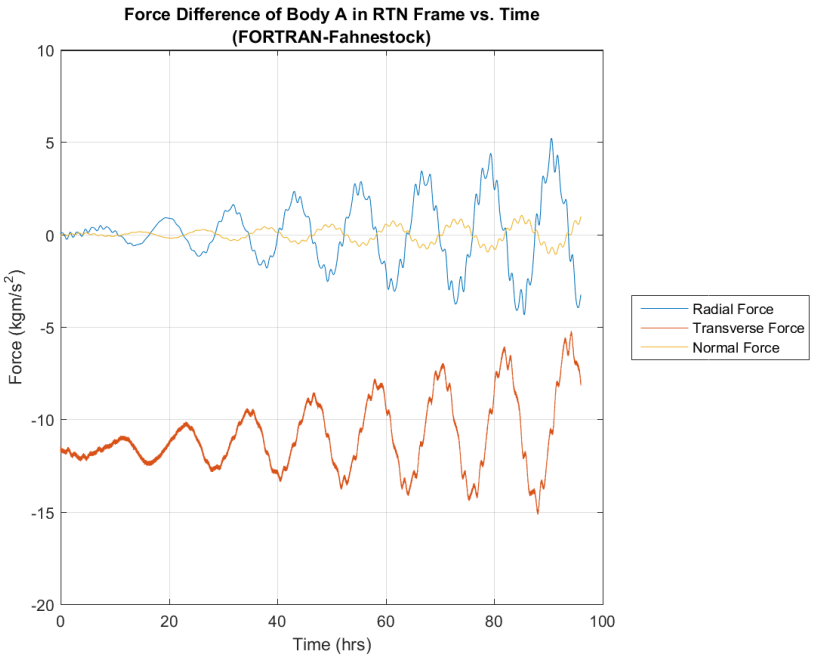

Figure 5.19: RTN frame force differences for Didymain.

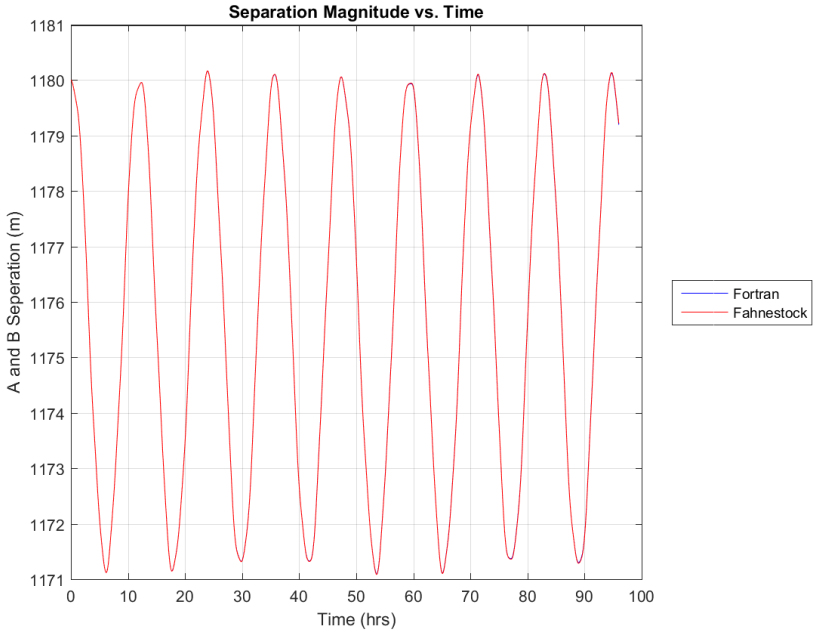

Figure 5.20: Didymoon and Didymain separation distance compared with JPL.

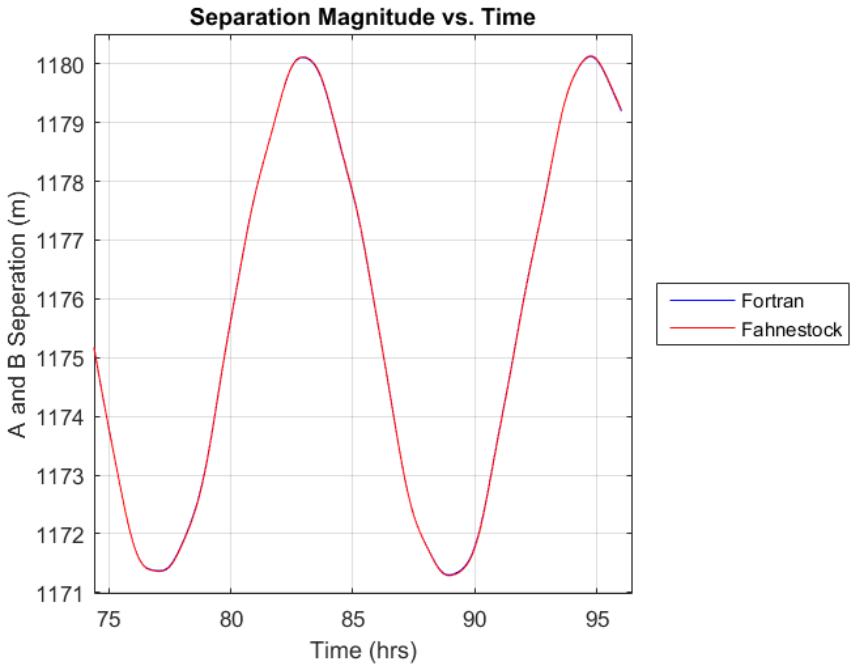

Figure 5.21: Didymoon and Didymain separation distance compared with JPL magnified on the last 20 hours.

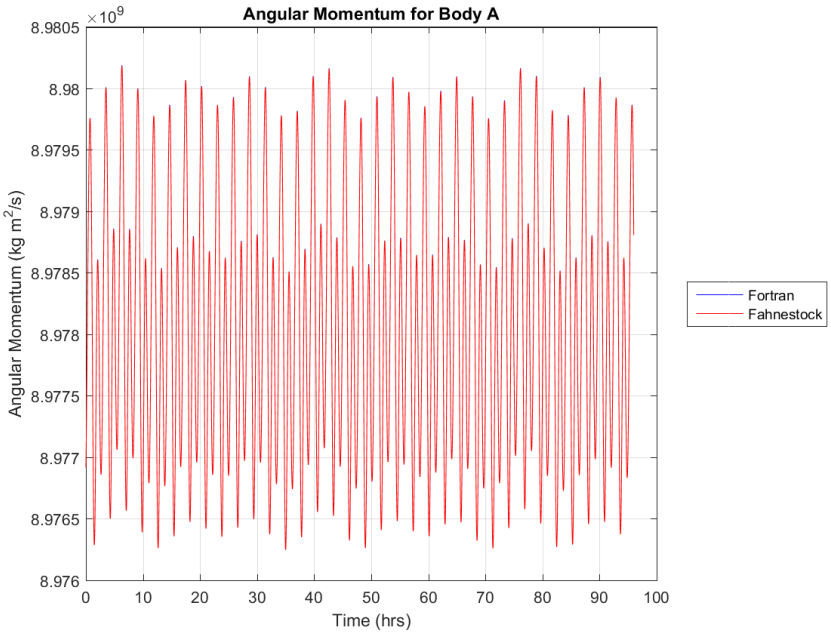

Figure 5.22: Didymoon angular momentum compared with JPL.

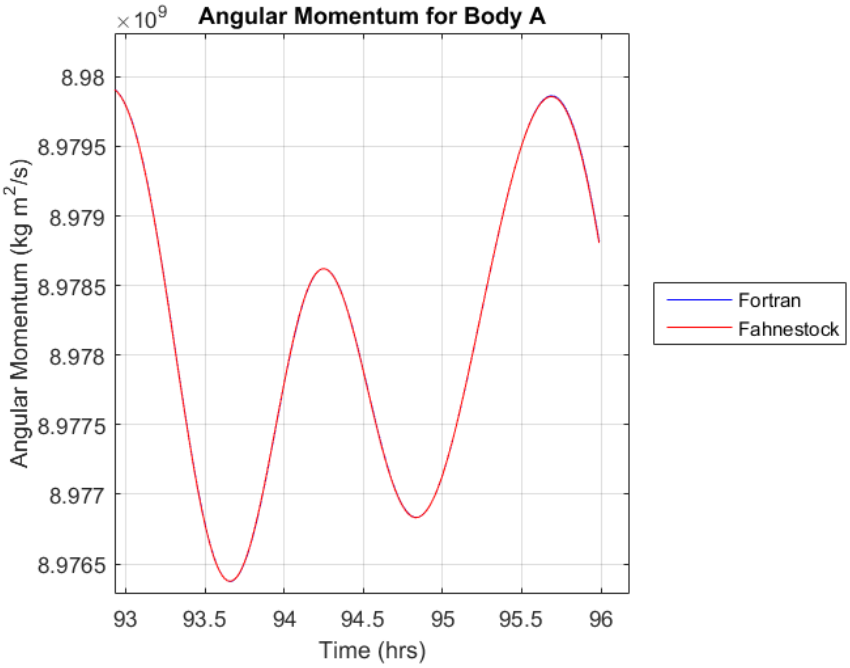

Figure 5.23: Didymoon angular momentum compared with JPL magnified on the last 3 hours.

This indicates a potential bias of the sinusoid. Further confirmation is seen by viewing the peaks and troughs. The peaks of the FORTRAN separation distance, in some cases, are slightly larger than the JPL values. Each trough, however, is noticeably larger than JPL's value. Yet both simulations show that the separation magnitude is bounded. A magnified plot can be seen in Figure 5.21.

To confirm simulation results and conservation of properties, object angular momentum was investigated. For convenience, only the angular momentum for Didymain is plotted. Similar trends are observed in Didymoon. The angular momentum of Didymain is displayed in Figure 5.22. Again, the peaks and troughs do not overlay well with JPL's implementation, much like what was seen for the separation distance. However, the angular momentum is bounded and conserved for at least the 96 hour time frame presented. A magnified plot of the last 3 hours is shown in Figure 5.23. Another area for checking conservative properties was to evaluate the accrued summation of the Frobenius norm associated with the identity matrix subtracted by the rotational trans-

formation matrix, F, matrix multiply with its transpose, $I_{3\times3}-FF^T$. This should, if it is fully conserved, be zero. Over the time period of 96 hours, the accrued summed Frobenius norm associated $I_{3\times3}-FF^T$ was on the order of 10^{-14}.

5.3.6 Future Work

As was discussed in this chapter, the force components differences are not zero for each of the RTN axis. This must be further explored to find the reasoning for the transverse force bias, which may due to not including external forces such as the solar radiation pressure force as well as solar tidal forces. Another desired lane to investigate is to incorporate "pockets" of varying density. A way to remedy this situation is to include a density difference from the rest of the body. If the density is less than the current density for the simplex, the local density, density for the "pocket," will be negative. This subtracts out or adds the difference in the density, hence changing the pocket mass. There is no need for any difference within the current formulation, except ρ_a and ρ_b will be defined as a full vector and not constant as was done for the simulations. By doing so, the density must also be changed to a per simplex bases in the "Polyhedron Properties" subroutine.

5.3.7 Conclusion

All steps needed to formulate the Full-2-Body Problem using polyhedron models have been presented as well as the incorporation of non-convex shapes. Along with these steps, incorporation of the equations of motion, two other external forces and torques, and polyhedron properties have been demonstrated. Simulations using initial conditions given by the JPL have been ran and have shown that results from the FORTRAN code agree with small deviations, which correlate to a maximum position component difference of -5.71 centimeters for Didymoon and -0.529 millimeters for Didymain. The position difference in the transverse direction shows a linear trend, which might not hold for

longer durations of simulation time. However, the summed Frobenius norm associated with $I_{3\times3} - FF^T$ evaluated to a small value, on the order of 10^{-14}, which would indicate that the rotational properties accrued small errors.

REFERENCES

[1] Bland, P.A. and Artemieva, N.A., 2006. The rate of small impacts on Earth. *Meteoritics & Planetary Science*, 41(4), pp.607-631.

[2] Miller, S.D., Straka, W.C., Bachmeier, A.S., Schmit, T.J., Partain, P.T. and Noh, Y.J., 2013. Earth-viewing satellite perspectives on the Chelyabinsk meteor event. *Proceedings of the National Academy of Sciences*, 110(45), pp.18092-18097.

[3] Popova, O.P., Jenniskens, P., Emelyanenko, V., Kartashova, A., Biryukov, E., Khaibrakhmanov, S., Shuvalov, V., Rybnov, Y., Dudorov, A., Grokhovsky, V.I. and Badyukov, D.D., 2013. Chelyabinsk airburst, damage assessment, meteorite recovery, and characterization. Science, 342(6162), pp.1069-1073.

[4] Zhang, Moran,"Russia Meteor 2013: Damage To Top $33 Million; Rescue, Cleanup Team Heads To Meteorite-Hit Urals." *International Business Times*. N.p., 18 Mar. 2013. Web. 22 Jan. 2017. Http://www.facebook.com/moranzhang.

[5] Frimet, Michael J., Jilje M. Roalsvik, and Richard P. Cember. "Commentary — Chelyabinsk: An Insurance Perspective." *SpaceNews.com*. N.p., 15 Dec. 2014. Web. 22 Jan. 2017.

[6] NATIONAL AERONAUTICS AND SPACE ADMINISTRATION (NASA). Jet Propulsion Laboratory. *Deep Impact Launch Press Kit 2005*. N.p., 8 Jan. 2005. Web. 15 Dec. 2016. http://www.jpl.nasa.gov/news/press_kits/deep-impact-launch.pdf.

[7] Europian Space Agency (ESA). *Rosetta End of Mission, Grand Finale Press Kit September 2016. Rosetta.* ESA, 28 Sept. 2016. Web. 18 Dec. 2016 http://sci.esa.int/rosetta/58334-rosetta-end-of-mission-grand-finale-press-kit-september-2016/.

[8] Cheng, A.F., Michel, P., Reed, C., Galvez, A., Carnelli, I. and Headquarters, P., 2012, September. Dart: double asteroid redirection test. In Proceedings of the European Planetary Science Congress, Madrid, Spain.

[9] Hawkins, Matt, et al. *An Innovative Solution to NASAs NEO Impact Threat Mitigation Grand Challenge and Flight Validation Mission Architecture Development.* Technical Report (NNX12AQ60G), 2014.

[10] Vardaxis, G., Sherman, P. and Wie, B., "Impact risk assessment and planetary defense mission planning for asteroid 2015 PDC, *Acta Astronautica*, Vol. 122, pp.307-323 (2016).

[11] Vardaxis, G. and Wie, B., "Near-Earth Object Intercept Trajectory Design for Planetary Defense, *Acta Astronautica*, 101 (2014) 115

[12] Lyzhoft, J., and Wie, B., "Hypervelocity Terminal Guidance of A Multiple Kinetic-Energy Impactor Vehicle (MKIV), AAS 16-411, AAS/AIAA Space Flight Mechanics Meeting, Napa Valley, CA, February 14-18, 2016.

[13] Zimmerman, B. and Wie, B., "A GPU-Accelerated Multiphase Computational Tool for Asteroid Fragmentation/Pulverization Simulation," AAS 16-242, AAS/AIAA Space Flight Mechanics Meeting, Napa Valley, CA, Feb. 15-199, 2016. *AIAA Journal*, Sept. 8, 2016 (online publication date).

[14] Wie, B., Zimmerman, B., Premaratne, P., Lyzhoft, J., and Vardaxis, G., "Non-Nuclear MKIV (Multiple Kinetic Impactor Vehicle) Mission Concept for Pulverizing

Small (50-150 m) Asteroids with Short Warning Times," AAS 15-567, AAS/AIAA Astrodynamics Specialist Conference, Vail, CO, August 9-13, 2015.

[15] Report No. DODIG-2014-111, "Exoatmospheric Kill Vehicle Quality Assurance and Reliability AssessmentPart A, September 08, 2014

[16] Hawkins, Matt, Bong Wie, and Yanning Guo. "Spacecraft guidance algorithms for asteroid intercept and rendezvous missions." *International Journal Aeronautical and Space Sciences* 13.2 (2012): 154-169.

[17] Hawkins, Matt, "New near-optimal feedback guidance algorithms for space missions" (2013). Graduate Theses and Dissertations. 13103. http://lib.dr.iastate.edu/etd/13103

[18] Kaplinger, B., "Physical modeling and high-performance GPU computing for characterization interception, and disruption of hazardous near-Earth objects," Ph.D. Thesis, Iowa State University, 2013

[19] Sitarski, Grzegorz. "Approaches of the parabolic comets to the outer planets." *Acta Astronomica* 18 (1968): 171.

[20] Cheng, A. F., et al. "Asteroid Impact and Deflection Assessment (AIDA) Mission: The double Asteroid redirection test (DART)." (2016).

[21] Fahnestock EG. The full two-body-problem: Simulation, analysis, and application to the dynamics, characteristics, and evolution of binary asteroid systems. ProQuest; 2009.

[22] Bhaskaran, S., 2006. *Autonomous navigation for deep space missions*. Pasadena, CA: Jet Propulsion Laboratory, National Aeronautics and Space Administration.

[23] Janus, John P. *Homing Guidance (A Tutorial Report)*. No. TOR-469 (9990)-1. AEROSPACE CORP EL SEGUNDO CA EL SEGUNDO TECHNICAL OPERATIONS, 1964.

[24] Lynch, Daniel R. *Numerical partial differential equations for environmental scientists and engineers: a first practical course*. Springer Science & Business Media, 2004.

[25] Eberly, David. "Derivative approximation by finite differences." *Magic Software, Inc* (2008).

[26] Jacobson, Mark Z. *Fundamentals of atmospheric modeling*. Cambridge university press, 2005.

[27] Vallado, David A. *Fundamentals of astrodynamics and applications*. Vol. 12. Springer Science & Business Media, 2001.

[28] Lyzhoft, J., Groath, D., and Wie, B., "HYBRID GUIDANCE CONTROL FOR A HYPERVELOCITY SMALL SIZE ASTEROID INTERCEPTOR VEHICLE," (Preprint)AAS 17-270, AAS/AIAA Space Flight Mechanics Meeting, San Antonio, Tx, February 5-9, 2017.

[29] Cockrill, Chris. "Understanding Schmitt Triggers." *Texas Instruments [viitattu 25.2. 2014]. Saatavissa:* http://www.ti.com/lit/an/scea046/scea046.pdf (2011).

[30] Li S, Cui P, Cui H. *Autonomous navigation and guidance for landing on asteroids*. Aerospace science and technology. 2006 Apr 30;10(3):239-47.

[31] Wie, B. "Hypervelocity Nuclear Interceptors for Asteroid Disruption," Acta Astronautica, 90, 2013, pp. 146-155.

[32] Pitz, A., Kaplinger, B., Vardaxis, G., Winkler, T., and Wie, B., "Conceptual Design of a Hypervelocity Asteroid Intercept Vehicle (HAIV) and Its Flight Validation Mission," Acta Astronautica, 94, 2014, pp. 42-56.

[33] Barbee, B., Wie, B., Steiner, M., and Getzandanner, K., "Conceptual Design of a Flight Demonstration Mission for Hypervelocity Asteroid Intercept Vehicle (HAIV)," Acta Astronautica, 106, 2015, pp. 139-159.

[34] Lyzhoft, J., Hawkins, M., Kaplinger, B., and Wie, B., "GPU-Based Optical Navigation and Terminal Guidance Simulation of a Hypervelocity Asteroid Impact Vehicle (HAIV)," AIAA-2013-4966, AIAA Guidance, Navigation, and Control Conference, Boston, MA, August 19-22, 2013.

[35] Cano, Juan L., et al. "Mission analysis for the don quijote phasea study." *Proceedings of the 58th Congress of the International Astronautical Federation, Hyderabad, India.* 2007

[36] Glvez, Andrs, and Ian Carnelli. "ESA Studies on the Don Quijote NEO mission: dealing with impact uncertainties." *Proceedings of the 56th International Astronautical Congress, Fukuoka, Japan.* 2005.

[37] Cheng, A. F., et al. "AIDA: ASTEROID IMPACT & DEFLECTION ASSESSMENT." IAC-1 3-A3.4.8, 64th International Astronautical Congress, Beijing, China, September 23-27, 2013.

[38] Chesley, Steven R., et al. "The ISIS Mission Concept: An Impactor for Surface and Interior Science." IAA-PDC2013-04-01, International Academy of Astronautics Planetary Defense Conference, Flagstaff, Arizona, USA, April 15-19, 2013.

[39] Bhaskaran, Shyam, Joseph E. Riedel, and Stephen P. Synnott. "Autonomous target tracking of small bodies during flybys." (2004).

[40] Kubitschek, D. G., "Impactor Spacecraft Encounter Sequence Design for the Deep Impact Mission," Paper No. GT-SSEC.C.32005, 2005.

[41] Wie, B., Barbee, B., et al., *An Innovative Solution to NASA's Neo Impact Threat Mitigation Grand Challenge and Flight Validation Mission Architecture Development*, NASA Grant and Cooperative Agreement Number: NNX12AQ60G, December 9, 2014. http://www.nasa.gov/sites/default/files/files/Bong_Wi_Final_Report.pdf

[42] Herring, J. et al., *Staring 256 X 256 LWIR Focal Plane Array Performance of the Raytheon Exoatmospheric Kill Vehicle*. Conference Proceedings., 1998. Print.

[43] Sessler, A. M. et al., *Countermeasures: A Technical Evaluation of the Operational Effectiveness of the Planned US National Missile Defense System*. Cambridge: Union of Concerned Scientists MIT Security Studies Program, Apr. 2000.

[44] Wilkening, D., "Making Sense of Ballistic Missile Defense: An Assessment of Concepts and Systems for U.S. Boost-Phase Missile Defense in Comparison to Other Alternatives." American Physical Society Nuclear Workshop, George Washington University, November 1-2, 2013

[45] Lyzhoft, Joshua, John Basart, and Bong Wie. "A new terminal guidance sensor system for asteroid intercept or rendezvous missions." *Acta Astronautica* 119 (2016): 147-159.

[46] Lyzhoft, J., Groath, D., and Wie, B., "Optical and Infrared Sensor Fusion for Hypervelocity Asteroid Intercept Guidance," AAS 14-421, AAS/AIAA Space Flight Mechanics Meeting, Santa Fe, NM, January 26-30, 2014.

[47] "WISE Preliminary Release Explanatory Supplement: WISE Flight System and Operations." *WISE Preliminary Release Explanatory Supplement*. N.p., 12

Apr. 2011. Web. 7 Apr. 2014. http://wise2.ipac.caltech.edu/docs/release/prelim/expsup/sec3_2.html.

[48] Beish, J. D., Cassegrain Telescopes for Amateurs. 3 Dec. 2013.

[49] Shaw, J. A., Reflector Telescopes. Class Lecture, Optical System Design, Montana State University, Bozeman, Febuary 4,2009.

[50] Lockwood, M. E., Cassegrain Formulas and Tips by Mike Lockwood. Lockwood Custom Optics. N.p., n.d. Web. 5 May 2014. http://www.loptics.com/ATM/mirrormaking/cassinfo/cassinfo.html.

[51] Marschner, S., Radiometry. Class Lecture, CS 6630 Spring 2012, Cornell University, Ithaca, January 26, 2012.

[52] Quimby, Richard S. *Photonics and lasers: an introduction.* John Wiley & Sons, 2006.

[53] Lebofsky, L. A. and Spencer, J. R. 1989. Radiometry and thermal modeling of asteroids. In Asteroids II (R. P. Binzel, T. Gehrels, and M. S. Matthews, Eds.), University of Arizona Press, Tucson, 128-147.

[54] Rieke, J. H., *Detection of Light: from the Ultraviolet to the Submillimeter*, 1st ed., Cambridge University Press, New York, 1994, pp. 56

[55] Dunlap, Justin C., et al. "Dark current behavior in DSLR cameras." IS&T/SPIE Electronic Imaging. International Society for Optics and Photonics, 2009.

[56] Porter, William C., et al. "Dark current measurements in a CMOS imager." Electronic Imaging 2008. International Society for Optics and Photonics, 2008.

[57] Ressler, Michael E., et al. "Performance of the JWST/MIRI Si: As detectors." SPIE Astronomical Telescopes+ Instrumentation. International Society for Optics and Photonics, 2008.

[58] Howell, Steve B. *Handbook of CCD astronomy.* Vol. 5. Cambridge University Press, 2006.

[59] Morin, F. J., and J. P. Maita. "Electrical properties of silicon containing arsenic and boron." Physical Review 96.1 (1954): 28.

[60] Budzier, Helmut, and Gerald Gerlach. *Thermal infrared sensors: theory, optimisation and practice.* John Wiley & Sons, 2011.

[61] Bolte, M., "Signal-to-Noise in Optical Astronomy." Class Lecture, Modern Observational Techniques, University of California, Santa Cruz.

[62] Dereniak, E. L., Boreman, G. D., *Infrared Detectors and Systems*, John Wiley & Sons, New York, 1996, Ch. 5.

[63] Hyseni, G., Caka, N., and Hyseni, K., "Infrared thermal detectors parameters: semiconductor bolometers versus pyroelectrics," WSEAS Transactions on circuits and systems, 9(4) (2010), 238-247.

[64] Nemarich, J., *Microbolometer detectors for passive millimeter-wave imaging.* No. ARL-TR-3460. ARMY RESEARCH LAB ADELPHI MD, 2005.

[65] Ryu, H., Kwon, S., Cheon, S., Cho, S. M., Yang, W. S., and Choi, C. A. (2009). "Evaluation of 1/f noise characteristics for Si-based infrared detection materials." ETRI journal, 31(6), 703-708.

[66] Moreno, M., Torres, A., Kosarev, A., and Ambrosio, R., "Un-Cooled microbolometers with amorphous germanium-silicon (a-GexSiy: H) thermo-sensing films." INTECH Open Access Publisher, (2012).

[67] Shaw, Joseph A., "Detectors." Electrical Engineering (EELE) 583 Remote Sensing Systems. Montana State University, Bozeman, Montana. Spring Semester 2012. Class Notes.

[68] Smith, J.C., "Sub-Exposure Times and Signal to Noise Considerations," [Paper], Revised February 3, 2010, Copyright 2004 John C. Smith, retrieved from http://www.hiddenloft.com/notes/SubExposures.pdf.

[69] Fenn, A. J., "Near-Field Testing of Adaptive Radar Systems," The Lincoln Laboratory Journal, Vol. 3, No. 1, pp. 23-40, 1990.

[70] Mainzer, Amanda K., et al. "Preliminary design of the wide-field infrared survey explorer (WISE)." Optics & Photonics 2005. International Society for Optics and Photonics, 2005.

[71] III. WISE Flight System and Operations (WISE All-Sky Release Explanatory Supplement: Flight System and Operations) http://wise2.ipac.caltech.edu/docs/release/allsky/expsup/sec3_2.html

[72] Wright, Edward L., et al. "The Wide-field Infrared Survey Explorer (WISE): mission description and initial on-orbit performance." *The Astronomical Journal* 140.6 (2010): 1868.

[73] Dotto, Elisabetta. "Observations of asteroids in the thermal infrared." REGOLITH ON SOLAR SYSTEM BODIES. INAF - Observatory of Rome (Italy). Observatoire de Paris CIAS 1 -3 Dec. 2010

[74] Lazzaro, Daniela, and Julio Angel Fernndez. *Asteroids, Comets, and Meteors (IAU S229).* No. 229. Cambridge University Press, 2006.

[75] Lim, Lucy F., et al. "Thermal infrared (813 m) spectra of 29 asteroids: the Cornell mid-infrared asteroid spectroscopy (MIDAS) survey." Icarus 173.2 (2005): 385-408.

[76] Maturilli, A., et al. "A Spectral Library of Emissivity Measurements for Asteroid Analogs." *Lunar and Planetary Science Conference.* Vol. 45. 2014.

[77] Zimmerman, B. and Wie, B., "GPU-Accelerated Computational Tool Development for Studying the Effectiveness of Nuclear Subsurface Explosions, IAA-PDC-15-03-15

[78] Strickland, B. R., and Lianos, D. P., "A Midcourse Multiple Kill Vehicle Defense against Submunitions." AIAA Defense and Space Programs Conference and Exhibit, Huntsville, AL, September 23-25, 1997. Vol. 9714, 1997.

[79] Payton, G., "Advanced Concepts in Missile Defense." *The George C. Marshall Institute* (2005): 14-20.

[80] Williams, D. S., Pflibsen, K., and Crawford, T., "Multiple Kill Vehicle (MKV) Interceptor and Method for Intercepting Exo and Endo-Atmospheric Targets," U.S. Patent No. 7,494,089. 24 Feb. 2009.

[81] Leal, M., Baker,T., and Pflibsen, K., "Multiple Kill Vehicle (MKV) Interceptor with Autonomous Kill Vehicles," U.S. Patent No. 7,494,090. 24 Feb. 2009.

[82] Zimmerman, B. and Wie, B., "A GPU-Accelerated Computational Tool for Asteroid Disruption Modeling and Simulation," *Acta Astronautica*, Vol. 127, 2016, pp. 644-654.

[83] Box, G. E. P., and Mervin, M. E.. "A Note on the Generation of Random Normal Deviates," *The Annals of Mathematical Statistics 29*, No. 2 1958, pp. 610-611.

[84] Lyzhoft, J., Basart J., and Wie B.. "A New Terminal Guidance Sensor System for Asteroid Intercept or Rendezvous Missions," *Acta Astronautica* 119, 2016, pp. 147-159.

[85] Otsu, N., "A Threshold Selection Method from Gray-Level Histograms," *Automatica*, 11(285-296), 1975, pp.23-27.

[86] Huang, D-Y, Lin, T-W, and Hu, W-C, "Automatic Multilevel Thresholding Based on Two-Stage Otsu's Method with Cluster Determination by Valley Estimation."

ICIC International Journal of Innovative Computing, Information and Control 7 (2011): 5631-5644.

[87] Kegelmeyer, L. M. et al., "Local Area Signal-to-Noise Ratio (LASNR) Algorithm for Image Segmentation," *Optical Engineering+ Applications*, International Society for Optics and Photonics, 2007.

[88] Bourdoux, Arnaud, and Dario Izzo. "Characterization and hazard mitigation of resonant returning Near Earth Objects." Final Stage Report, ACT internal report: ACT-RPT-4100-AB-CHMRRNEO05.

[89] Gronchi, Giovanni F., Giacomo Tommei, and Andrea Milani. "Mutual geometry of confocal Keplerian orbits: uncertainty of the MOID and search for virtual PHAs." *Proceedings of the International Astronomical Union* 236 (2006): 3.

[90] Bonanno, C. "An analytical approximation for the MOID and its consequences." *Astronomy and Astrophysics 360* (2000): 411-416.

[91] Chesley, Steven R., and Paul W. Chodas. "Asteroid close approaches: analysis and potential impact detection." *Asteroids III* (2002): 55.

[92] Gronchi, Giovanni F., "RESEARCH ACTIVITY." ATTIVIT Di RICERCA. http://adams.dm.unipi.it/~gronchi/HOMEPAGE/research.html N.p., n.d. Web. 23 Mar. 2016.

[93] Lee T, Leok M, McClamroch NH. Lie group variational integrators for the full body problem. *Computer Methods in Applied Mechanics and Engineering*. 2007 May 15;196(29):2907-24.

[94] Lee T, Leok M, McClamroch NH. Lie group variational integrators for the full body problem in orbital mechanics. *Celestial Mechanics and Dynamical Astronomy*. 2007 Jun 1;98(2):121-44.

[95] Maciejewski AJ. Reduction, relative equilibria and potential in the two rigid bodies problem. *Celestial Mechanics and Dynamical Astronomy*. 1995 Mar 1;63(1):1-28.

[96] Fahnestock EG, Scheeres DJ. Simulation and analysis of the dynamics of binary near-Earth Asteroid (66391) 1999 KW4. Icarus. 2008 Apr 30;194(2):410-35.

[97] Fahnestock EG, Lee T, Leok M, McClamroch NH, Scheeres DJ. Polyhedral potential and variational integrator computation of the full two body problem. InProc. AIAA/AAS Astrodynamics Specialist Conf., AIAA-2006-6289 2006 Aug 28.

[98] Galvez, A., Carnelli, I., Khan, M., Martens, W., Michel, P., Ulamec, S. and Hriscu, A., 2014. Asteroid investigation mission: the european contribution to the aida eu-us cooperation. *In Proceedings of the 24th International Symposium on Space Flight Dynamics*, Laurel, MD, USA.

[99] Margot, J.L., Nolan, M.C., Benner, L.A.M., Ostro, S.J., Jurgens, R.F., Giorgini, J.D., Slade, M.A. and Campbell, D.B., 2002. Binary asteroids in the near-Earth object population. *Science*, 296(5572), pp.1445-1448.

[100] Werner, R.A. and Scheeres, D.J., 2005. Mutual potential of homogeneous polyhedra. *Celestial Mechanics and Dynamical Astronomy*, 91(3-4), pp.337-349.

[101] Efthimiou, C. and Frye, C., 2014. Spherical harmonics in p dimensions. *World Scientific*.

[102] McMahon, J.W., 2011. *An analytical theory for the perturbative effect of solar radiation pressure on natural and artificial satellites* (Doctoral dissertation, University of Colorado).

[103] Kenneally, P., "High Geometric Fidelity Solar Radiation Pressure Modeling via Graphics Processing Unit," Master's Thesis, Aerospace Engineering Sciences Department, University of Colorado, Boulder, May 2016.

[104] Ruevekamp, S., 2009. *Orbital stability assessments of satellites orbiting Small Solar System Bodies* (Doctoral dissertation, TU Delft, Delft University of Technology).

[105] Bass, M., Van Stryland, E.W., Williams, D.R. and Wolfe, W.L. eds., 2001. *Handbook of optics* (Vol. 2). New York: McGraw-Hill.

[106] Wie, Bong. *Space vehicle dynamics and control, Second Edition*. Reston, VA: American Institute of Aeronautics and Astronautics, 2008. Print.

[107] McDonald, R., 2005. Tidal Forces and their Effects in the Solar System.

[108] Colagrossi, A., Ferrari, F. and Lavagna, M., 2015. Asteroids coupled dynamics analysis by means of accurate mass distribution and perturbations modelling. In *PDC Conference*.

[109] Lee, T., Leok, M. and McClamroch, N.H., 2007. Lie group variational integrators for the full body problem in orbital mechanics. *Celestial Mechanics and Dynamical Astronomy*, 98(2), pp.121-144.

[110] Lee, T., 2008. *Computational geometric mechanics and control of rigid bodies*. ProQuest.

[111] Cardoso, J.R. and Leite, F.S., 2003. The MoserVeselov equation. *Linear algebra and its applications*, 360, pp.237-248.

[112] Eberly, D., 2002. Polyhedral mass properties (revisited). *Geometric Tools*, LLC, Tech. Rep.

[113] Mirtich, B., 1996. Fast and accurate computation of polyhedral mass properties. *journal of graphics tools*, 1(2), pp.31-50.

[114] Dobrovolskis, A.R., 1996. Inertia of any polyhedron. *Icarus*, 124(2), pp.698-704.

[115] Press, W., Teukolsky, S., Vetterling, W. and Flannery, B., 1992. Numerical Recipes in Fortran 77: The Art of Scientific Computing, 933 pp.